



U.S. Department  
of Transportation

**National Highway  
Traffic Safety  
Administration**



---

DOT HS 812 404

April 2017

# High-Performance Computing Studies

## DISCLAIMER

This publication is distributed by the U.S. Department of Transportation, National Highway Traffic Safety Administration, in the interest of information exchange. The opinions, findings, and conclusions expressed in this publication are those of the authors and not necessarily those of the Department of Transportation or the National Highway Traffic Safety Administration. The United States Government assumes no liability for its contents or use thereof. If trade or manufacturers' names or products are mentioned, it is because they are considered essential to the object of the publication and should not be construed as an endorsement. The United States Government does not endorse products or manufacturers.

Neither NCMS, members of NCMS, nor any person acting on behalf of them:

- makes any warranty or representation, express or implied, with respect to the accuracy, completeness or usefulness of the information contained in this report, or that the use of any information, apparatus, method, or process disclosed in this report may not infringe privately owned rights, or
- assumes any liability with respect to the use of, or from damages resulting from the use of, any information, apparatus, method, or process disclosed in this report.

The views and conclusions contained herein are those of the authors and should not be interpreted as necessarily representing the official policies or endorsements, either expressed or implied, of the U. S. Government.

Suggested APA Format Citation:

National Center for Manufacturing Sciences. (2017, April). *High-performance computing studies* (Report No. DOT HS 812 404). Washington, DC: National Highway Traffic Safety Administration.

### Technical Report Documentation Page

1. Report No. DOT HS 812 404		2. Government Accession No.		3. Recipient's Catalog No.	
4. Title and Subtitle High-Performance Computing Studies			5. Report Date April 2017		
			6. Performing Organization Code		
7. Authors			8. Performing Organization Report No.		
9. Performing Organization Name and Address National Center for Manufacturing Sciences 3025 Boardwalk Drive, Ann Arbor MI 48108			10. Work Unit No. (TRAIS)		
			11. Contract or Grant No. DTNH22-14-D-00321		
12. Sponsoring Agency Name and Address National Highway Traffic Safety Administration			13. Type of Report and Period Covered DRAFT Final, June 2014-June 2016		
			14. Sponsoring Agency Code		
15. Supplementary Notes					
16. Abstract <p>Carbon Fiber reinforced plastic (CFRP) material is becoming one of the preferred solutions for vehicles to achieve overall weight reduction in order to meet fuel economy and emission standards while maintaining safety requirements. Carbon fiber thermoplastic composites offer several advantages compared to metallic alternatives, including higher levels of ductility and specific energy absorption, rapid processing, and recyclability and reuse. The objective of this study was to investigate the computational tools for the design, optimization and manufacture of carbon fiber thermoplastic materials for vehicle sideframe structures (e.g., B-pillar) subjected to high-velocity side-impact crash loading, and to investigate and demonstrate the appropriateness of simulative methods and tools to adequately predict behavior relevant for the assessment of vehicle safety.</p> <p>In this study, CFRP intensive vehicle components were designed, manufactured, and tested. The project team investigated thermoplastic carbon fiber reinforced materials for vehicle sideframe structures, created requirements, and defined assessment strategies. The design of the B-pillar was followed by the manufacturing and testing of a prototype and validation of the predictive engineering tools.</p> <p>The study limitations included constitutive models and modeling approaches.</p> <p>This study demonstrated that the carbon fiber thermoplastic B-pillar offered 60 percent weight savings over the metallic baseline and satisfied the side-impact crash requirements. Also, the dynamic impact and crush response of the B-pillar was adequately modeled using computational tools.</p>					
17. Key Word Crash Simulations, Restraint System Optimization, Field Data Analysis, Field Performance Evaluation, Seatbelt Interlock, Unbelted Requirements				18. Distribution Statement	
19. Security Classif. (of this report)		20. Security Classif. (of this page)		21. No. of Pages 133	22. Price

Form DOT F 1700.7 (8-72)

Reproduction of completed page authorized

# Table of Contents

---

List of Figures.....	v
List of Tables.....	x
Acronyms and Abbreviations.....	xi
1. Executive Summary.....	1
2. Introduction.....	2
3. B-Pillar Performance Requirements.....	7
3.1 FMVSS No. 214.....	7
3.1.1 Test Description.....	7
3.2 Structural Requirements for FMVSS No. 214 Barrier Side-Impact.....	7
3.2.1 Link Between Structural Design and Occupant Safety .....	8
3.2.2 Functional Design Requirements.....	8
3.2.3 Geometrical Design Requirements.....	9
3.3 Structural Requirements for CFRP Components in a Crash Load Path.....	10
3.3.1 Structures in Crash Management Systems .....	10
3.3.2 Energy Dissipation Zones.....	11
3.3.3 Materials .....	13
3.3.4 Test Results: Second Impact on Damaged CFRP Components .....	15
3.3.5 Summary .....	19
4. B-Pillar Assessment Strategy and Models.....	20
4.1 Derivation of Component Model.....	20
4.2 Analytical Calculation of Deformation Energy .....	21
4.3 Definition of Loading and Boundary Conditions for the Component Model Using FEA .....	22
5. Material Selection and Test Data for Design.....	26
5.1 Carbon Fiber Thermoplastic Material Requirements.....	27
5.2 Material Selection Approach .....	28
5.3 Material Sourcing and Acquisition .....	28
5.4 Processing, Microstructure and Quality Assessment .....	28
5.5 Mechanical Property Characterization for Screening .....	29
5.6 Material Selection for B-Pillar .....	32
5.7 Material Card Generation for Simulations .....	35



5.8	Adhesive Bonding for Hat/Spine/Rail Joints .....	36
5.9	Adhesive Selection.....	36
5.10	Adhesive Bond Strength Assessment .....	37
5.11	Plexus MA530 Cure Cycle Development .....	37
5.12	Summary.....	38
6.	Design and Analysis .....	39
6.1	Introduction/Background .....	39
6.1.1	Objectives and Approach.....	39
6.1.2	BMW Metal Baseline Reduced B-Pillar Impact Model .....	39
6.1.3	Design Requirements for Composite B-Pillar .....	41
6.2	Design and Production Methodology for Composite B-Pillar.....	41
6.2.1	Development of Design Methodology .....	41
6.2.2	CATIA Composite Model Definition .....	43
6.2.3	CATIA to LS-DYNA Using Altair HyperMesh .....	47
6.2.4	NASTRAN BDF to DYNA Keyfile Translator.....	48
6.2.5	Baseline Composite Model in CATIA.....	49
6.2.6	Composite B-Pillar Design Studies.....	50
6.2.7	Analysis of Composite B-Pillar Design G50 and G51 .....	54
6.2.8	Finalized “TAB” Design of G81 TAB Composite B-Pillar .....	56
6.3	Analysis Methodology for Composite B-Pillar .....	61
6.3.1	BMW Metal Baseline Reduced B-Pillar Impact Model .....	61
6.3.2	Separation of Metal B-Pillar From BMW Baseline Metal Model and Development of Modular LS-DYNA Input Deck System for Composite B-Pillar.....	61
6.3.3	Contacts Between Metal and Composite Parts .....	61
6.3.4	Adhesive Joints .....	62
6.3.5	Selection of Composite Material Model for B-Pillar Applications .....	62
6.3.6	Material Model and Parameters.....	63
6.3.7	Adhesive Properties and Determination of Traction Law Parameters .....	66
6.3.8	Model Validating Sub-Component Tests .....	69
6.4	G81 TAB Composite B-Pillar Model Validation with New MAT54 Model Parameters ..	73
6.5	Summary and Conclusions .....	75
7.	Processing and Part Fabrication.....	77
7.1	Introduction .....	77
7.2	Liquid Molding Processing of Spine .....	78

7.3	Hat Section Manufacturing.....	82
7.3.1	Incoming Prepreg Quality .....	83
7.3.2	Blank Evaluations .....	83
7.3.3	IR Heating and Forming Process.....	85
7.3.4	Sub-Element Hat Section Production .....	86
7.3.5	Hat Production.....	89
7.4	B-Pillar Assembly .....	90
7.4.1	Adhesive Bonding Procedure .....	90
7.4.2	Hat to Spine Assembly and Bonding .....	91
7.4.3	B-Pillar to Rocker Assembly and Bonding .....	93
8.	Full-Scale Testing and Simulations.....	96
8.1	UD-CCM Tower of Power Low-Velocity Impact Testing Facility.....	96
8.2	Experimental Setup for Impact Testing of Composite B-Pillars .....	100
8.3	TOP-LVI Experimental Results .....	101
8.3.1	TOP-LVI Experimental Results of Composite B-Pillar B3.....	103
8.3.2	Post-Impact Damage Analysis of Composite B-Pillar B3.....	103
8.4	Simulation of Full-Scale Full Energy Impact Experiments on Composite B-Pillars...	105
8.4.1	FE Model of TOP-LVI Experiment .....	105
8.4.2	Results and Discussion on TOP-LVI Simulations .....	108
9.	Feedback from Vehicle Simulation.....	114
9.1	Geometrical Vehicle Integration .....	114
9.1.1	LS-DYNA to ABAQUS Translation .....	114
10.	Conclusions .....	118

# List of Figures

---

Figure 2-1. Computational Design Framework.....	4
Figure 2-2. Adhesively Bonded Assembly of B-Pillar .....	5
Figure 2-3. Comparison of Experimental and Predicted B-Pillar Deformation Shows Good Correlation.....	6
Figure 2-4. Design Loop Considers Full Vehicle Simulation.....	6
Figure 3-1. Test Configuration FMVSS NO. 214 Side-Impact, all dimensions in mm, velocity in km/h .....	7
Figure 3-2. Intrusion Requirements at Certain Crucial Points in Time.....	9
Figure 3-3. Locations of Considered Intrusion Measurements on B-Pillar.....	9
Figure 3-4. Crash Zone 1 .....	12
Figure 3-5. Crash Zone 2 .....	12
Figure 3-6. Crash Zone 3 .....	12
Figure 3-7. Crash Zone 4 .....	13
Figure 3-8. Footwell After Frontal Impact, Steel (left) Versus CFRP (right).....	14
Figure 3-9. Occupant Compartment After Side-Impact,Steel (top) Versus CFRP (bottom).....	15
Figure 3-10. CT-Scan of Splintering in Bulkhead After Frontal Impact.....	15
Figure 3-11. Footwell After Frontal Impact in CFRP Life-Cell With Lower (top) Versus Higher (bottom) Load Impact Energy.....	17
Figure 3-12. Component Test Setup Roof Rail .....	18
Figure 3-14. Load and Absorbed Energy Over Time of First and Second Impact Test .....	18
Figure 4-1. Derivation of Component Model.....	21
Figure 4-2. Comparison of Deformation Pattern Between Stage 2 and Stage 3 Model .....	21
Figure 4-3. Velocity Versus Time of Vehicle and Barrier .....	22
Figure 4-4. Evaluated Impactor Variants.....	24
Figure 4-5. Cross-Section Showing Barrier – B-Pillar Interaction.....	24
Figure 4-6. Comparison of Shape During Impact Between Impactor Variant 3 and MDB .....	25
Figure 5-1. Temperature Capability of Various Thermoplastic Polymers .....	26
Figure 5-2. Pillar Design Zones and Typical Cross Sections.....	32
Figure 5-3. Pillar Section View .....	33
Figure 5-4. Key Properties of Material Systems .....	34
Figure 5-5. Key Properties of PEI, Nylon, and ELIUM, Normalized to Nylon Properties .....	35
Figure 5-6. Ply Orientation and Energy Absorption .....	35
Figure 5-7. B-Pillar Design .....	36

Figure 6-1. Different Views of Metal Baseline Reduced B-Pillar Impact Model Impact Mass, $M = 375.31 \text{ kg}$ . Impact Velocity, $V = 9.00 \text{ m/s}$ .....	39
Figure 6-2. Different Views of Deformed Metal Baseline Reduced B-Pillar Impact Model Time, $t = 34 \text{ ms}$ .....	39
Figure 6-3. Quantitative Design Requirements for the Metal Baseline Reduced B-Pillar Impact Model .....	40
Figure 6-4. Design Framework and Workflow .....	42
Figure 6-5. SMARTree Client Used to Capture, Store and Share Material Property Data .....	42
Figure 6-6. Thermoplastic Material Database Workflow Within SMARTree Client .....	44
Figure 6-7. Creation of Grid and Laminate Cells .....	45
Figure 6-8. Virtual Stacking Management .....	46
Figure 6-9. Creation of Plies Based on Grid Definition With Option to Manually Adjust Transition Regions.....	46
Figure 6-10. Composite Definition Exportable to Commercial Solvers .....	47
Figure 6-11. CAD to DYNA Workflow through Altair HyperMesh .....	48
Figure 6-12. LS-DYNA Keyfile Generator.....	49
Figure 6-13. Initial Parametric CAD Surface Model.....	50
Figure 6-14. Design Iterations for Composite B-Pillar .....	51
Figure 6-15. Spine-Hat Composite B-Pillar Adhesively Bonded Over Entire Boundary .....	51
Figure 6-16. Hat Composite Designed With Discrete Functionality .....	52
Figure 6-17. Two-Part Spine-Hat Bonded B-Pillar Design.....	52
Figure 6-18. AS4/Nylon Hat Composite Design and Stacking Configuration .....	53
Figure 6-19. AS4/Nylon Spine Composite Design and Stacking Configuration.....	53
Figure 6-20. Thickness Maps of (a) B-Pillar and (b) Associated Ply Layup.....	54
Figure 6-21. LS-DYNA Crash Simulation Result at Various Times Composite B-pillar design G50 computational run #90 designated by "091-G50. Material AS4/Nylon, Total Weight 7.26 kg as compared to Metal Baseline weight of 9 kg.....	55
Figure 6-22. Dynamic Deformation or Intrusion at Different Times G50-Composite B-Pillar, Material AS4/Nylon .....	55
Figure 6-23. Time History of Impactor Ridge Body Velocity (RBV) and Impact-Contact Force G50-Composite B-Pillar, Material ZS4/Nylon; G51-Composite B-Pillar, Material AS4/Nylon Hat & AS4/PEI Spine.....	56
Figure 6-24. Impactor Rigid Body Velocity (RBV) and Impact-Contact Force Versus Impactor Rigid Body Displacement (RBD)G50-Composite B-Pillar, Material AS4/Nylon; G51- Composite B-Pillar, Material AS4/Nylon Hat & AS4/PEI Spine.....	56
Figure 6-25. Axial Strain Distribution on G50 Hat and Spine G51-Composite B-Pillar, Material AS4/Nylon Hat & AS4/PEI Spine .....	57

Figure 6-26. Finalized G81 TAB Composite B-Pillar Design to Reduce Strain Concentrations, to Reduce Weight, and to Increase Producibility .....	58
Figure 6-27. Dynamic Deformation at the Root of Finalized G81 TAB Composite B-Pillar Design Material AS4/Nylon Hat and AS4/PEI Spine. Total Weight 3.86 kg (57% weight reduction as compared to Metal Baseline).....	58
Figure 6-28. Strain Concentration of Finalized G81 TAB Composite B-Pillar Design.....	59
Figure 6-29. Crash Performance of Finalized G81 TAB Composite B-Pillar Design .....	59
Figure 6-30. Brief Overview of Composite B-Pillar Design Process .....	60
Figure 6-31. Weight and Cost of Different Composite B-Pillar Designs .....	60
Figure 6-32. Different Views of Metal Baseline Reduced B-Pillar Impact Model Impact Mass, $M = 375.31 \text{ kg}$ . Impact Velocity, $V = 9.00 \text{ m/s}$ .....	61
Figure 6-33. Different Views of Metal Baseline Reduced B-Pillar Impact Model With Metal B-Pillar Removed .....	62
Figure 6-34. Adhesive Bond Between Roof and Composite B-Pillar and Between Rocker and Composite B-Pillar .....	62
Figure 6-35. Stress-Strain Behavior Modeled in MAT54 .....	63
Figure 6-36. TT-Tension Tests and Estimation of Mode I Cohesive Parameters .....	67
Figure 6-37. Lap-Shear Tests and Estimation of Mode II Cohesive Parameters.....	68
Figure 6-38. Parametric Determination of Cohesive Parameters for Plexus 50°C Adhesive.....	69
Figure 6-39. Summary of Cohesive Parameters for Adhesives Evaluated.....	69
Figure 6-40. Hat-Beam Crush Test Setup .....	70
Figure 6-41. Load-Displacement of Hat-Beam Crush Tests Loading Rate = 0.010 m/s.....	70
Figure 6-42. FE Model of Hat-Beam Crush Test and Simulation with Baseline Parameters ....	71
Figure 6-43. Baseline and Optimized MAT54 Simulation Parameters .....	72
Figure 6-44. Parametric Optimization of MAT54 Model Parameters for Maximizing Crush Force and Crush Work Done .....	74
Figure 6-45. Model Validation of Composite B-Pillar Design 110C-G81-NPP-THK-RUN-4 with Experimentally Validated MAT54 Material Parameters .....	75
Figure 7-1. Several New Programs Considering Composites at Much Higher Volumes .....	77
Figure 7-2. Schematic of VARM Process [ <a href="http://www.tpicomposites.com/?id=9">http://www.tpicomposites.com/?id=9</a> ] .....	78
Figure 7-3. Preform Kitting and Assembly on Tool.....	80
Figure 7-4. Final Infusion Setup of Spine .....	81
Figure 7-5. Viscosity Behavior of Elium Resin Systems .....	81
Figure 7-6. Dry-Spots After Infusion and Evaporation Behavior of Elium Resin.....	82
Figure 7-7. Initial Production of 8 Spines.....	82

Figure 7-8. Schematic of Forming Station .....	83
Figure 7-9. Microstructure of Incoming Tencate Tape Material .....	84
Figure 7-10. Thickness Information of Prepreg and Processed Material.....	84
Figure 7-12. Ultrasonic C-Scan Indicate Part Variation for Different Process Conditions .....	85
Figure 7-13. Temperature History During Heating and Forming of Blanks.....	86
Figure 7-14. Optimized Forming Process Leads to Desired Microstructure and Quality .....	86
Figure 7-15. Sub-Element Hat Tooling .....	87
Figure 7-16. Photo of Sub-Element Specimen and Assembled Microscopic Image.....	88
Figure 7-17. Microscopic Photos Taken from Sub-Element Hat.....	88
Figure 7-18. Assembly of Prepreg Pieces to Form Hat Blank .....	89
Figure 7-19. Forming Cell for Full-Scale Hats .....	89
Figure 7-20. Photo of First Three Hats Produced.....	90
Figure 7-21. Surface Treated (grit-blast) Spine Section Ready for Assembly .....	91
Figure 7-22. Adhesive Dispensing with Robot Head on Hat Prior to Assembly.....	92
Figure 7-23. Adhesively Bonded Hat and Spine Assembly .....	93
Figure 7-24. Assembled B-Pillar in Rocker Assembly and Impact Fixtures in Drop Tower .....	94
Figure 7-25. Surface Preparation of Steel Rocker.....	94
Figure 7-26. Adhesively Bonded Assembly of B-Pillar and Rocker .....	95
Figure 8-1. Different Views of As-Manufactured Composite B-Pillars .....	96
Figure 8-2. (a) High-Energy Drop Tower (TOP2000) and (b) Cross-Beam Showing B-Pillar Fixture Hardware Mounted in Place and Ready for Testing.....	97
Figure 8-3. (a) Ratchet Catch Mechanism and (b) Vertical Ratchet Rails Mounted on Guide Beams.....	98
Figure 8-4. FOV Modeling in CATIA for B-Pillar Impact Test to Confirm View Area.....	99
Figure 8-5. (a) Floating Beam With Camera Mounting, (b) FOV for DIC System, (c) Opening for Camera, and (d) Floating Platform Within Floor of TOP2000 .....	99
Figure 8-6. TOP Impact Test Fixture for Testing Composite B-Pillar TOP Drop Height $hI = 26924 - mm = 106 - inches$ , TOP Drop Mass $mP = 1265 - lbs = 568.80 - kg$ , TOP Impact Velocity $VI = 23.82 - ftsec = 7.26 - ms$ , TOP Impact Energy $EI = 15.02 - kJ$ .....	100
Figure 8-7. Time History of Impact-Contact Force .....	102
Figure 8-8. Snapshots of Deformation of Composite B-Pillar Under TOP-LVI Loading.....	102
Figure 8-9. TOP-LVI Experimental Results of Composite B-Pillar B3 .....	104
Figure 8-10. Plastic Deformation of Rocker Box Assembly of Composite B-Pillar B3 .....	104
Figure 8-11. Different Damage Mechanisms of Composite B-Pillar B3.....	105

Figure 8-12. FE Model of the TOP-LVI Experiment.....	107
Figure 8-13. Four-Point Bend Test Results of As-Received AISI 1050 Steel .....	107
Figure 8-14. Snapshots of Composite B-Pillar Deformation at Different Times.....	109
Figure 8-15. Time History of Impact-Contact Force and RBD of Impactor Pin Comparison between the simulation and experiments .....	110
Figure 8-16. Impact-Contact Force versus RBD Simulation and Experiment B3 .....	110
Figure 8-17. Dynamic Deformation and Displacement of Spine Centerline Simulation and Experiment B3.....	110
Figure 8-18. Various Stages of Vehicle Models Used to Predict Occupant Intrusion.....	111
Figure 8-19. Time History of Dynamic Displacement on Centerline of B-Pillar at a Point Location of Maximum Dynamic Displacement of Individual Components.....	113
Figure 8-20. Spine Deflection at Key Times With Peak Deflection for Metal Baseline, CFRP Model and Experiment.....	113
Figure 9-1. BIW Model With Cut Outs and Adjustments for Composite B-Pillar Integration...	115
Figure 9-2. Stress-Strain Comparison Between LS-DYNA MAT54 and Initial ABAQUS Material Model .....	115
Figure 9-3. Stress-Strain Enhanced ABAQUS Material Model.....	116
Figure 9-4. Comparison of Metal Baseline and Composite B-Pillar at Stage 2 Vehicle Model, Door Hinge Causing Local Collapse of Hat Section.....	117
Figure 9-5. Comparison of Metal Baseline and Composite B-Pillar Intrusion Over Time .....	117

# List of Tables

---

Table 2-1. Commercial Thermoplastic Materials and Suppliers for Automotive Market .....	3
Table 5-1. Material Suppliers, Forms, and Processing Conditions.....	28
Table 5-2. Microscopic View of Material Systems Structure.....	30
Table 5-3. Mechanical Testing Results .....	31
Table 5-4. Material Characterization .....	34
Table 5-5. Lap-Shear Strength Results of Adhesive and Surface Treatment Combinations ....	37
Table 5-6. Lap-Shear Strength Results of Substrates with Plexus MA530.....	37
Table 5-7. Substrate Adhesion Test Results .....	38
Table 5-8. Lap-Shear Test Results .....	38
Table 6-1. MAT54 Card Parameters .....	64
Table 8-1. Mass Properties of B-Pillar.....	96



# Acronyms and Abbreviations

---

3D	three-dimensional
ABB	automated adhesive bonding
ASTM	American Section of the International Association for Testing Materials
BIW	body-in-white
BMW	Bayerische Motoren Werke
CAD	computer-aided design
CAE	computer-aided engineering
CATIA	computer-aided three-dimensional interactive application
CF	carbon fiber
CFC	chlorofluorocarbon
CFRP	carbon fiber reinforced plastic
CPM	composite design for manufacturing
CT	computerized tomography
DAQ	data acquisition
DIC	differential interference contrast
DoT	Department of Transportation
DSC	differential scanning calorimetry
FE	finite element
FEA	finite element analysis
FMVSS	Federal Motor Vehicle Safety Standard
FOV	field of view
GIC	critical strain energy release rate
GM	General Motors
GUI	graphical user interface
HPRTM	high-pressure resin transfer molding
IR	infrared
Kg	kilogram
kJ	kilojoules
lb.	pound
LCM	liquid composite molding
m	meter
MAP 21	Moving Ahead for Progress in the 21 <sup>st</sup> Century Act
MDB	movable deformable barrier
mm	millimeter
ms	millisecond
m/s	meters per second
NCMS	National Center for Manufacturing Sciences
OEM	original equipment manufacturer
PAN	polyacrylonitrile
PCIV	plastics and composites intensive vehicle
RBD	rigid body displacement
RBV	rigid body velocity
RFI	resin film infusion
RTM	resin transfer molding
T <sub>g</sub>	glass transition
T <sub>m</sub>	melt temperature
T <sub>s</sub>	service temperature
TT	through-thickness
UD-CCM	University of Delaware Center for Composite Materials
VARTM	vacuum-assisted resin transfer molding

# 1. Executive Summary

---

Carbon fiber reinforced plastic (CFRP) material is becoming one of the preferred solutions for vehicles to achieve overall weight reduction in order to meet fuel economy and emission standards while maintaining safety requirements. Current CFRP vehicle structures are fabricated by injecting and curing thermosetting polymers into carbon fiber preforms. Carbon fiber thermoplastic composites offer several additional advantages: higher levels of ductility and specific energy absorption; rapid processing; and recyclability and reuse. The purpose of this project was to investigate the computational tools for the design, optimization and manufacture of carbon fiber thermoplastic materials for vehicle side frame structures (e.g., B-pillar) subjected to high-velocity side-impact crash loading, and to investigate and demonstrate the appropriateness of simulative methods and tools to adequately predict behavior relevant for the assessment of vehicle safety. The B-pillar is the support post that connects a vehicle's roof to its body at the rear of the front occupant door that provides the major source of resistance to occupancy compartment intrusion during a side-impact collision. The B-pillar was developed using computer-aided design (CAD) and computer-aided engineering (CAE) and evaluated using both simulation and hardware for legal safety requirements.

To address this issue, the Department of Transportation's National Highway Traffic Safety Administration (DOT/NHTSA) awarded the National Center for Manufacturing Sciences (NCMS) a contract to research this material and to evaluate its impact on vehicle crash safety and weight savings.

A project team, led by NCMS, was formed consisting of two technology providers, Bayerische Motoren Werke (BMW) and the University of Delaware Center for Composite Materials (UD-CCM). NCMS, a not-for-profit collaborative research consortium of 83 cross-industry members based in Ann Arbor, Michigan, played a traditional program management role. BMW, a manufacturer of automobiles, was the first original equipment manufacturer (OEM) in the automobile industry to offer high-volume production vehicles with a significant amount of composite materials used in structural applications. Within the scope of this project, BMW assisted UD-CCM by supplying vehicle design and safety requirements derived from full vehicle crash simulations as well as feedback and guidance on all project tasks. UD-CCM, an internationally recognized interdisciplinary Center of Excellence for Composites conducted the composite design, analysis and optimization computational tasks, developed tooling and novel processing methods for forming and multi-material joining, and manufactured full-size carbon fiber thermoplastic B-pillar assemblies that were tested under full-energy, high-velocity side-impact crash conditions.

The overall goals of this project were met by the design, manufacture and testing of carbon fiber thermoplastic B-pillar that offered 60 percent weight savings over the steel baseline and satisfied the side-impact crash requirements specified in Section 3. The dynamic impact and crush response of the B-pillar was adequately modeled using computational tools. Opportunities for improvement in materials constitutive models and modeling approaches were identified based on detailed correlations with the sub-component and full-scale crash test results.

## 2. Introduction

---

As part of the Moving Ahead for Progress in the 21st Century Act (MAP-21), NHTSA was requested to research the inclusion of emerging lightweight plastic and composite technologies in motor vehicles to increase fuel efficiency, lower emissions, meet fuel economy standards, and enhance occupant motor vehicle safety through continued use of the NHTSA's *Plastic and Composite Intensive Vehicle Safety Roadmap* (Report No. DOT HS 810 863). This Safety Roadmap identified several key research efforts the agency could support to help encourage the wider commercial adoption of fuel efficient, safe vehicles using plastics and composites intensive vehicle (PCIV) structures. Many of these identified research efforts focused on the need to develop and demonstrate the utility of predictive engineering tools to evaluate and optimize the crash safety of load bearing PCIV components. NHTSA sought to identify and evaluate safety benefits of structural plastics and composites applications in future lighter, more fuel efficient and environmentally sustainable vehicles. The PCIVs safety research also supported national and global efforts to design and deploy vehicles with improved fuel efficiency and emissions, without compromising their crash safety.

Previous studies have shown that composite structures deform in a manner different than similar structural components made of conventional materials like steel and aluminum. The micro-mechanical failure modes, such as matrix cracking, de-lamination, and fiber breakage, constitute the main failure modes of composite structures. These complex fracture mechanisms make it difficult to analytically and numerically model the collapse behavior of fiber reinforced composite structures.

This project was an effort toward implementing these safety goals while reducing vehicle weight. A research approach was formulated to advance the simulation capabilities to effectively model and predict the behavior of composite structures in automotive applications.

UD-CCM and BMW led the technical development of this project to design, manufacture and test CFRP intensive vehicle components. The team investigated thermoplastic (TP) carbon fiber reinforced materials for vehicle side frame structures. B-pillar requirements have been defined (Section 3) and assessment strategies have been proposed (Section 4). The main structural design targets for side-impact were related to a required distance between a hard surface of the body-in-white (BIW) or interior components and the occupant/dummy at certain points in time. It was assumed that when these minimum distance measures were not exceeded, the system allowed enough space for the air bags to deploy and protect the occupant in an adequate manner.

Commercially available thermoplastic materials were characterized (Section 5) to define appropriate material models and to evaluate energy absorption mechanisms. A number of carbon fiber thermoplastic material choices are currently available in the marketplace with a variety of carbon fiber and thermoplastic resin choices and material forms. A preliminary materials screening strategy was adopted for all materials sourced in this effort, to down-select promising candidate systems for detailed assessment and material card development. In addition to mechanical material evaluation, ultrasonic scans for panel quality, fiber volume fraction and density measurements were performed for all material systems and assessed microstructural performance of these composites. In Table 2-1 the commercial thermoplastic materials are examined.

Predictive engineering at all levels, from coupon to sub-element to full-scale, guided the material down-selection. State-of-the-art CAE tools simulating full vehicle to component and test setup behavior were used to optimize manufacturability and structural/crash performance (Section 6). A preferred subsystem concept (e.g., rocker and roof frame) was developed to allow rapid computational iterations within the subsystem. A study of commercial tools for establishing this methodology was carried out with CATIA chosen as the CAD-CAE design tool; Altair’s HyperWorks as a finite element (FE) pre- post-processing tool and LSTC LS-DYNA as the crash analysis solver. CATIA was chosen as the CAD interface as this software has unique capabilities for virtual design and manufacturing of multi-layer composites with data export directly to thirdparty FE solvers. HyperMesh 13.0 was used as the FE preprocessor to use the powerful surface meshing capabilities and recently added drape functionality with ply and laminate realization. Various carbon fiber thermoplastic materials were evaluated (see Section 5) and material properties and parameters were determined in LS-DYNA for impact prediction. In Figure 2-1, these materials and the computational design framework are shown. A thermoplastic carbon composite B-pillar was designed using the predictive engineering environment and the safety performance for side crash was evaluated.

Table 2-1. Commercial Thermoplastic Materials and Suppliers for Automotive Market

Material Form	TP	Process	US Suppliers	European Suppliers
Fabric (2D/3D, NCF)	Elium TP	Infusion	Weavers	Weavers
Long Fiber Thermoplastic (LFT)	PA6, PA66, PPA	Forming	Celanese	Celanese
Co-mingled Fabric	PA6, PA66, PP	Forming	Concordia, FGI (glass/PP)	Comfil APS (Denmark)
UD Prepreg Tape	PA6, PA66, PPA, PET, PP	Forming	Tencate, Celanese, Vector, Sabic, ...	Tencate, Celanese, Vector, Sabic, Suprem
Semi-preg (fabric)	PP, PA66, PET	Forming	Vector	Tencate (Netherlands), Porcher (France)
Co-Woven Fabrics	PP, PA66, PET	Forming	Vector	Unknown
Coated Tow (can be woven, braided etc)	PP, PA6, PPA, PA66, PET	Forming	Fibrtec	Unknown
Stretch-Broken CF	Unknown	Forming	DuPont	Schappe Techniques (France)
Pre-consolidated Laminates	PP, PA6, PA66, TPU	Forming	Lingol, Tencate, Celanese	Bond (Germany), Tencate, Suprem

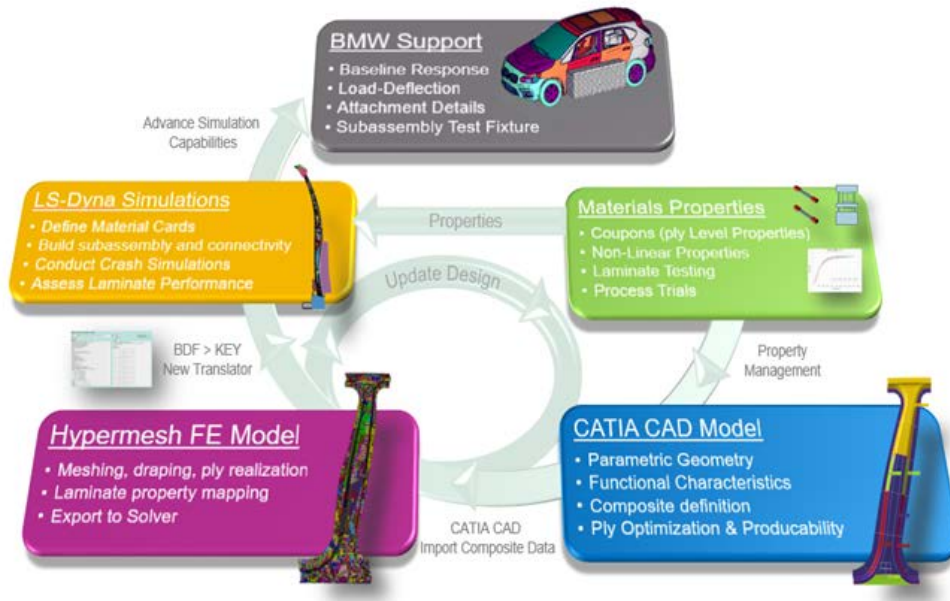


Figure 2-1. Computational Design Framework

The design of the B-pillar was followed by the manufacturing (Section 7) and testing of a prototype at UD-CCM and validation of the predictive engineering tools. Sub-components and B-pillars were fabricated at UD-CCM using the stamp forming and infusion processes allowing scalability with the potential to meet automotive production rates in the future. The processing approach affects local material properties, impacting performance. UD-CCM implemented a new forming cell to allow fabrication of engineered blanks and the forming of the blanks in a heated press system to produce the hat section. The process showed potential cycle times of around 2 minutes to form a complex geometry hat section.

Vacuum-assisted resin transfer molding (VARTM) including fabrication of the dry preform followed by infusion and cure allowed spine production meeting the high-fiber volume fraction requirements. Tooling for both processes were designed, fabricated and met tolerance requirements. The tools were used as a tooling jig for final assembly using an adhesive bonding approach of the spine to the hat section. Final weight of the assembled B-pillar was within 5 percent of the prediction with good translation of geometry and thickness requirements.

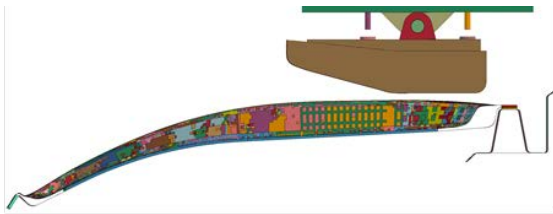
Finally, the UD-CCM large drop tower was used to validate the predictive engineering tools and crash performance of the proposed B-pillars under realistic side-impact crash conditions (Section 8). A high-energy, custom-designed drop tower was used to test the B-pillar sub-assembly. An impact test fixture was designed and built to test the composite B-pillar under high-speed crush test impact conditions similar to the subsystem impact simulations. The test fixture consisted of three components, i.e. (i) consumable steel rocker assembly and end clamps, (ii) clamps for the composite B-pillar at the roof, and (iii) the impactor assembly. The composite B-pillar was adhesively bonded to the steel rocker hat-section and cured prior to the rocker assembly (Figure 2-2). Various measurements were taken during testing including load, displacement and strain readings. Five composite B-pillars have been impact tested with similar impact conditions and results compared with a FE model of the conducted impact experiment developed from a CATIA solid model for LS-DYNA applications. Agreement of the loading and displacement measurements was established demonstrating the fidelity of the predictive tools. This comparison is shown in Figure 2-3.



*Figure 2-2. Adhesively Bonded Assembly of B-Pillar*

The final design was validated in the full vehicle simulation (Section 9). This allowed performance feedback for the composite B-pillar design on the full vehicle level. See Figure 2-4 for a visual representation of this process. Integration of the composite B-pillar into the vehicle simulation model required some modification of both the geometry of the BIW FE representation and the material models used for crash modeling of composites at BMW. Eventual design changes to the component can be considered and validated at the full vehicle level to improve ultimate performance. This report summarizes the results and provides recommendation for future work (Section 10).

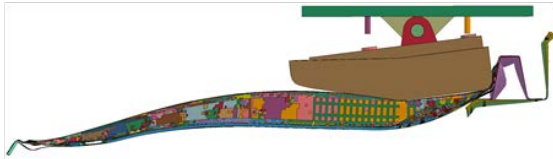
The project goal to advance the simulation capabilities to effectively model and predict the safety behavior of composite structures in automotive applications and to show the potential of thermoplastic carbon composites to attain equal or better occupant safety performance at 60 percent weight reduction as equivalent vehicle components in the market today has been demonstrated. The B-pillar design meets structural and crash safety requirements (e.g., FMVSS No. 214 barrier specified in Section 3) in the subsystem environment using thermoplastic composites that offers significant advantages (e.g., recycling, joining) compared to thermoset with the potential for improved crash performance. The holistic approach looked at new composite materials and processes for automotive applications with the ultimate goal to increase confidence in the predictive design tools available to the automotive community.



(i) Time  $t = 0$  ms



(a) Time  $t = 0$  ms



(ii) Time  $t = 30$  ms



(b) Time  $t = 30$  ms



(iii) Time  $t = 60$  ms



(c) Time  $t = 60$  ms

TOP-LVI Simulation RUN # 1

TOP-LVI Experiment # B3

Figure 2-3. Comparison of Experimental and Predicted B-Pillar Deformation Shows Good Correlation

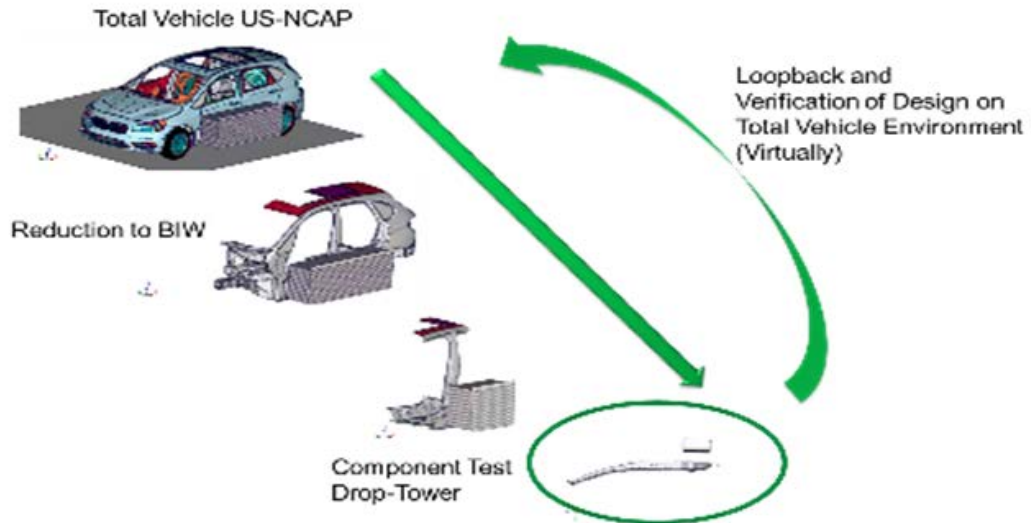


Figure 2-4. Design Loop Considers Full Vehicle Simulation



## 3. B-Pillar Performance Requirements

### 3.1 FMVSS No. 214

The side-impact is a primary challenge when considering occupant safety in vehicle development. In particular, it is the most relevant safety-based structural challenge for the development of a composite reinforced B-pillar. The Federal Motor Vehicle Safety Standard Part 571.214 (FMVSS No. 214), side-impact of a movable deformable barrier (MDB), was chosen as base requirement to fulfill in this project.

#### 3.1.1 Test Description

The full test description including the requirements to fulfill this test can be obtained from the U.S. Government Publishing Office, Electronic Code of Federal Regulations (<http://www.ecfr.gov/>).

A short overview of the FMVSS No. 214 load case can be given by describing the impact conditions based on Figure 3-1.

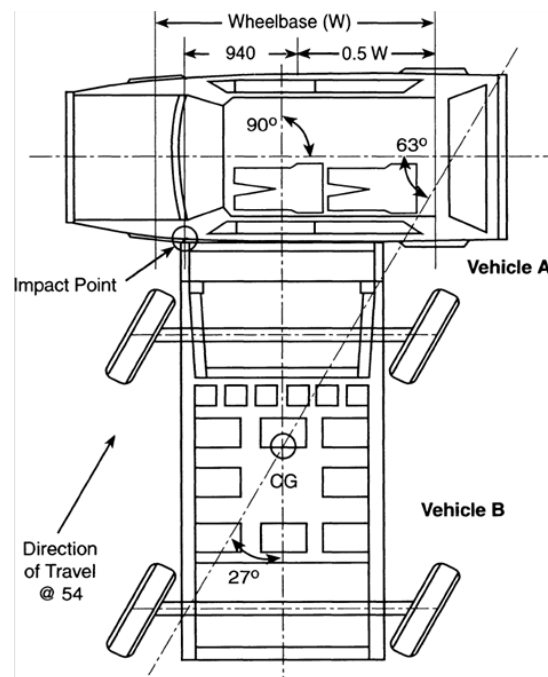


Figure 3-1. Test Configuration FMVSS NO. 214 Side-Impact, all dimensions in mm, velocity in km/h

According to the test conditions the vehicle is impacted by the MDB with a mass of 1.361 ( $\pm 4.5$ ) kg traveling at a velocity of 53.9 km/h. The MDB impacts the vehicle at a target angle of 27-degrees. Requirements for compliance to the test procedure are dummy injury criteria, fuel system integrity (FMVSS 301) and door retention.

### 3.2 Structural Requirements for FMVSS No. 214 Barrier Side-Impact

Initially the barrier is traveling at a velocity of 54 km/h. When the barrier impacts the vehicle, the side frame including rocker, roof rail, doors and B-pillar begin deforming. The barrier is decelerated by the contact force between barrier and vehicle, while the vehicle is accelerated. When the contact force reaches the crush load level of the barrier's honeycomb core, the



barrier begins to deform. Both vehicle and barrier consume a portion of the overall impact energy by deformation. Once the velocity of barrier and vehicle are equal, no further deformation can be observed and elastic spring back sets in.

### 3.2.1 Link Between Structural Design and Occupant Safety

For this project it was assumed that structural performance and occupant safety could be assessed separately. While interior components and restraint systems have a major influence on the dummy performance and thus on the actual occupant's safety, a certain level of structural performance is necessary to ensure that interior parts and restraint systems contribute in the intended manner. If the influence of the dummy on the structural performance is known or can be estimated, the structural and restraint performance can be integrated to yield the overall vehicle performance using principals of superposition. Following the approach of systems engineering this procedure in general allowed for a detailed understanding of the contribution of each component to the overall system performance. In addition, it allowed for the definition of an independent solution space for the single component that then can be designed and optimized individually.

Simulation performance is an additional reason for separating the structural design and assessment from the occupant safety assessment. Occupant safety FE models are computationally expensive, as they require a very detailed approach to contact modeling and feature a great number of degrees of freedom due to the dummy models and occupant restraint components (air bag inflation, belt sliding, etc.). Performing iterative design loops on a full vehicle simulation including dummy and restraint systems during the development of the B-pillar concept was not feasible.

For this project structural requirements were defined. These requirements deliver design targets that ensured a certain structural performance was achieved. It was assumed that when these requirements were met by the BIW structure and the simplified FE models respectively, it was ensured that the solution space to find a feasible restraint system configuration was sufficient.

The main structural design targets for side-impact were related to a required distance between a hard surface of the BIW or interior components and the occupant/dummy at certain points in time. It was assumed that when these minimum distance measures were not exceeded, the system allowed enough space for the air bags to deploy and protect the occupant in an adequate manner.

### 3.2.2 Functional Design Requirements

Distance measures were derived from the metal baseline small-sized production vehicle. Thus, meaningful requirements for the structural performance of the composite B-pillar could be transferred to UD-CCM.

Note that only maximum values for the B-pillar deflection are given in Figure 3-2. It was assumed that a stiffer structure – while causing more energy absorption in the barrier – would yield positive influence on the dummy loading conditions. However this was not always true, since a higher load level during impact leads to greater acceleration of the car and thus the gap between any hard structure and the occupant/dummy may close faster. Figure 3-3 shows the z-locations of the considered points for deflection measurement.

points in time			deflection requirements
$t_1$	critical point in time	$t_f + 3 \text{ ms} = 9 \text{ ms}$	$d_{\text{cfrp}} \leq d_{\text{steel}}$
$t_2$	critical point in time	$t_f + 5 \text{ ms} = 11 \text{ ms}$	$d_{\text{cfrp}} \leq d_{\text{steel}}$
$t_3$	critical point in time	$t_f + 8 \text{ ms} = 14 \text{ ms}$	$d_{\text{cfrp}} \leq d_{\text{steel}}$
$t_4$	critical point in time	35 ms	$d_{\text{cfrp}} \leq d_{\text{steel}}$
$t_5$	maximum deflection	-	$d_{\text{cfrp}} \leq d_{\text{steel}}$

Figure 3-2. Intrusion Requirements at Certain Crucial Points in Time

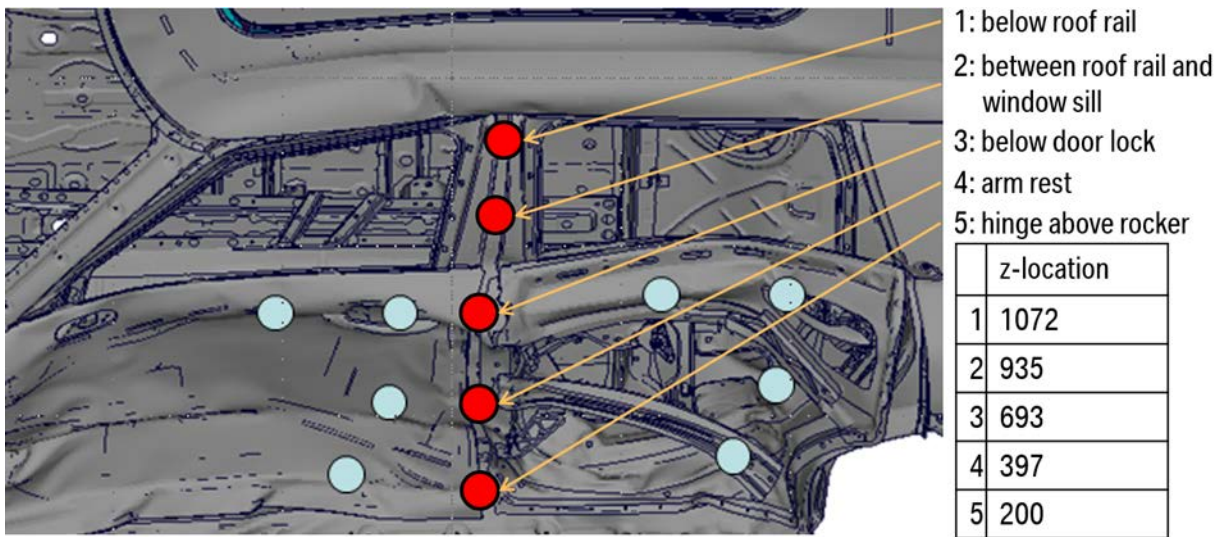


Figure 3-3. Locations of Considered Intrusion Measurements on B-Pillar

To confirm this assumption, a side frame stiffness study was performed on the original baseline vehicle model in a fully integrated dummy/restraint/structural FE analysis (FEA). The thickness of relevant components of the vehicle side frame and floor structure, including the B-pillar, the roof and the rocker were scaled to achieve both a stiffer (meaning less B-pillar deflection) and a weaker (meaning greater B-pillar deflection) variant that were then both compared to the baseline model.

The results of this side frame stiffness study led to the conclusion, that a stiffer side frame does not generate a negative influence on the dummy's rib intrusions. This project however was limited to the rib intrusion values measured by the dummy model. Further dummy measures as well as possible impact on the structural performance in other load cases were not evaluated.

### 3.2.3 Geometrical Design Requirements

In addition to the functional requirements, a geometrical outer shape was defined that would not be exceeded by the composite B-pillar. This requirement ensured the comparability between the composite B-pillar and the metal baseline in terms of geometrical stiffness. In

addition it ensured the compatibility of the CFRP B-pillar with the vehicle side frame structure and doors.

The shape of the baseline metal B-pillar was adopted as the geometrical outer boundary for the design of the composite B-pillar. The baseline metal B-pillar featured a hole in the lower inner region, which was necessary to enable the integration of the seat belt retractor into the metal B-pillar. The implementation of a composite B-pillar concept in this vehicle would have necessitated consideration of integration of the belt retractor. This would have led to increasing complexity of the design model (the retractor has an influence on the structural performance of the B-pillar) and require additional effort in the production of the B-pillar. For a generic vehicle concept, the retractor must not necessarily be integrated into the B-pillar (potential alternative locations might be: seat integrated retractor, roof or floor-mounted retractor, etc.). The specific location of the belt retractor has not been included in this project, meaning the composite B-pillar is not required to feature a hole or a certain space for the integration of a seat belt retractor.

### 3.3 Structural Requirements for CFRP Components in a Crash Load Path

Conventional vehicle structures consisting of metals have a long history of crash design. The requirements for structural integrity are well established and the criteria for fulfilling these are known. As a general rule one does not allow significant rupture in load paths, connections such as spot welds or in the structures of the occupant compartment. This standard ensures a certain degree of robustness in the crashworthiness of a vehicle.

Vehicles made of lightweight materials such as CFRP are no new innovation. There is a long history of using CFRP for racing cars or in low-volume super sports cars. In contrast to normal series production, these vehicles may have differing requirements for passive safety and are not necessarily tested by consumer protection authorities. Nevertheless, CFRP occupant cells have shown good response to crash tests as well as field accidents and even benefits compared to metal structures. CFRP currently used in series production is usually limited to individual vehicle components, such as the roof panels. The large scale use of CFRP in crash-relevant vehicle structures (main load paths, occupant compartment) demands a new approach for structural integrity.

The requirement of minimizing significant damage – as used in the structural the design of metals for crash requirements – is no longer suitable for CFRP structures, where energy dissipation involves splintering, in contrast to plastic deformation of steel structures.

BMW's goal was to ensure a crash design that exploits the advantages of CFRP and other lightweight materials in order to maintain or even improve the level of crashworthiness compared to conventional vehicles. This goal was achieved by the clear definition of the structural behavior, dependent upon the crash zone and combination of material and geometry used.

#### 3.3.1 Structures in Crash Management Systems

The requirements for structural integrity depend on the material used, the energy dissipation zone and the geometry of the considered structural component. In order to specify those requirements, it is necessary to provide the following definitions:

- Membranes or panels are parts, formed by surfaces, whose thickness is small compared to their remaining dimensions. Examples are the roof, floor panel, bulkhead, etc.

- Profiles are parts with a significant length/width-ratio. Examples are the rocker panel, roof rail, A-, B-... pillars, engine support beams etc.

### 3.3.2 Energy Dissipation Zones

Each structural component of a crash management structure was assigned a so-called energy dissipation zone. These zones were assigned to structural components in regard to their location as well as their contribution to crashworthiness of the structural crash management system. The description of the energy dissipation zones is illustrated in Figures 3-4, 3-5, 3-6, and 3-7 for the front part of the vehicle including the A-pillar. An equivalent classification of energy dissipation zones was also defined for the rear and side parts of the vehicle.

#### **Zone 1: Front-End – Bumper and Crash Boxes**

In Zone 1 plastic deformation was allowed (Figure 3-4). Separation or damage of the bumper cross-beam or the crash boxes was acceptable as long as function and continuous energy absorption was maintained by the subsequent structures.

#### **Zone 2: Longitudinal Beams to Suspension Turret Including Sub-Frame Front Area**

In Zone 2 plastic deformation and damage within deformed components were acceptable (Figure 3-5). Separation or damage of the load paths was to be minimized. The first front sub-frame connection to the longitudinal beams and the front branch of the suspension turret could separate to enable more deformation in the main load path and therefore increase energy absorption.

#### **Zone 3: Longitudinal Beams Between Bulkhead and Suspension Turret including Sub-Frame Rear Area**

In Zone 3 plastic deformation and damage within deformed components were acceptable (Figure 3-6). Separation or damage of the load paths was to be minimized. Separation of the different load paths (front sub-frame to longitudinal beams, suspension turret to longitudinal beam) was to be minimized. This enabled protection of the “Life” cell.

#### **Zone 4: “Life” Cell – Bulkhead, Side Frame**

In Zone 4 deformations were allowed (Figure 3-7). Significant damage was to be minimized. The detailed description of acceptable crash behavior in this zone is enclosed in the next section.

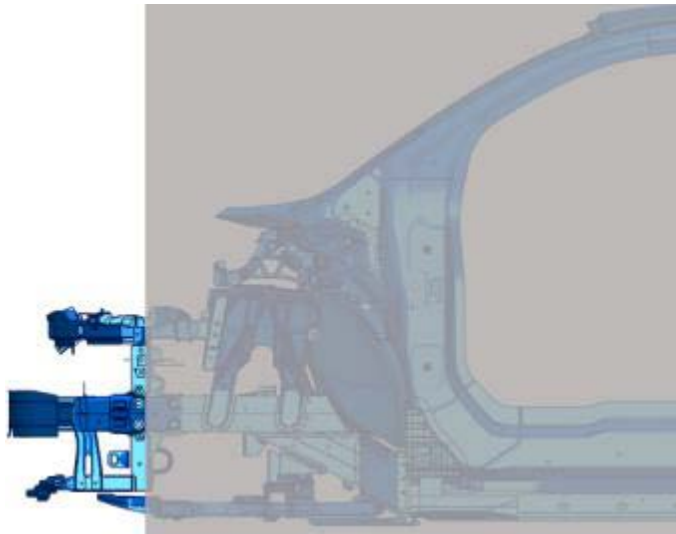


Figure 3-4. Crash Zone 1

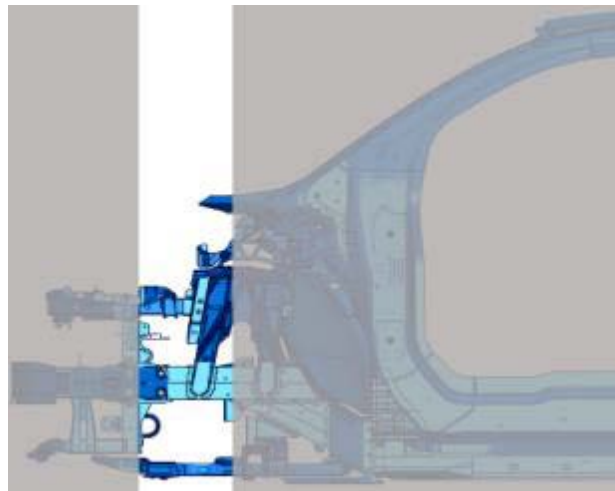


Figure 3-5. Crash Zone 2

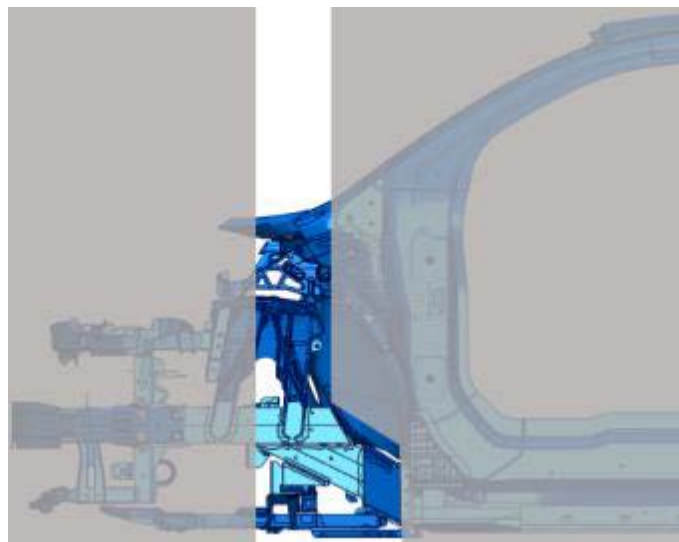


Figure 3-6. Crash Zone 3

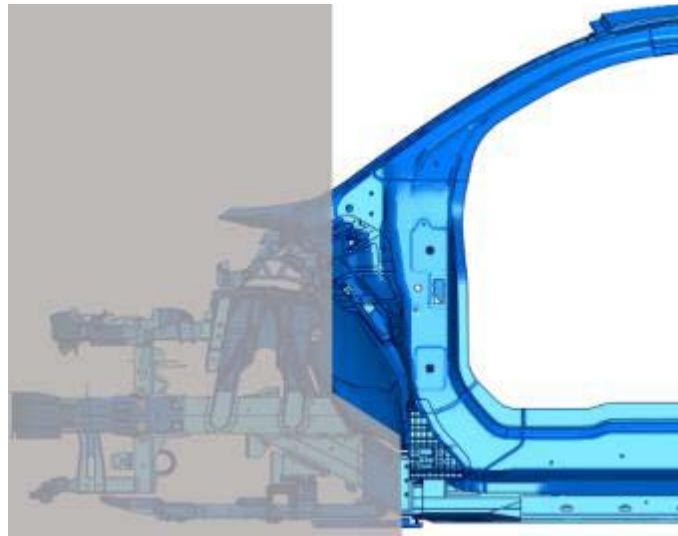


Figure 3-7. Crash Zone 4

### 3.3.3 Materials

As mentioned before the criteria to ensure structural integrity of a component depended upon:

- Geometry (membranes, profiles),
- Energy dissipation zone (1-4), and
- Material (ductile metals, metal castings, CFRP).

Regarding the requirements for structural integrity in an impact event, materials were treated differently with respect to their mechanical properties and fracture mechanics.

- i. Ductile metals are materials with high-fracture toughness and show a ductile rupture pattern. Examples are cold worked steel panels and extruded aluminum profiles.
- ii. Metal castings are materials with low-fracture toughness and show a brittle damage pattern. Examples are aluminum die-castings, sand castings, and magnesium-castings.
- iii. CFRP are carbon-fiber-reinforced plastics. As a material group CFRP can feature a range of different mechanical properties depending on the used fiber, matrix, layup, manufacturing process, etc.

Since the requirements for structural integrity for metallic structures are well known and with respect to the topic of this project, the following explanations focus on an occupant compartment, primarily consisting of CFRP structures.

The requirements for structural integrity in Zone 4 (occupant compartment) were the same for frontal, side and rear impact:

- Structural integrity after crash was given for:
- profiles made of CFRP located in a crash zone where damage was to be minimized (Zone 4), if a certain load bearing capacity was maintained for example by ensuring that several fiber layers remained intact;
- membranes made of CFRP as part of the Life cell (bulkhead, floor panel, roof...) if damage was minimized and/or splintering could be controlled (e.g., fiber layers in different directions); and

- connection of membranes and profiles made of CFRP (for example floor/rocker panel) if damage to the connection (adhesive, rivet, etc.) was minimized or was bridged by another (intact) structure.

While splintering in CFRP structures is acceptable, significant rupture in metallic structures (profiles and membranes) located in Zone 4 was to be minimized. As shown by the following test results, in contrast to metallic components, structures made of CFRP provide a significant amount of load bearing capability after being partially damaged by an impact event. A crack in metallic structures would be considered unstable and therefore may propagate uncontrollably without significant additional loading. In CFRP crack growth was stopped or heavily inhibited by undamaged fibers in the transverse direction.

In the examples shown, a small vehicle with crash relevant CFRP structures is considered. In spite of the occurrence of damage, for example in the bulkhead (in case of frontal impact) or the side frame (in case of side-impact), the intrusion level experienced by an occupant compartment made of CFRP is comparable to that of similar conventional vehicles (i.e., size and mass) made of steel. As Figures 3-8 and 3-9 show, the intrusion observed following frontal impact or side-impact (oblique pole), respectively, are in similar ranges.

The main challenge when assessing damage and splintering in CFRP structures is the determination of the degree of damage (i.e., are all fiber layers affected or are there still intact fiber layers). Usually one cannot determine this by a simple sight check. One possibility for appraising such undetermined damage is CT-scanning. In the past this was performed, for example, for typical damage and splintering in the bulkhead (Figure 3-10) after a frontal impact.

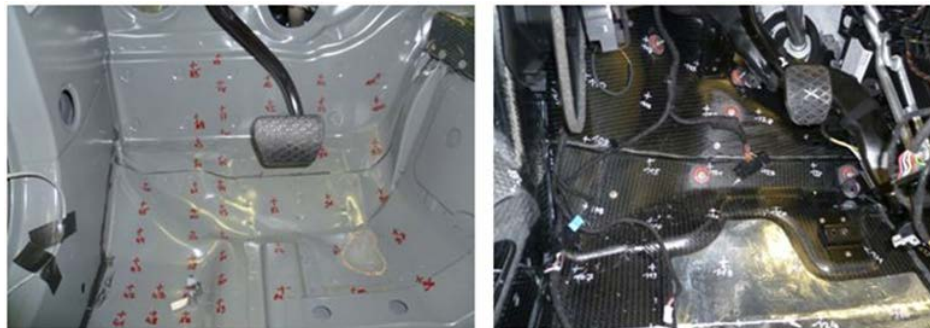


*Figure 3-8. Footwell After Frontal Impact, Steel (left) Versus CFRP (right)*





Figure 3-9. Occupant Compartment After Side-Impact, Steel (top) Versus CFRP (bottom)



Figure 3-10. CT-Scan of Splintering in Bulkhead After Frontal Impact

The results of the CT-scanning show that splintering in this area was not significant, i.e., many fiber layers were still intact. In the example shown in Figure 3-10, the splintering observed was classified as acceptable, as the majority of the fiber layers were still intact and thus still capable of load transfer to protect the occupants. The resulting documentation for characteristic damage modes in different laminate layups could be used as an assessment catalogue for further visual inspections.

### 3.3.4 Test Results: Second Impact on Damaged CFRP Components

Splintering can be accepted in CFRP structures due to the fact that CFRP structures maintain load bearing capacity, even after damage occurs. The fiber layer structure of membrane elements can provide a natural crack arrestor. Several test results confirm these assumptions, as shown in this section.

Considering the example vehicle in frontal impact (FMVSS No. 208, full frontal), the same test was executed with an increased load on the bulkhead. Although permitted splintering occurred



in case of the lower load impact, damage was only lightly increased in case of the higher load impact, as shown in Figure 3-11. The internal requirements for dynamic and static intrusion were fulfilled in both cases.<sup>1</sup>

Side-impact component tests showed similar results.

The experimental setup considered was a dynamic 5-point bending test with CFRP crash structures (roof rail and rocker panel), which approximated the impact of a FMVSS No. 214 oblique pole test (Figure 3-12).

The test was repeated on the same, now partially damaged, structure under the same conditions. The damage characteristics in the CFRP structures corresponded to those observed resulting from a FMVSS No. 214 oblique pole test. The structures were able to absorb the same amount of impact energy in the second impact, as shown in Figures 3-13 and 3-14. The measured load in the second test was missing the first peak resulting from initial damage of the composite. This led to a larger deformation on a level comparable to the crush force of the first impact. After unloading, the B-pillar was able to bear the impact weight after the drop and return to original geometry. Future work should investigate thermoplastics' ability to withstand multiple impacts. If this procedure were performed using metal structures, one would expect a considerable drop-off in the force level in the case of a significant rupture.

---

<sup>1</sup> Ferenczi, I., Kerscher, S., & Moeller, F. (2013). Energy Dissipation and Structural Integrity in Frontal Impact. Proceedings of the 23rd International Technical Conference on the Enhanced Safety of Vehicles (ESV), , Seoul, South Korea, May 27-30, 2013.



Figure 3-11. Footwell After Frontal Impact in CFRP Life-Cell With Lower (top) Versus Higher (bottom) Load Impact Energy

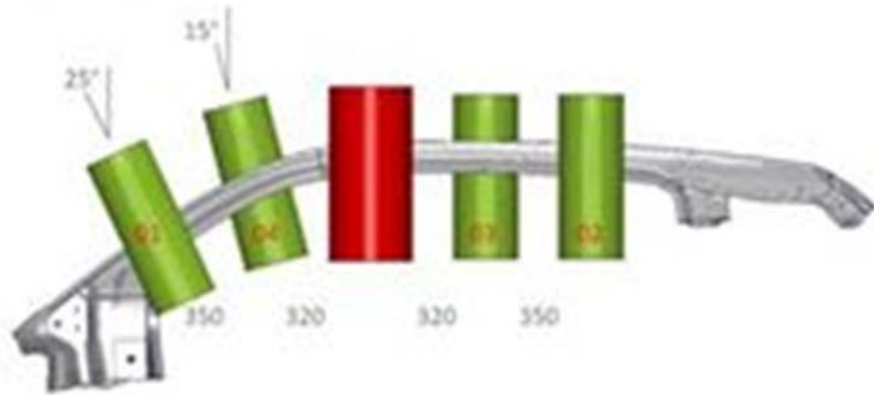


Figure 3-12. Component Test Setup Roof Rail

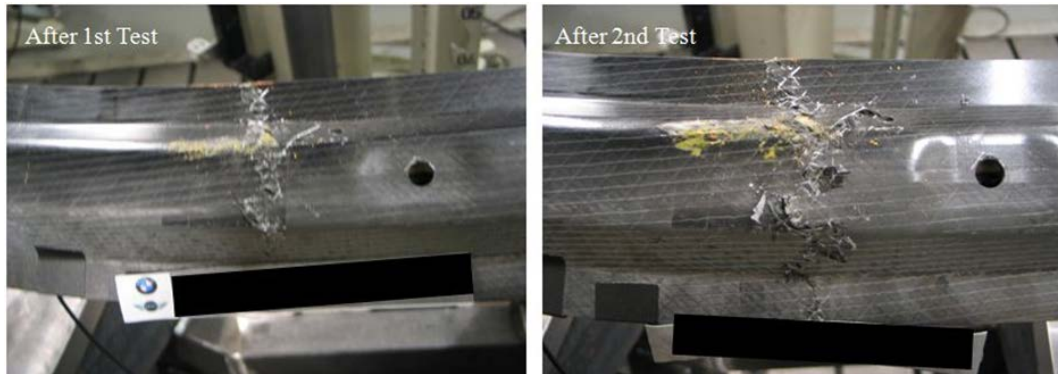


Figure 3-13. Roof Panel After 1<sup>st</sup> (left) and 2<sup>nd</sup> (right) Impact

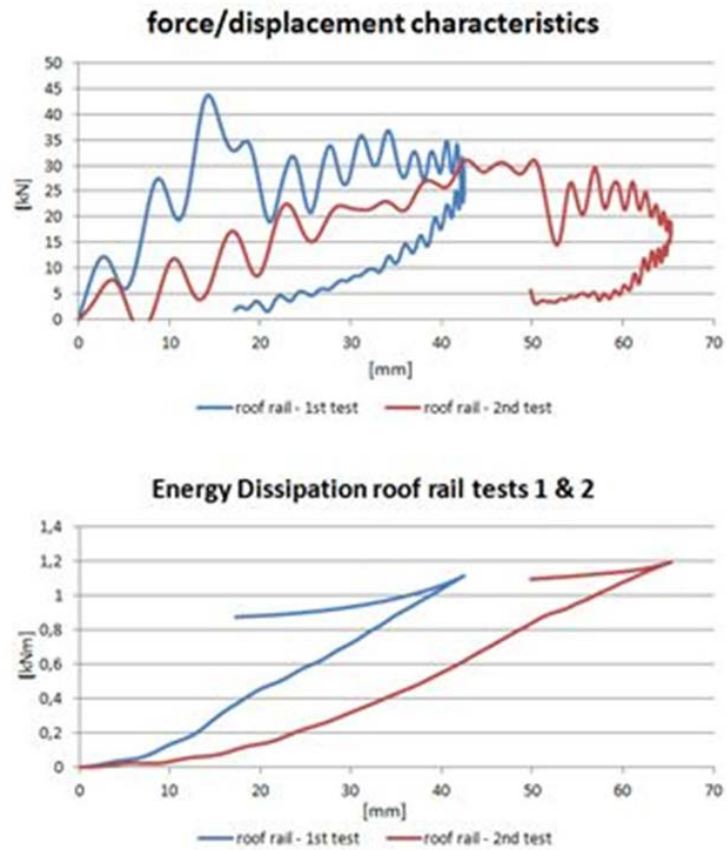


Figure 3-14. Load and Absorbed Energy Over Time of First and Second Impact Test

### 3.3.5 Summary

CFRP structures require different evaluation criteria when compared to structures comprised of ductile metals. Metal structures may collapse if the load continues after significant rupture occurs, whereas CFRP structures display ongoing load bearing capacity, even after significant splintering occurs. Furthermore, CFRP structures show different performance characteristics in regard to crack propagation. The fiber layer structure provides a natural crack arrestor as shown with the help of CT-scans and second impact testing.

Based upon these observations, CFRP can clearly be deemed a suitable material for crash applications, due to its specific mechanical properties. State-of-the-art crashworthiness requirements in terms of structural integrity can be fulfilled with CFRP structures, if its specific attributes are adequately considered in the design process.

## 4. B-Pillar Assessment Strategy and Models

---

As mentioned in Section 3.2.1, a design model needed to be developed that allowed for individual assessment of the composite B-pillar. An environment was derived, in which the compliance to the defined solution space, described in Section 3.2.2, could be assessed. This allowed for a rapid assessment of design changes in terms of structural performance.

Due to the long response time and high-computational effort, a fully coupled structural and occupant restraint simulation was not suitable for this project. Therefore, a simulation environment for single component structural assessment of the B-pillar, derived by BMW, is described in Section 4.1. This model was then used for iterative design simulations at UD-CCM as described in Section 6.

The initial strategy foresaw a detailed model validation by comparison of the composite B-pillar design model with the final hardware test results, as well as sub-component test results. This validated model was then intended to be integrated back into the full vehicle model, to generate performance feedback for the composite B-pillar design on the full vehicle level, followed by eventual design changes to the component. Due to several complications within the fabrication of the composite B-pillar specimens, which led to significant delays in the project progress, this validation loop could not be accomplished as initially intended within the given time constraints. However, the predictive design model of the composite B-pillar (prior to model validation based on sub-component test results and component test results) was investigated in vehicle simulations as shown in Section 8.

### 4.1 Derivation of Component Model

To be able to design and assess the B-pillar on a single component level, a reduced test setup was necessary. This setup met all requirements for a hardware component test and for a lean computational model with a short response time. The derivation process is shown in Figure 4-1.

Beginning with a detailed full vehicle representation, a process of simplification of the FE model was performed in multiple steps. The results of each further reduction were juxtaposed with those of its parent model in terms of kinematics and load distribution throughout the structure, to allow comparison of performance.

The influence of the interior components and restraint systems on the BIW deformation was captured by comparing the Stage 1 and Stage 2 simulation results.

Figure 4-2 shows a cross-section through the overlaying models Stage 2 and Stage 3. The deformation pattern of the Stage 3 model (blue) matched the deformation of the Stage 2 model over time.

The following list shows the major reductions in complexity that were performed during the derivation process:

- Isolation of the B-pillar and connecting structures roof rail and rocker.
- Restraint of B-pillar and connecting structure.
- Impact energy was reduced to meet the energy consumed by structural deformation of the B-pillar in the full vehicle simulation.



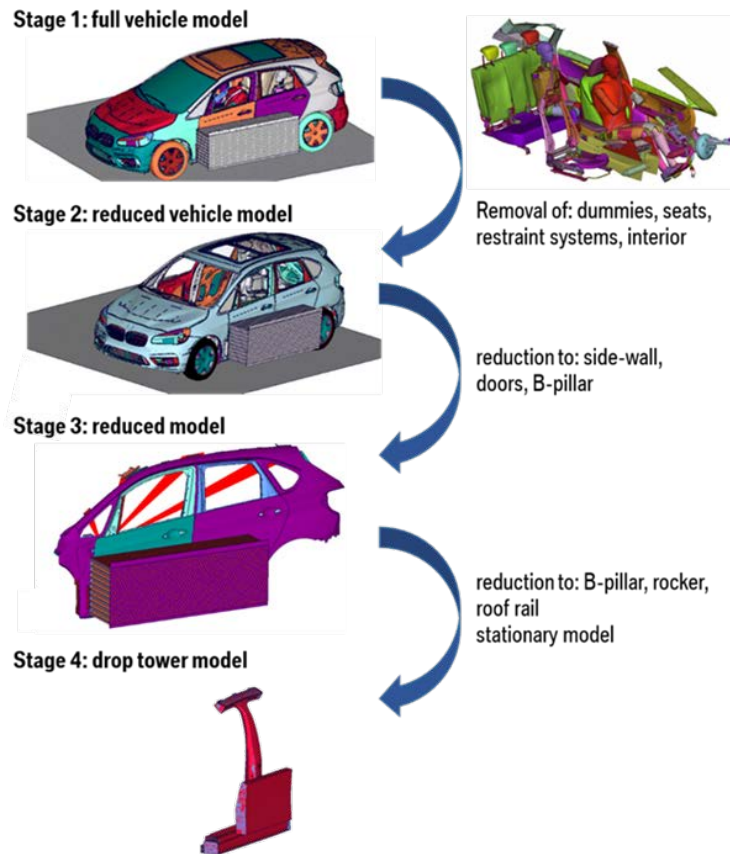


Figure 4-1. Derivation of Component Model

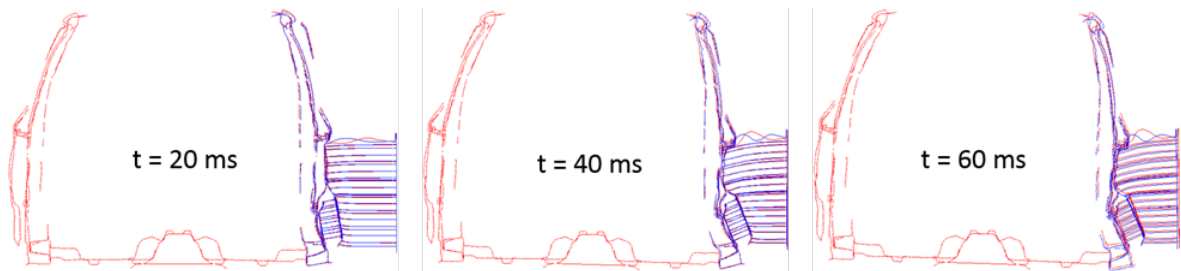


Figure 4-2. Comparison of Deformation Pattern Between Stage 2 and Stage 3 Model

- The MDB was replaced by a rigid impactor matching a similar deformation shape compared to the full vehicle simulation.
- Boundary conditions for the connecting support structure and the impactor were derived from FEA to obtain a similar deformation pattern compared to the full vehicle.

The resulting drop tower component model is described in detail in the following sections.

## 4.2 Analytical Calculation of Deformation Energy

The energy consumed by deformation during the FMVSS No. 214 side-impact crash test can easily be estimated by applying the principal of conservation of momentum in a closed system, while neglecting the rotational movement of barrier and vehicle due to the angular impact.

The point in time of interest is  $t_1$  in Figure 4-3 at which the deformation of vehicle and barrier reached their maxima and before elastic rebound began. At this point in time the vehicle and the barrier travel at the same velocity.

$$v_{B,1} = v_{V,1} = v_1$$

$$\frac{m_B v_{B,0} + m_V v_{V,0}}{(m_B + m_V)} = v_1$$

The remaining kinetic energy at this point in time is then

$$E_{kin,1} = 0.5 \cdot (m_B + m_V) \cdot v_1^2$$

thus,

$$E_{defo} = E_{kin,0} - E_{kin,1} = 0.5 \cdot (m_B \cdot v_{B,0}^2 - (m_B + m_V) \cdot v_1^2)$$

### 4.3 Definition of Loading and Boundary Conditions for the Component Model Using FEA

A final assessment of the designed composite B-pillar was a drop tower test performed at UD-CCM. Keeping this in mind, the design model on component level (Stage 4) was detailed meeting all requirements for a feasible hardware setup. Certain boundary conditions were defined by the need of a producible and practical hardware setup:

- Stationary B-pillar.
- Loading by impactor with defined mass and impact velocity yielding the impact energy.
- Restriction of impact velocity due to drop height.
- Restriction due to available drop mass.

Further boundary conditions were adjusted to achieve the best compromise between comparability to the more detailed FE models and practicability for the hardware tests.

- Impact energy (impactor mass and velocity).
- Boundary conditions (allowed degrees of freedom at the bearing points on roof rail and rocker).
- Impactor design and direction of impact.

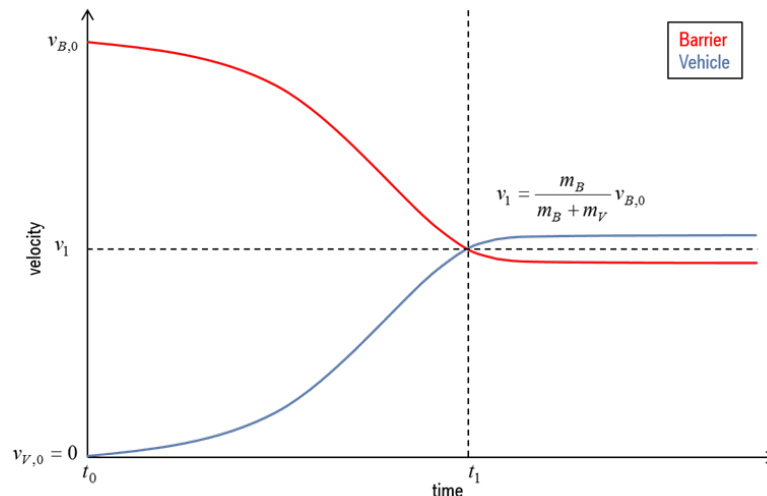


Figure 4-3. Velocity Versus Time of Vehicle and Barrier

In this section the definition of the latter arbitrary boundary condition for the Stage 4 drop tower model is described. For a description of the hardware test setup see Section 8.

## **Impact Energy**

Without further information describing the stiffness or respectively the force level between barrier and vehicle in detail, the energy consumed by the deformation of the vehicle cannot be determined.

An adequate estimation can be obtained by performing FEA of the full vehicle crash test. In a FEA different forms of energy can be obtained as an output for the whole model or for specified parts. Thus the amount of energy absorbed by the full vehicle during impact can be derived, as well as the portion of energy consumed by the B-pillar, the roof rail and the rocker, respectively. This led to an impact energy of 15.2 kJ.

To achieve an analogous B-pillar deformation over time to that observed in the full vehicle model, mass and velocity of the impactor were adjusted while maintaining the impact energy. This procedure was restricted by the height of the (hardware) drop tower, which limited the achievable velocity as well as by the available drop mass. For the final Stage 4 drop tower model a configuration of  $m = 375 \text{ kg}$  and  $v_0 = 9 \text{ m/s}$  (32.4 km/h) was chosen.

## **Boundary Conditions**

Determining adequate boundary conditions for the component model was essential to obtain comparable loading in terms of stress distribution throughout the B-pillar. Multiple FEAs were run with differing boundary conditions, and the resulting stresses and strains, as well as cross-sectional forces in the B-pillar and the connecting structure were compared with the results from the total vehicle simulation.

To ensure reliable and reproducible results for the entire series of hardware tests, simple boundary conditions such as clamped or simply supported were favored, compared to more complex kinematic or force-based boundary conditions. Forces can be measured more easily for clamped degrees of freedom using load cells.

## **Impactor Design and Direction of Impact**

After reducing the model to Stage 4 components, different impactor variants, as shown in Figure 4-4 were evaluated. A rigid impactor with a rotational degree of freedom along the vehicle x-axis was chosen due to mainly two reasons.

Initially, a segment of the FMVSS No. 214 barrier as impactor was investigated. This investigation showed that the missing doors in the drop tower model led to a different stress distribution on the barrier surface, which in turn led to different deformation and lower force level during barrier deformation. Instead of displaying a more even force distribution due to contact between doors and barrier, in the component model the barrier was involved in direct contact with the B-pillar. Figure 4-5 shows a z-cross-section of the deformed shape of the barrier in the Stage 3 model in blue and the deformed shape of the impactor Variant 1 in the drop tower model in red.



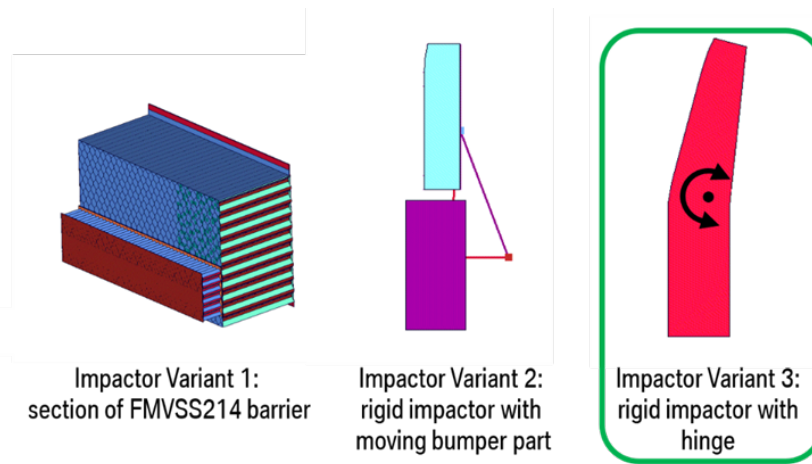


Figure 4-4. Evaluated Impactor Variants

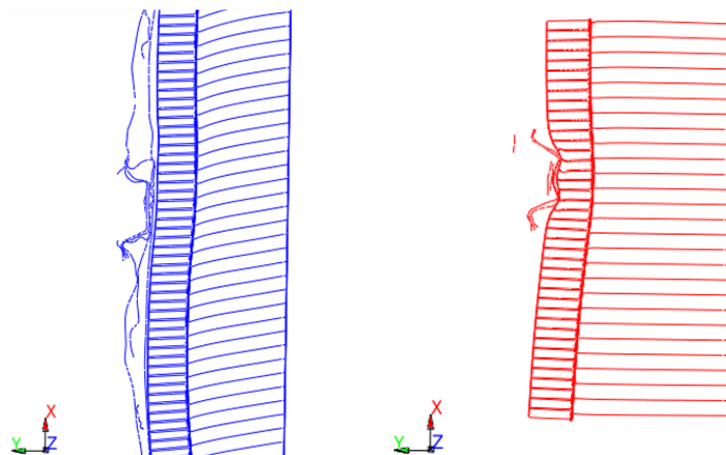
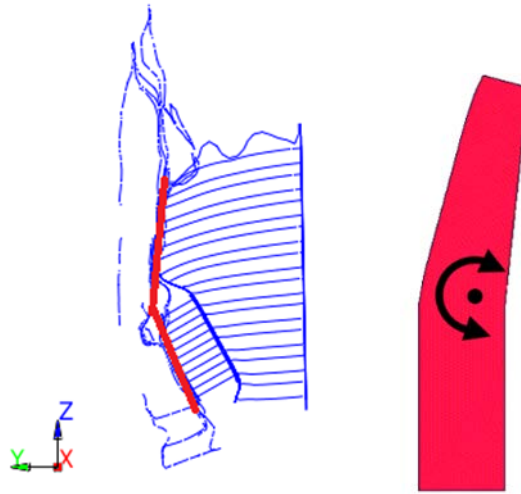


Figure 4-5. Cross-Section Showing Barrier - B-Pillar Interaction

The need to reproduce the same deformation as in the full vehicle simulation, despite the missing doors, led to the use of a rigid impactor. The second impactor variant featured two rigid segments connected by several hinges. The segments of the impactor represent the barrier's main block and the bumper region and allowed for relative motion between the two segments.

While Variant 2 yielded a good representation of the B-pillar loading compared to the Stage 3 model, this approach led to a rather complex impactor in the hardware environment of the drop tower. The force or moment-based couplings of different degrees of freedom of the segments required a very sophisticated impactor design. As mentioned above, in order to obtain meaningful results from the B-pillar test series, it was important to achieve reproducible test conditions and reliable measurements. Therefore, the complexity of the impactor was reduced in Variant 3.

The Variant 3 impactor represents the deformed shape of the barrier as shown in Figure 4-6. This impactor was found to be a good tradeoff between hardware test requirements and correlation of loading between the drop tower model and the Stage 3 reduced vehicle model.



*Figure 4-6. Comparison of Shape During Impact Between Impactor Variant 3 and MDB*

In order to reproduce the FMVSS No. 214 MDB loading in a drop tower environment, the impact direction had to be adjusted. An angled impact according to the FMVSS No. 214 test specifications would exert significant lateral forces on the test fixture, potentially leading to fixture damage.

The angled impact conditions cannot be neglected when occupant movement is considered and were accordingly taken into consideration in the full vehicle simulation. For the structural assessment of the B-pillar, however, this simplification was deemed adequate.

In addition, it should be noted that the design model featured an initial gap between the impactor and the B-pillar and rocker panel. This was incorporated to ensure the loading of the B-pillar in the drop tower design model (without side frame and doors) began at the same point in time compared to the vehicle model. Thus a close match in the intrusion history was achieved between the drop tower model and the vehicle model. In order to ensure comparability with the hardware test results, this time shift must be added to the  $t_0$  condition of the first contact between impactor and B-pillar.

## 5. Material Selection and Test Data for Design

Carbon fiber reinforced thermoplastics were chosen as candidate materials for the design, analysis, prototyping, test and evaluation of a B-pillar, with the goal of assessing computational design and analysis tools for crash worthy automotive composite structures. This section documents material sourcing and selection, property screening and measurements, development of material property cards for design and analysis and finally adhesion/joining method development during this project effort.

A number of carbon fiber thermoplastic material choices are currently available in the marketplace, with a variety of carbon fiber and thermoplastic resin choices and material forms. An initial assessment was performed to evaluate material forms and thermoplastic resin combinations with potential for scalable manufacturing processes in the automotive industry. Table 2-1 shows the variety of material forms and resin choices available and potential material suppliers.

Carbon fibers are available in a variety of specifications, and with material cost being a significant driver for automotive applications, PAN (Polyacrylonitrile)-based fibers with Standard Modulus were chosen for an optimal mix of cost versus performance. There are a number of fiber suppliers (Toray, Hexcel, Cytec, etc.) and the choice of fiber supplier was left to the material form supplier, so long as the fiber met the Standard Modulus specification documented in the next section.

A wide variety of thermoplastic resins are available with a range of performance metrics (see Table 2-1). The most common requirement for resin systems in composite structures is service temperature. Figure 5-1 shows Glass Transition ( $T_g$ ), Melt Temperature ( $T_m$ ) and Service Temperature ( $T_s$ ) for a variety of resin systems. A key decision was made early in this effort, to not impose e-coat temperature capability for this effort, as it requires dimensional stability at temperatures up to 177°C (350°F). This is specific to the painting process currently used in automotive production lines, and imposing this requirement significantly reduces polymer choices. After discussions with BMW, a service temperature requirement of 80°C (176°F) was set as the primary temperature requirement for thermoplastic resin selection. A second aspect of this effort was to demonstrate the potential crash performance of thermoplastics due to their high-toughness and elongation to failure compared to thermosets. Resin requirements were developed and are documented in the next section.

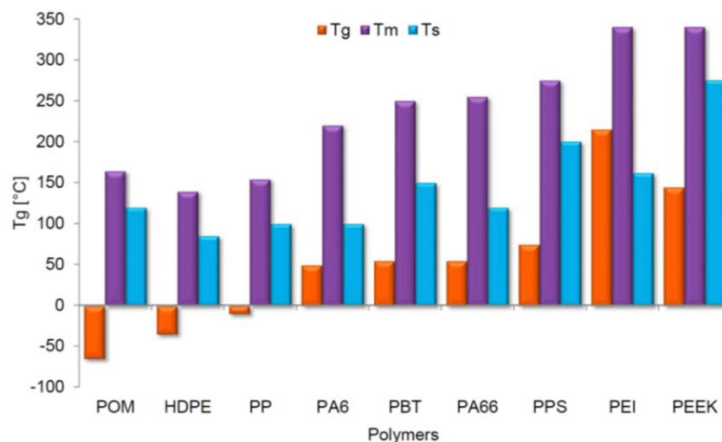


Figure 5-1. Temperature Capability of Various Thermoplastic Polymers

## 5.1 Carbon Fiber Thermoplastic Material Requirements

A Materials Requirements document, in collaboration with BMW, was created to source carbon fiber thermoplastic materials from suppliers in the composites industry, describing the fiber, resin and material form criteria for this effort. The following requirements were communicated to the supplier.

### Material Form

- Ready to use material forms to fabricate carbon thermoplastic B-pillar for automotive market
- Continuous fiber with thermoplastic resin
- Fiber architectures – no restriction
- Fiber loading >50 percent by volume
- Form manufacturing process must be scalable to large quantities

### Carbon Fiber

- Standard Modulus fiber
- T700 equivalent
- No preference of specific fiber or tow size
- Sizing compatibility left to supplier

### Thermoplastic Polymer

- Service Temperature: -30°C (-22°F) cold, 80°C (176°F) hot (in humid environment)
- High-toughness required (>10 percent elongation to failure)
- Provide data – tension modulus, strength and elongation to failure
- Exposure to standard automotive fluids (gasoline, etc.)
- 180°C (356°F) temperature exposure for short duration (1-2 mins) from painting. Not a major driver, would be nice to have

Within the scope of these requirements, the suppliers were allowed to provide multiple forms, resin choices, different fiber architectures, etc.

For each material choice provided by the supplier, they were asked to provide these items.

- Material form you choose to provide
- Brief description, datasheet
- Availability (small to large quantities)
- Widths, areal weight, resin content
- Nominal ply thickness per recommended process
- Resin impregnation level (full, partial etc. depending on form)
- Recommended process conditions for optimal quality
- Nominal composite properties (if available)
- Fiber type and supplier
- Fiber properties – datasheet, variability (std. dev. for properties)
- Sizing – polymer compatibility
- Preferred filament count for provided material form
- Nominal composite properties at 60 percent fiber loading

## 5.2 Material Selection Approach

A preliminary materials screening strategy was adopted for all materials sourced in this effort, to down-select promising candidate systems for detailed assessment and MAT54 material card development. The strategy centered around the measurement of three key mechanical properties.

- 0-degree tension for translation of fiber properties
- 90-degree tension for processed laminate quality and sizing or fiber-matrix adhesion
- $\pm 45$ -degree tension for in-plane shear and ductility assessment

In addition to these tests, ultrasonic scans for panel quality, fiber volume fraction and density measurements were performed for all material systems. Suppliers were given the choice of either providing material forms and process conditions or processed panels for these three properties.

## 5.3 Material Sourcing and Acquisition

Table 5-1 documents the various suppliers, material forms and/or panels provided. UD prepreg refers to unidirectional carbon fiber with pre-impregnated thermoplastic resin. The fibers are all aligned in one direction.

Table 5-1. Material Suppliers, Forms, and Processing Conditions

Supplier	Material Form	Material System	What was provided	Process Conditions
Cytec	UD Prepreg	AS4/PEI	UD prepreg tape	329°C, 30 mins, 150 psi
Tencate	UD Prepreg	AS4/Nylon-6	UD prepreg tape	271°C, 15 mins, 100 psi
Aonix	UD Prepreg	CF/Proprietary	Composite Panels	Proprietary
BASF	UD Prepreg	AS4/Nylon	Composite Panels	Proprietary
Concordia	Co-mingled	AS4/Nylon	Co-mingled Fabric	260°C, 15 mins, 150 psi
Arkema	Elium infusion resin	T700/Elium	Elium resin and CF fabric with compatible sizing	Room Temperature Infusion

A number of other suppliers were also contacted for materials, but were not considered in this effort (Celanese – similar material to Tencate and BASF Nylon-6 prepreg), did not participate in this effort either by declining to provide materials (Vector Systems, Fibertec), or did not have materials ready in time for this effort (SABIC, Zoltek, Barrday).

Suppliers that provided the material form (Tencate, Cytec, Concordia and Arkema) also provided processing conditions for each system, as shown in Table 5-1.

## 5.4 Processing, Microstructure and Quality Assessment

All material systems sourced were used to fabricate panels for the three screening mechanical tests or panels were directly provided by the supplier. For all the systems, microstructure evaluation was performed as a key metric to assess material form and processing influence on performance. The Cytec AS4/PEI system microstructure was selected as the target microstructure to be achieved, based on its high-mechanical performance. For each material system, the achieved microstructure is shown in the Table 5-2.

There are several interesting features to note: Tencate and BASF microstructures are similar, with fiber bundle clustering and non-uniform fiber distribution; similar microstructure was seen

for the Aonix system; Concordia co-mingled system showed poor microstructure due to fiber bundle alignment issues and weaving processes; Arkema system showed typical fabric microstructure with fiber tows based on the weave pattern and nesting.

Accordingly, one can expect the best properties from the AS4/PEI system, with reduction in properties as the microstructure gets more non-uniform. Additional assessments in the form ultrasonic scans, density measurements and layer thicknesses were performed for each system and corroborate the expectations of performance based on their microstructure.

## 5.5 Mechanical Property Characterization for Screening

An initial screening assessment was performed for all six systems based on the three mechanical tests documented previously and the results are shown in the Table 5-3. For all cases, test methods followed ASTM standard procedures.

Composite laminate configurations were as follows: 6-layers with 0-degree orientation  $[0]_6$  for 0-degree tension test (4 layers for Arkema due to non-crimped fabric), 8-layers with 0-degree orientation  $[0]_8$  for 90-degree tension test (6-layers for Arkema due to non-crimped fabric), and 8-layer symmetric cross-ply orientation  $[0/90]_{2s}$  for the in-plane shear test (samples cut in the 45-degree direction). For the 3518 standard, strain measurements past the 5 percent strain limit were performed using optical methods, as shear strains in excess of 60 percent were measured.

Table 5-2. Microscopic View of Material Systems Structure






<p>Cytec AS4/PEI from UD Prepreg Tape</p>	
<p>Tencate AS4/Nylon-6 from UD Prepreg Tape</p>	
<p>Aonix Carbon/Thermoplastic (Panels provided)</p>	
<p>Tencate AS4/Nylon-6 from UD Prepreg Tape</p>	
<p>Concordia AS4/Nylon-6 from Co-Mingled Fabric</p>	
<p>Arkema T700/Elium from Infusion of Non-Crimped Fabric</p>	

Table 5-3. Mechanical Testing Results

Supplier	Mechanical Test	Modulus (msi)	Strength (ksi)	Strain to failure (%)	Poisson's ratio
Cytec AS4/PEI	0 Tension (ASTM D 3039)	19.4 ± 0.20	349 ± 16.8	1.64%	0.33
	90 Tension (ASTM D 3039)	1.41 ± 0.03	7.83 ± 0.50	0.54%	-
	± 45 Tension (ASTM D 3518)	0.60 ± 0.02	22.9 ± 0.25	~30%	-
Tencate AS4/Nylon	0 Tension (ASTM D 3039)	14.56 ± 0.73	210.3 ± 11.6	1.43%	0.34
	90 Tension (ASTM D 3039)	0.7 ± 0.03	4.48 ± 0.38	0.72%	-
	± 45 Tension (ASTM D 3518)	0.21 ± 0.02	20.39 ± 1.32	>60%	-
Aonix	0 Tension (ASTM D 3039)	16.42 ± 0.68	280.5 ± 9.7	1.53%	0.32
	90 Tension (ASTM D 3039)	1.1 ± 0.02	3.86 ± 0.23	0.33%	-
	± 45 Tension (ASTM D 3518)	0.46 ± 0.02	15.84 ± 0.72	~40%	-
BASF AS4/Nylon	0 Tension (ASTM D 3039)	14.50 ± 1.07	201.4 ± 17.7	1.4%	0.36
	90 Tension (ASTM D 3039)	0.70 ± 0.09	4.33 ± 0.5	0.82%	-
	± 45 Tension (ASTM D 3518)	0.17 ± 0.02	10.58 ± 0.72	~45%	-
Concordia AS4/Nylon	0 Tension (ASTM D 3039)	13.35 ± 1.45	113.5 ± 8.36	0.86%	0.97
	90 Tension (ASTM D 3039)	0.91 ± 0.06	7.72 ± 0.21	1.23%	-
	± 45 Tension (ASTM D 3518)	0.62 ± 0.13	17.57 ± 0.04	2.8-7.8%	-
Arkema T700/Elium	0 Tension (ASTM D 3039)	17.71 ± 0.89	290.07 ± 14.6	1.52%	0.31
	90 Tension (ASTM D 3039)	1.14 ± 0.03	4.92 ± 0.30	1.23%	-
	± 45 Tension (ASTM D 3518)	0.52 ± 0.13	14.98 ± 1.02	~18%	-

A comparison of the measured properties led to the following conclusions:

1. The AS4/PEI system was the best performing system for tension properties with reasonable shear elongation.
2. Both Nylon prepreg systems (Tencate and BASF) were very similar in performance, with the Tencate system showing the best performance in shear. Very high-elongation (>60%) was measured showing remarkable ductility in this configuration.
3. The Aonix and Arkema systems also demonstrated very good tension properties, though the transverse tension performance was significantly lower than AS4/PEI.
4. The co-mingled system from Concordia showed poor overall performance due to poor fiber direction control in the weave and processing.
5. Microstructure tracked performance, as expected, with the best microstructure (AS4/PEI) performing the best. The Nylon systems (BASF, Tencate) had similar microstructure with resin rich regions, which may potentially be the cause for the high-shear elongation.
6. Comparing material costs, the PEI system was the most expensive at ~\$40/lb., compared to the Nylons (\$16-18/lb.) and Arkema (same as Nylons). The Concordia system was also relatively expensive (\$35/lb.) due to the cost of making the polymer fiber and the com-mingling process. However, the tape material forms require significant processing costs for



manufacturing tailored blanks and forming, compared to the co-mingled form which is readily drapeable and formed into the final geometry.

## 5.6 Material Selection for B-Pillar

The B-pillar design (detailed in Section 6) was a two-part design with a hat section adhesively bonded with a flat spine section. As shown in Figure 5-2, the pillar design was based on functionality of each zone/section of the pillar, with laminate stacking sequence and materials used chosen based on desired functional response. As shown in Figure 5-3, it is a non-cored hat-spine structure with tabbed end geometry. The hat section was designed to provide significant energy absorption capability under crush and a high-elongation system with  $\pm 45$ -degree laminate (such as the Tencate Nylon) in the hat vertical walls, transitioning to zero-degree on the top. The fiber orientations were chosen to maximize and tailor energy absorption under crash and details are documented in Section 6.

Based on the screening mechanical tests for the six material systems chosen, comparative charts for key properties are shown in Figure 5-4. They compare Tension Modulus, Tensile Strength, Shear Strength and Shear Strain with the first two properties representing key properties for the spine and the second two properties representing key properties for the hat section. The PEI and Arkema systems performed the best in spine critical properties, in that order and the Tencate Nylon system performed the best in shear for the hat critical properties. For the spine section, the Arkema system was chosen for two reasons: infusion-based manufacturing technique at significantly lower processing temperatures compared to PEI, and lower material cost. The Tencate Nylon system was chosen for the hat section, with thermoforming as the preferred manufacturing route. The two manufacturing processes chosen are both being considered for high-volume automotive composite production, with the High-Pressure Resin Transfer Molding (HPRTM) process already in production for the BMW i-series.

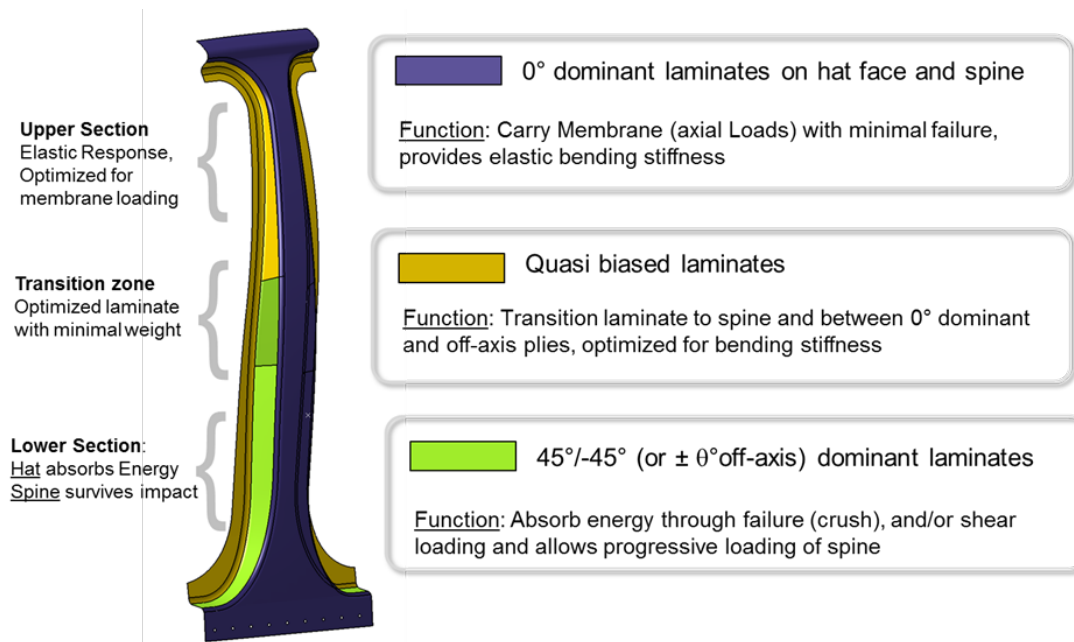


Figure 5-2. Pillar Design Zones and Typical Cross Sections

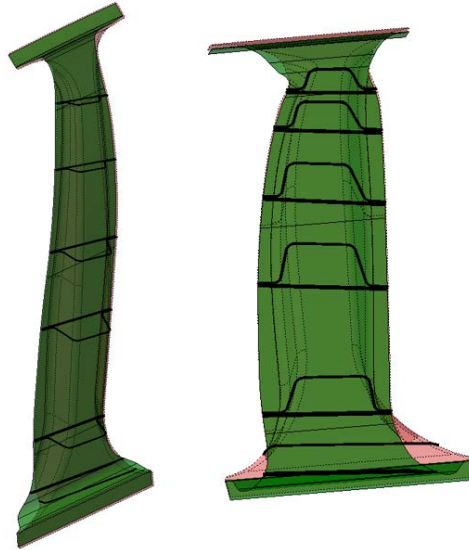


Figure 5-3. Pillar Section View

Additional material characterization was performed for the Arkema, PEI and the Tencate Nylon system to generate properties for material cards in design and analysis. This included compression and compression shear (+45-degrees in compression) as the hat section undergoes compression loading during impact. Measured properties are documented in Table 5-4.

A comparison of the key properties for the three systems of interest (PEI, Nylon and Elium) are shown in the radar plot (Figure 5-5) normalized to Nylon properties with several interesting implications:

1. For the spine critical properties, the PEI and Arkema system were more than 20 percent higher, with the PEI system showing the best performance.
2. Comparing the PEI and Arkema system, compression strengths were 2 and 1.7x higher than the Nylon system. Consequently, on a cost-weighted basis the PEI system can be twice as expensive and still give a lighter and cost-effective solution.
3. The Nylon system dominated hat critical properties with 3x higher shear elongation or ductility, which will be exploited in the design of the crushable section.

For the crushable hat section, one of the design challenges was the ply orientation or optimal energy absorption under shear compression, which was the expected loading mode under crash. The energy absorption capability for several laminate constructions were calculated by performing compression tests, and measuring the area under the load-deflection curve. As shown in the Figure 5-6, the  $[\pm 45]$  degree orientation absorbed the most energy with addition of 90-degree plies reducing the energy absorption capability and was the preferred orientation for the vertical wall section of the hat directly under the impact zone.

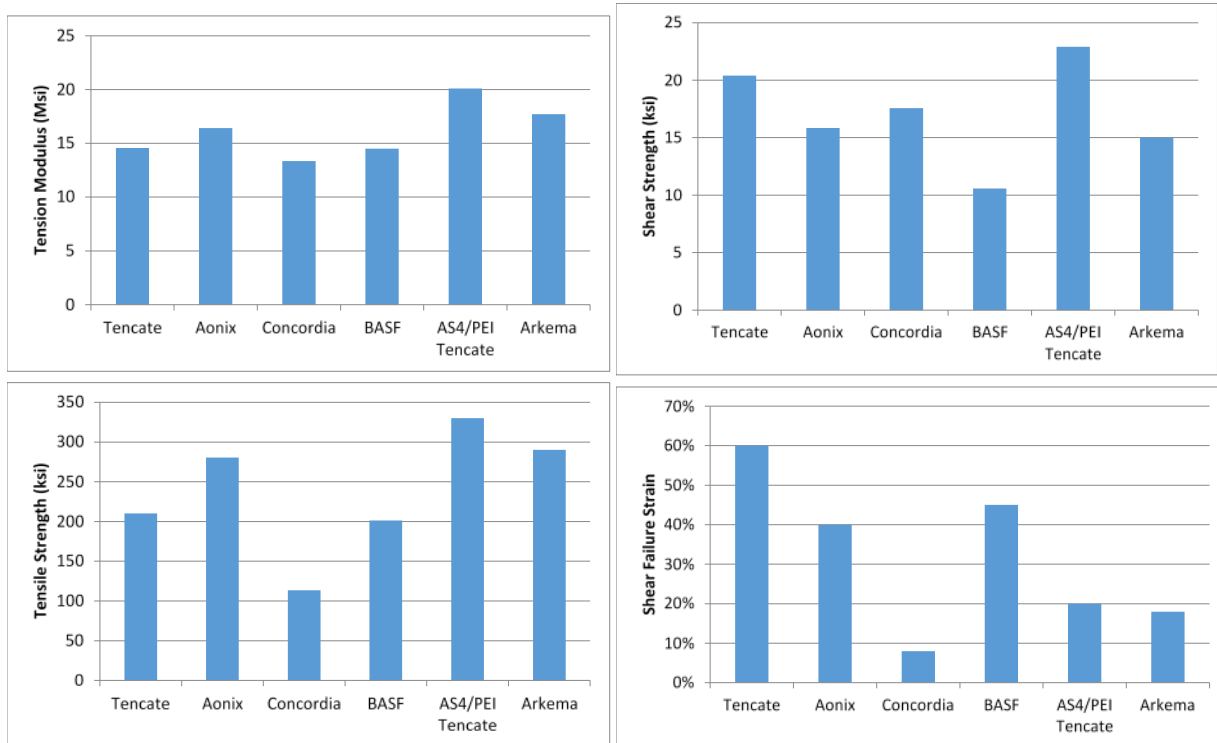


Figure 5-4. Key Properties of Material Systems

Table 5-4. Material Characterization

Supplier	Mechanical Test	Modulus (msi)	Strength (ksi)	Strain to failure (%)	Poisson's ratio
Cytac AS4/PEI	0 Compression (ASTM D 3410)	16.7 ± 0.6	176 ± 6.7	1.29%	-
	90 Compression (ASTM D 3410)	-	18.6*	-	-
Tencate AS4/Nylon	0 Compression (ASTM D 3039)	13.54 ± 0.50	82.79 ± 11.28	0.63%	-
	90 Compression (ASTM D 3039)	1.05 ± 0.05	16.03 ± 0.40	-	-
	±45 Compression (ASTM D 3518)	0.35 ± 0.02	10.84 ± 0.08	>60%	-
Arkema T700/Elium	0 Compression (ASTM D 3039)	15.78 ± 1.17	139.2 ± 7.94	1.43%	-
	90 Compression (ASTM D 3039)	-	10.97*	-	-

\*Values predicted from micromechanics

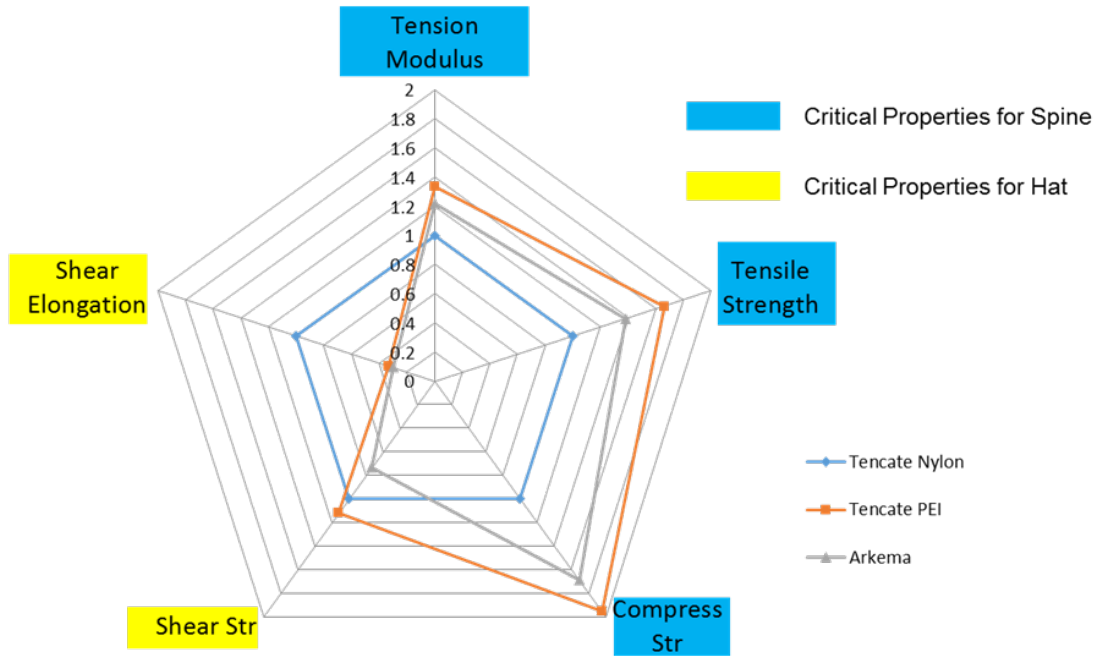


Figure 5-5. Key Properties of PEI, Nylon, and ELIUM, Normalized to Nylon Properties

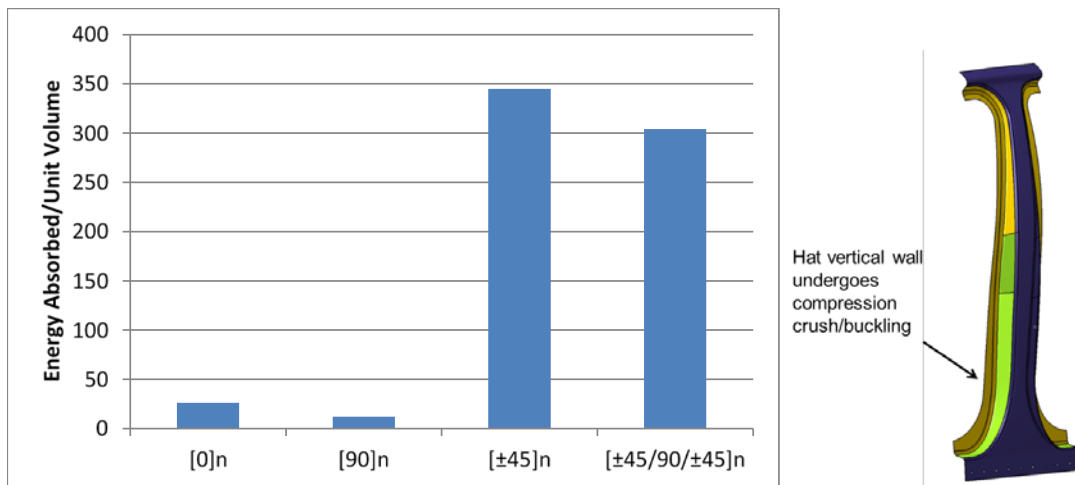


Figure 5-6. Ply Orientation and Energy Absorption

## 5.7 Material Card Generation for Simulations

UD-CCM used LS-DYNA composite damage model MAT54 for shell elements in the composite B-pillar design and analysis. Parameters of the MAT54 card are documented in Section 6.

## 5.8 Adhesive Bonding for Hat/Spine/Rail Joints

The proposed B-pillar design was a multi-material design with Nylon in the hat section, Elium in the spine section and steel for the top and bottom rails (Figure 5-7). Following manufacture of the hat and spines, an adhesive joining method would be used for assembly of the hat/spine and steel rails into the full-scale test article for drop tower testing. This required the selection of an adhesive system and appropriate pretreatments for compatibility to all three systems, joint strength assessment and failure modes, traction law development for modeling and simulation, and the final assembly process development. This section documents adhesive selection methodology and joint strengths and traction law development for the selected adhesive. Assembly methods and joining procedures are documented in Section 7.

## 5.9 Adhesive Selection

A number of adhesive systems were evaluated for bonding to thermoplastic resins and steel, with emphasis on high-elongation systems for crash performance.

BMW recommended two systems – DOW Betaforce (polyurethane-based) and Sikaforce 766 L30 (polyurethane), based on their experience with bonding thermoset composites on the BMW i-series. Of the two, the Sikaforce system is not currently sold in the United States and was not considered. Two other systems were selected by UD-CCM, based on prior experience – 3M AC240 (polysulfide-based) and Plexus MA530 (methacrylate-based). Both these systems are high-elongation systems with demonstrated performance in prior UD-CCM programs and are able to bond to a variety of surfaces.

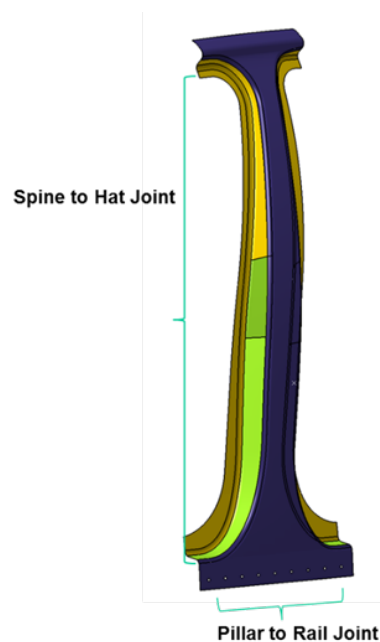


Figure 5-7. B-Pillar Design

Surface treatment is the main factor impacting adhesion strength in bonded joints and several surface preparation methods were evaluated – mechanical roughening, plasma treatment and adhesive-compatible primers.

## 5.10 Adhesive Bond Strength Assessment

Adhesion performance for the selected adhesives was performed with single lap-shear tests (ASTM D 3165). Coupons were prepared for bonding Nylon-Nylon, Elium-Elium and Steel-Steel in single lap-shear configuration. The standard lap-shear configuration was modified to include a 1.5 mm bondline to account for tolerances during assembly of the hat and spine, and with 5.08 cm (2 in.) overlap (1.27 cm in the standard) to more accurately reflect the actual joint configuration.

Lap-shear strengths for the selected combinations of adhesives and surface treatments were first performed for Nylon-Nylon and the results are shown in Table 5-5. All adhesive systems were cured per their manufacturer specifications. As seen from the results, Plexus provided good adhesion with Nylon and no primer or plasma treatment was necessary. The Plexus system also had a working life of 30-45 minutes, which was sufficient for assembling/bonding of the hat and spine sections.

Lap-shear tests were then performed with the Plexus system for all substrates with a 24-hour room temperature cure cycle, and the results of these tests are shown in Table 5-6. Delamination with good lap-shear performance was seen for all substrates. In addition, the 72-hour cure for the adhesive increased lap-shear strength by 30 percent that showed that a higher temperature cure (compared to room temperature) may be more suitable for the Plexus system.

Table 5-5. Lap-Shear Strength Results of Adhesive and Surface Treatment Combinations

Adhesive and Surface Treatment	Lap-Shear Strength (psi)	Failure Mode
AC240B-1/2, grit blast	132	Adhesive
Plexus MA530, grit blast	1084	Cohesive
TDS Betaforce, grit blast, plasma treat	443	Adhesive
TDS Betaforce, grit blast, Sika primer	412	Adhesive

Table 5-6. Lap-Shear Strength Results of Substrates with Plexus MA530

Substrates	Lap-Shear Strength (psi)	Failure Mode
Nylon-Nylon, grit blast	1084	Cohesive
Steel-Steel, grit blast, PC120 primer	1154	Cohesive
Elium-Elium, grit blast	1108	Cohesive
Elium-Elium, grit blast, 72 hrs	1373	Cohesive

## 5.11 Plexus MA530 Cure Cycle Development

Based on the 72-hour room temperature cure lap-shear test results, a modified higher temperature cure cycle could be developed to increase bond strengths. Cure kinetics were performed for the Plexus system using differential scanning calorimetry (DSC), and a 2-hour 50°C (122°F) cycle was selected to ensure complete cure of the adhesive. The proposed bonding cycle for both assembly and full cure of adhesive was as follows.

- 3 hours at room temperature in assembly fixture (30-45 minutes working time)
- 2 hours free standing cure at 50°C (122°F)

Using this cure cycle, all substrate adhesion tests were repeated and a transverse-tension test was also performed and the results are shown in Table 5-7. The transverse tension strength and load-displacement curve was based on ASTM (American Section of the International Association for Testing Materials) C 297, the Standard Test Method for Flatwise Tensile Strength of Sandwich Constructions, and measured using 5.08 cm (2 in.) aluminum blocks for simplicity, so long as the failure mode was cohesive.

An increase in lap-shear strengths of 40 percent was seen for all substrates with the modified adhesive cure cycle, as compared to the standard 24-hour room temperature cycle. Measured data and load-displacement curves were used to generate a traction law for the adhesive. The methodology to generate the traction law is documented in Section 6.

A final aspect of the adhesive bonding study was the effect of adhesive working time on bond strength. Lap-shear tests were performed on Nylon-Nylon at different out times to assess change in bond strengths as a function of out-time. Out-time refers to the time the mixed adhesive was dispensed on the substrate surface prior to the surfaces being bonded together.

Lap-shear results, shown in Table 5-8, showed that a maximum of 20 minutes was available for adhesive dispensing and assembly of the hat, spine, and rails.

## 5.12 Summary

Carbon fiber thermoplastic materials were sourced and property characterization performed to identify candidate material systems for the B-pillar. Two different materials were chosen based on functional design, for the two-part pillar – Tencate AS4/Nylon for the hat section, and the Arkema T700/Elium system for the spine section. The Nylon system demonstrated high-ductility in shear and the Elium system was a cost-effective solution for the spine section dominated by tension/compression properties. MAT54 material cards in LS-DYNA were developed for the selected material systems for design and analysis of the pillar. Adhesive studies identified the Plexus MA530 system as suitable for all substrates (Nylon, Elium and Steel), and a modified bonding cycle was developed, followed by traction law development.

Table 5-7.Substrate Adhesion Test Results

Substrates	Test	Strength (psi)	Failure Mode
Nylon-Nylon, grit blast	Lap-Shear	1467	Cohesive
Steel-Steel, grit blast, PC120 primer	Lap-Shear	1501	Cohesive
Elium-Elium, grit blast	Lap-Shear	1467	Cohesive
Aluminum-Aluminum	Transverse Tension	1668	Cohesive

Table 5-8.Lap-Shear Test Results

Substrates	Lap-Shear Strength (psi)	Failure Mode
Nylon-Nylon, grit blast, grit blast baseline (~5 minutes)	1467	Cohesive
Nylon-Nylon, grit blast, 0 minutes	1614	Cohesive
Nylon-Nylon, grit blast, 20 minutes	1417	Cohesive
Nylon-Nylon, grit blast, 30 minutes	1289	Cohesive-Adhesive

## 6. Design and Analysis

### 6.1 Introduction/Background

#### 6.1.1 Objectives and Approach

Design and analysis procedures for a composite B-pillar have been presented. BMW has provided a reduced baseline metal B-pillar impact model that has been used as a platform for composite design that will satisfy all design criteria set by BMW in earlier section. Present design and analysis will be carried out by modifying the baseline metal impact model to accommodate the composite B-pillar subjected to identical impact conditions as baseline. At every stage of composite design and analysis procedure, results would be compared to the baseline metal impact model to ensure that all design criteria were met.

#### 6.1.2 BMW Metal Baseline Reduced B-Pillar Impact Model

Following the reduced analysis methodology developed by BMW, a metal baseline reduced B-pillar impact model for LS-DYNA environment was delivered to UD-CCM. LS-DYNA impact analysis of the metal baseline was conducted with the initial mass, velocity, and energy determined by BMW ( $M = 375.31 \text{ kg}$ ,  $V = 9.00 \text{ m/s}$ , &  $E = 15.20 \text{ kJ}$ ) that matched the design requirements. Figure 6-1 shows different views of the metal baseline and Figure 6-2 shows the maximum dynamic deformation/intrusion occurred at time  $t = 34 \text{ ms}$ .

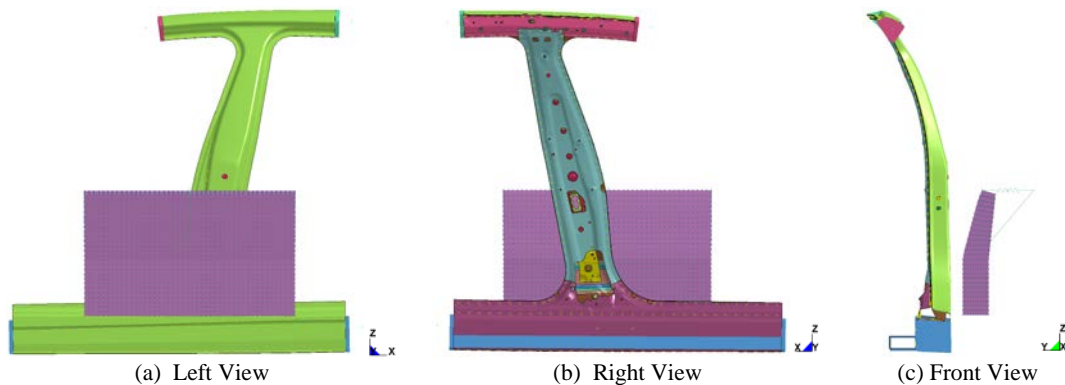


Figure 6-1. Different Views of Metal Baseline Reduced B-Pillar Impact Model  
Impact Mass,  $M = 375.31 \text{ kg}$ . Impact Velocity,  $V = 9.00 \text{ m/s}$

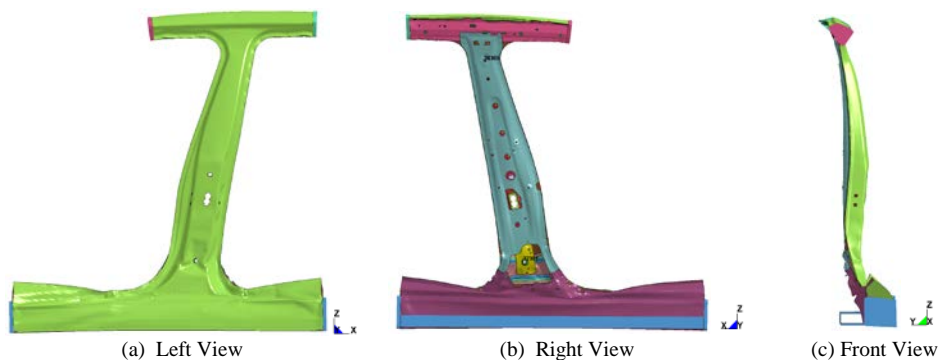
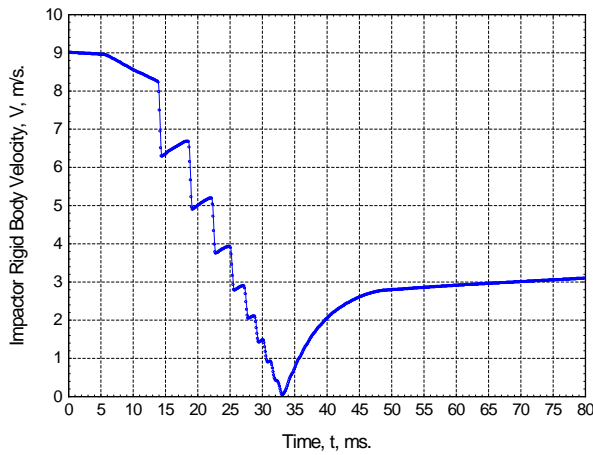


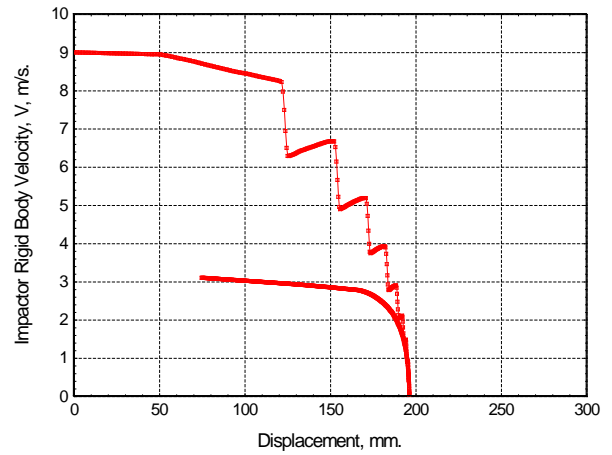
Figure 6-2. Different Views of Deformed Metal Baseline Reduced B-Pillar Impact Model  
Time,  $t = 34 \text{ ms}$



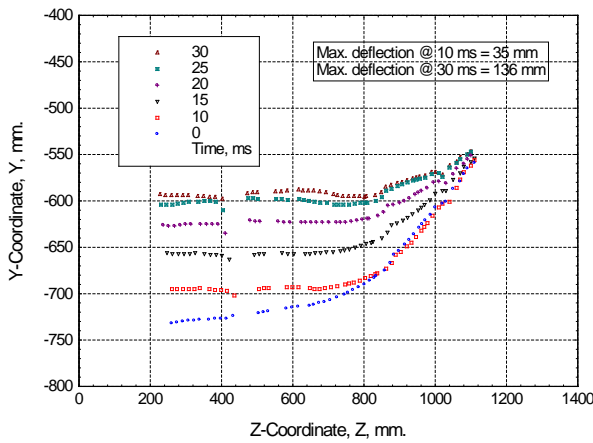
From the metal baseline model, several key results were extracted and presented in Figure 6-3. Key design parameters were identified from these results and are presented in the next section.



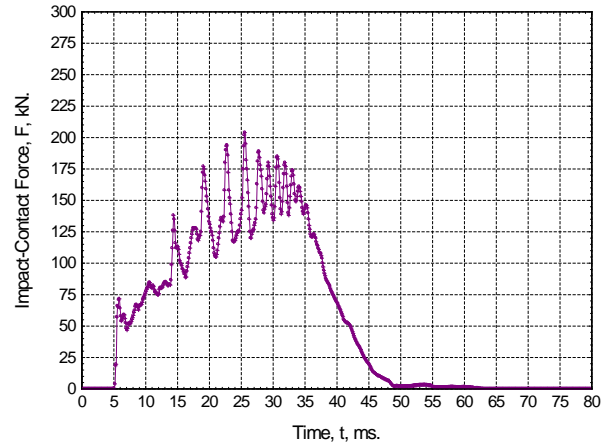
(a) Impactor RBV vs. Time.  
 $V = 0$  @  $t = 33$  ms,  $V_R = 3.1$  m/s.



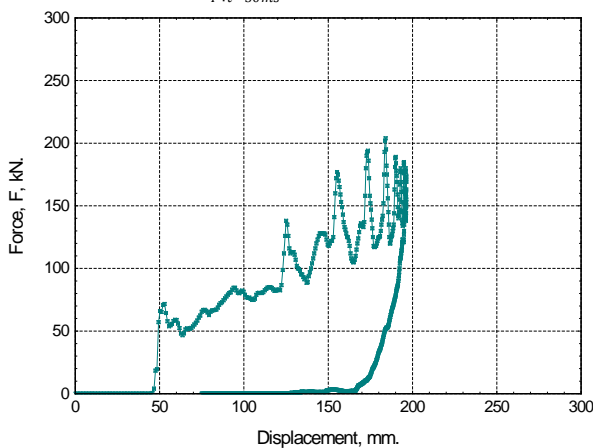
(b) Impactor RBV vs. RBD.  
 $u_Y|_{\max} = 196$  mm.



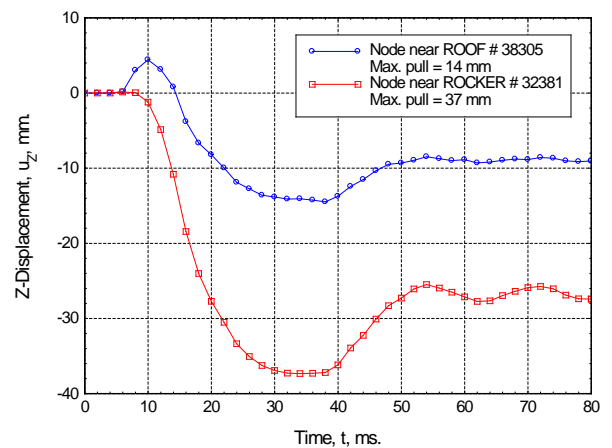
(c) B-Pillar Intrusion at Different Time.  $u_Y|_{t=10\text{ms}} = 35\text{mm}$ ,  
 $u_Y|_{t=30\text{ms}} = 136\text{mm}$ .



(d) Impact-Contact Force vs Time. Impulse  $p = 4377$  kg-m/s.



(e) Impact-Contact Force vs. Impactor RBD. Work done  $W = 13316$  J.



(f) Vertical pull down of the B-Pillar near Roof & Rocker.

Figure 6-3. Quantitative Design Requirements for the Metal Baseline Reduced B-Pillar Impact Model

In the metal baseline model, (i) impact-contact is established at time  $t = 5ms$ , (ii) the impactor velocity was reduced to zero at time  $t = 33ms$ , i.e., time required to stop the impactor was about 28 ms, (iii) the impactor rebound with a rebound velocity of  $V_R \approx 3m/s$ , and (iv) the impact-contact force reduced to almost zero at around  $t = 50ms$ , i.e., the impact contact duration was about 45 ms. Impact-contact force is plotted against the impactor Rigid Body Displacement (RBD) and the total work done was calculated to be  $W = 13.316kJ$  as compared to the impact energy of  $E = 15.20 kJ$ . Maximum intrusion of the back face of the metal B-pillar at Z-coordinate  $Z=400$  mm was found to be 35 mm (where contact between impactor and the B-pillar assembly was established at around 5 ms), and at 30 ms a maximum intrusion of 136 mm was measured. Note that the rigid body displacement of the impactor (center of gravity at  $z = 230$  mm) causes the crush of the front face of the B-pillar and the dynamic displacement of the back face of the B-pillar is a measure of intrusion. The difference between the impactor and the maximum intrusion is a measure of relative crush of the B-pillar.

### 6.1.3 Design Requirements for Composite B-Pillar

While the detail design requirements have been discussed in Section 3, the data presented in Figure 6-3 was compared with the composite design solutions.

## 6.2 Design and Production Methodology for Composite B-Pillar

### 6.2.1 Development of Design Methodology

The primary goal of this phase of the project was to establish the design and analysis protocol for a B-pillar using lightweight composite materials. A study of commercial tools for establishing this methodology was carried out that with CATIA chosen as the CAD-CAE design tool; Altair's HyperWorks as a FE pre- post- processing tool and LSTC LS-DYNA as the crash analysis solver. CATIA was chosen as the CAD interface as this software had unique capabilities for virtual design and manufacturing of multi-layer composites with data export directly to third party FE solvers and various laser projection/ply cutters. HyperMesh 13.0 was used as the FE preprocessor to use the powerful surface meshing capabilities and recently added drape functionality with ply and laminate realization. These features allowed for direct composite property mapping that could be exported to various solver environments (Figure 6-4).

Currently the DYNA \*.key export feature in HyperMesh does not include composite property information mapped onto shell elements so a software conversion utility was written in NI LabVIEW that converted NASTRAN \*.bdf files that contained this information into an LS-DYNA \*.key format. This allowed simulation of as-draped composite information within LS-DYNA with the option to easily update composite definition within CATIA and remap to the FE mesh within HyperMesh for laminate optimization. This workflow is shown schematically in Figure 6-4.

Additionally, this project required materials characterization and sharing of various material property to be used among the various design and engineering group members. Demonstration of assembly and management of this data was seen as critical to the success of this project. To aid in this effort, SMARTree, a material data management software application, was used to populate and share material data from various sources. SMARTree co-developed at UD-CCM was an easy-to-use, drag-and-drop client that allowed implementation and control of standard protocols to store and share material, process and test data. The drag-and-build SMARTree environment, shown in Figure 6-5 includes built-in logic and integrity checks so as to ensure valid data with compliance to various material and test standards. The software also has embedded modeling capabilities that include micromechanics, property calculations as

well as linear and non-linear laminate analysis. The data can be exported directly to various FE solvers for analysis and design.

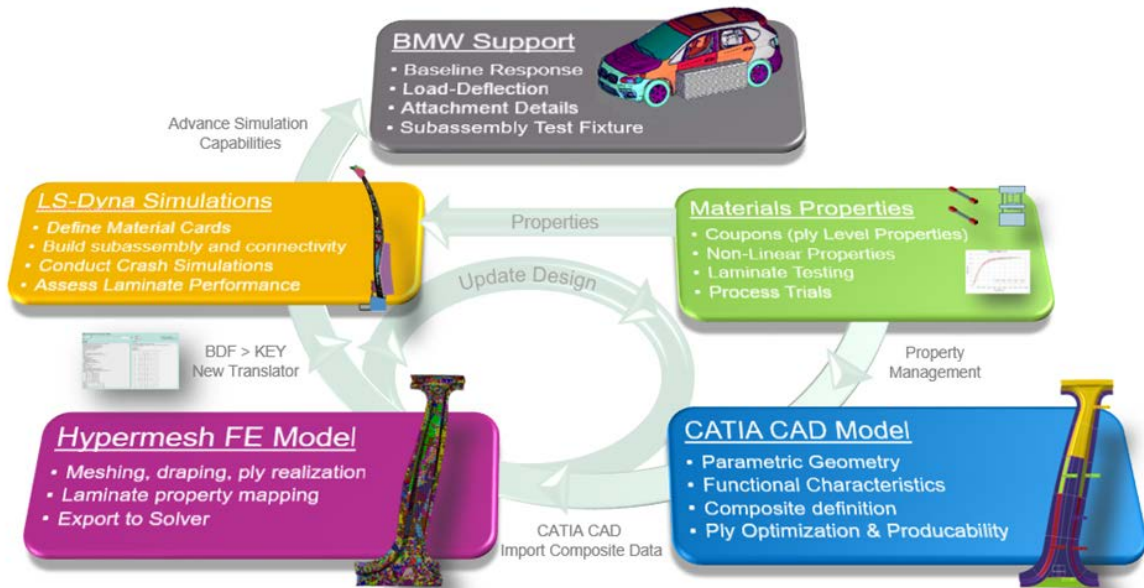


Figure 6-4. Design Framework and Workflow

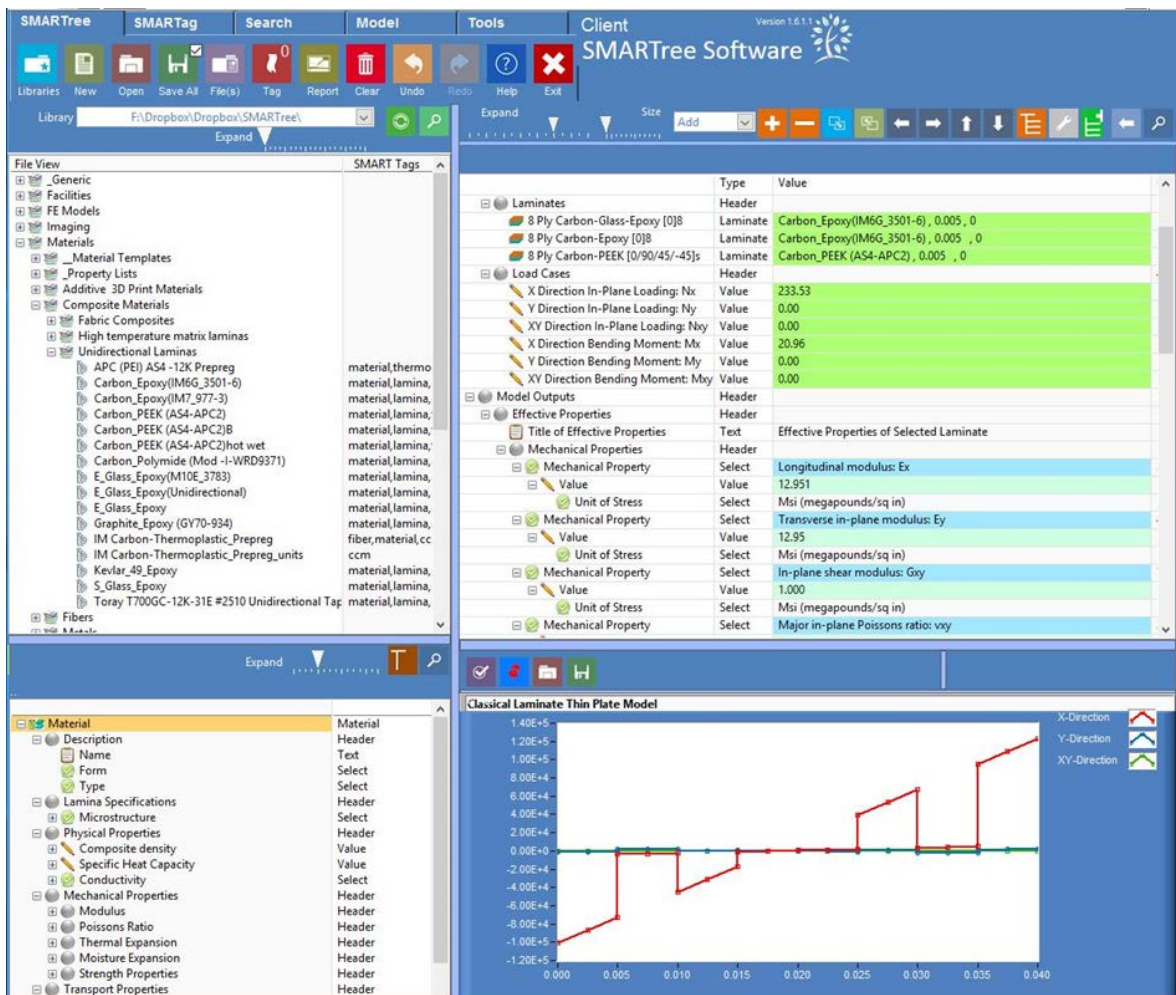


Figure 6-5. SMARTree Client Used to Capture, Store and Share Material Property Data

SMARTree was used to generate a number of thermoplastic material property datasets including non-linear mechanical properties. This data was generated from raw test data that was reduced using a Levenberg-Marquardt algorithm embedded within the software that directly calculates a set of coefficients of the Ramberg-Osgood non-linear model. This data was used to evaluate laminate behavior using the embedded non-linear analytical model. A schematic of this workflow is shown in Figure 6-6.

## 6.2.2 CATIA Composite Model Definition

CATIA composites engineering design and composite design for manufacturing provided process-oriented tools dedicated to the design of composites parts from preliminary to engineering detailed design to direct generation of manufacturing data. CPE targets aerospace, automotive, consumer goods and shipbuilding industries OEMs and suppliers. Automatic ply generation, exact solid generation, analysis tools such as fiber draping simulation and inspection capabilities are just some of the essential components of this product. By enabling users to embed manufacturing constraints earlier in the conceptual design stage, this product shortens the design-to-manufacturing period. With the powerful synchronization capabilities, CPM is the essential link between engineering design and physical manufacturing, allowing suppliers to closely collaborate with their OEMs in the composite design process. With CPM, manufacturing engineers can include all manufacturing and producibility constraints in the composites design process. CPE offers three methods for composite definition that vary in function and complexity and robustness:

- **Ply-Based Method:** Each ply is manually defined individually using either a common orientation rosette and ply boundary or unique rosette and boundary. This method is commonly used for simple beams and stiffeners and is the most straightforward method for building a composite on a CAD surface.

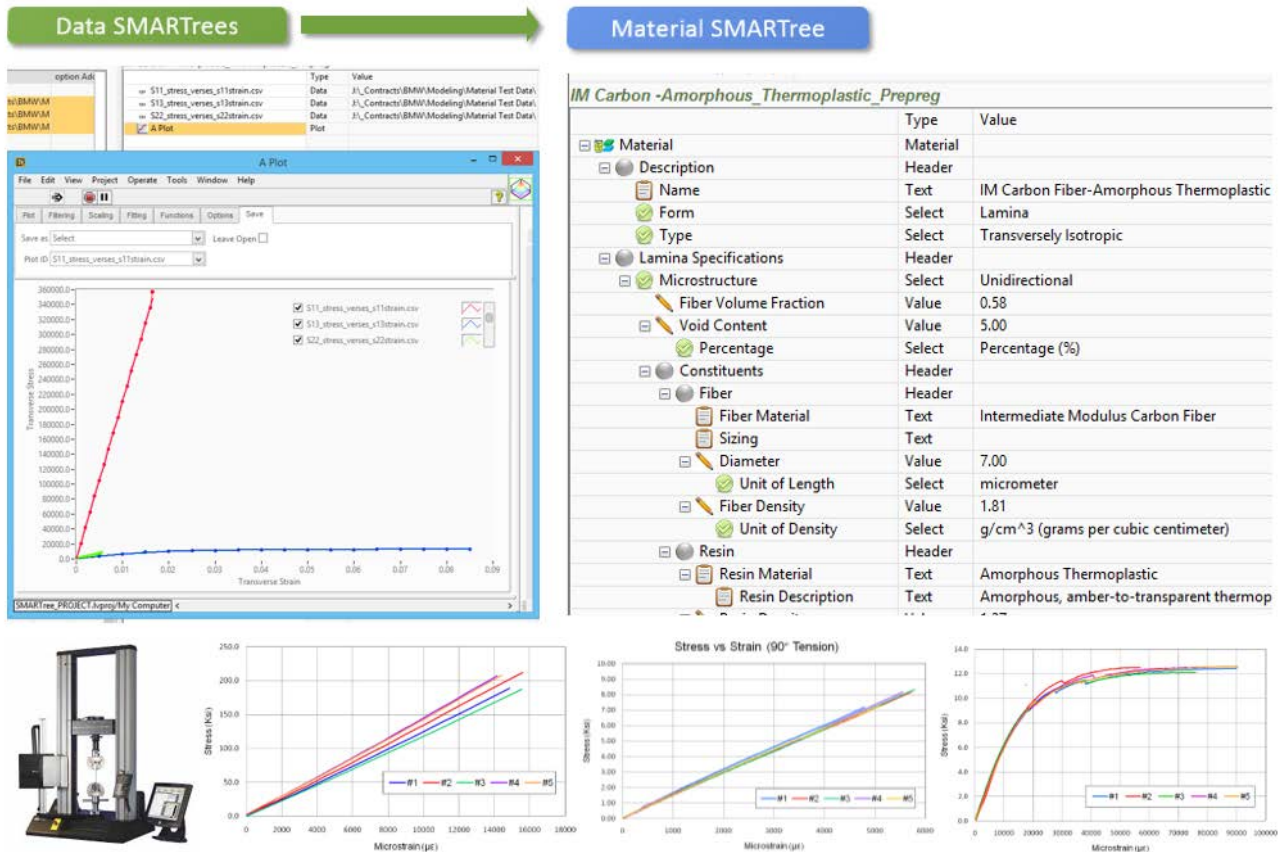


Figure 6-6. Thermoplastic Material Database Workflow Within SMARTree Client

- **Zone-Based Method:** Used for more complex structures with grouping of laminates. This method is commonly used for vehicle hoods, fenders, etc.
- **Grid-Based Method:** Complex structures requiring multi-level ply and region design/optimization. This method is commonly used for wind turbine blades, aircraft wings, fuselage, and large vehicle components.

For this effort, all composite components were defined using the grid-based method to capture and transition the discrete functionality within various regions within the structure. The following section describes the methodology used to define a composite structure on a B-pillar surface with this method.

### 1. Create Grid

Divide surface into grid boundaries where unique laminates are defined. This method does not allow modeling of surfaces with holes so these surfaces must be defined with the other methods or removed (deactivated) from the surface prior to grid definition. Surfaces with holes can be treated separately with zones or manual plies as needed and spliced into a grid with matching laminate definition. The grid is typically defined as a rectangular domain with rectilinear domains (four sides) to ensure later convergence of composite laminate cells. The edges of the composite boundary are also defined with this step. During this process, transition rules are defined between grid locations, namely the ratio or spacing by which ply-drops or adds are established. The user has a wide variety of options to customize the transition zones between all grid blocks. Finally, the grid does not need to reflect the ultimate laminate boundary but it should capture the user design intent. The grid defined for the hat section of



the B-pillar is shown in Figure 6-7 where a horizontal grid (purple) intercepts a vertical (blue) grid.

## 2. Define Laminate Cells

This step is used to define the laminate for each cell and merge cells as needed. The plies can be assigned by simple ply counts: ordered (stacking defined) or thickness law (ply count and orientation). Various rules regarding recommended ply ratios are established in this step. The laminate definition for the B-pillar in this project is shown in Figure 6-7.

## 3. Virtual Stacking Management

If the plies are placed in an unordered manner (ply count method) then virtual stacking management is used to organize plies within the overall structure. It establishes the user intended sequence for placement. Additional operations such as ply or cell swapping, establishing laminate symmetry and simplifying ply boundaries are carried out in this step. This step is shown schematically in Figure 6-8 for the B-pillar. Note that all plies are color coded based on composite ply definition and clicking on each cell will highlight the ply in the CAD model.

## 4. Plies Creation

This step involves setting the ply creation algorithm, parallel/offset rules and fallback strategies. The user can preview the automated ply generation result and fix/optimize as needed. Once completed these plies can be merge with adjacent regions created with other methods (plies from regions with holes etc.). Once the full ply definition is created, the manufacturing edge of part can be defined. A result of created plies is shown in Figure 6-9 where the user design intent of localized ply-drops is established.

## 5. Optimize Local Drop Offs

This optional step is used to manually adjust created ply transitions to ensure ply-drop guidelines are maintained.

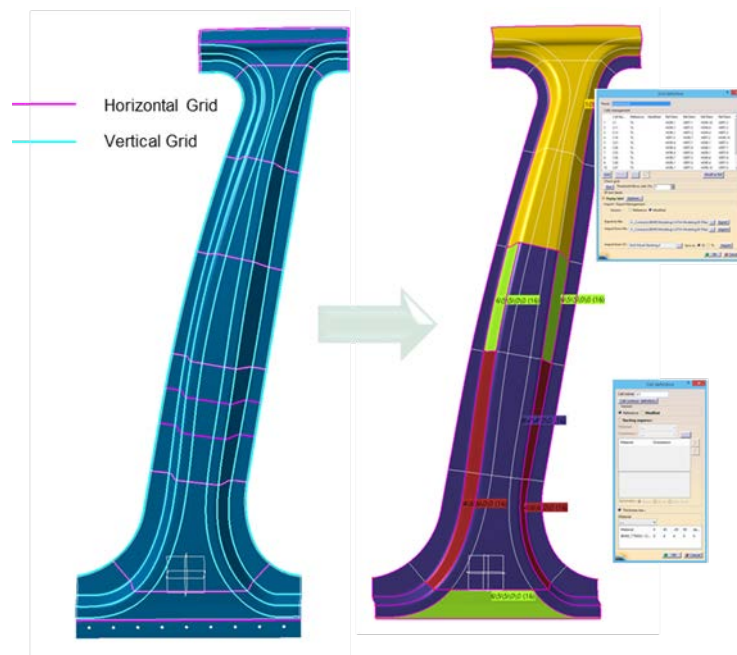


Figure 6-7. Creation of Grid and Laminate Cells

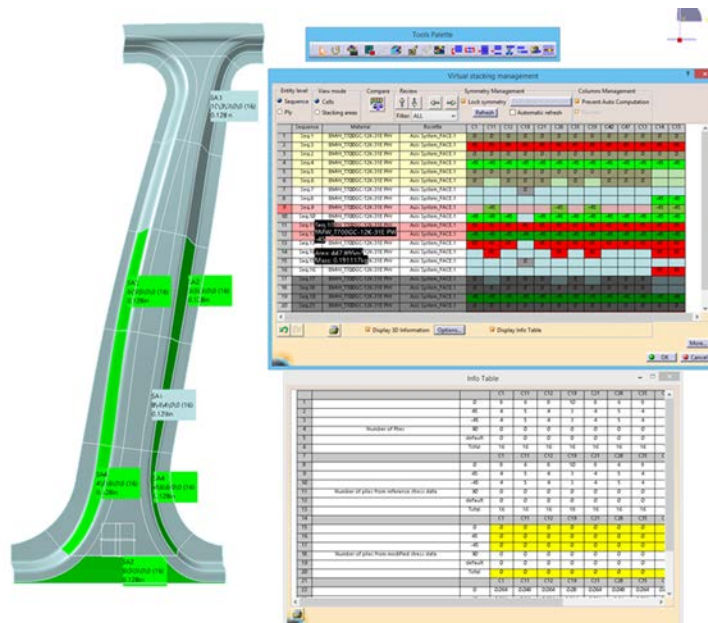


Figure 6-8. Virtual Stacking Management

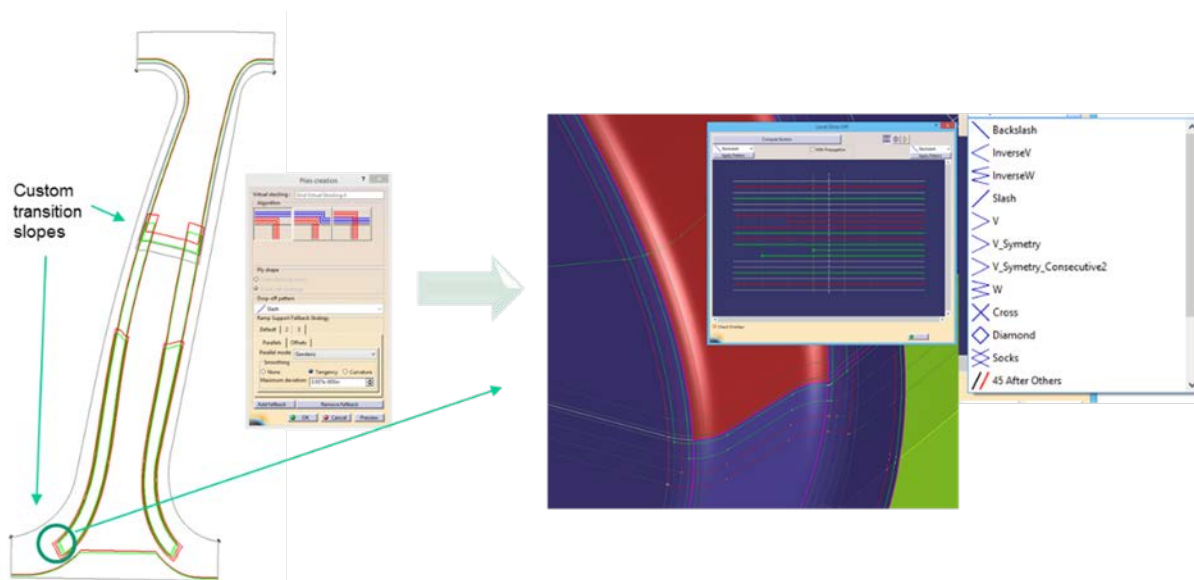


Figure 6-9. Creation of Plies Based on Grid Definition With Option to Manually Adjust Transition Regions

Once the ply stacking is created, the user can conduct a producibility analysis to observe how each ply drapes on the B-pillar surface and make adjustments as needed to minimize/control shear. Flat patterns for each ply can also be created within CPM and export as \*.dxf format for nesting and ply cutting. An add-on called Simulayt can be used to export the ply draped orientation for direct import into Dassault Systems ABAQUS or ANSYS workbench software. In this effort Altair's embedded draped ply simulator is used to map ply properties to an FE mesh so it is only necessary to export composite ply definition with the associated CAD surfaces to conduct an analysis on the structure. Figure 6-10 shows the B-pillar flat pattern for a full coverage ply as well as a number of localized plies. Fixed geometric points can also be

mapped on to a generated flat pattern function and is useful for overlaying patterns for thermoplastic blank production prior to the thermoforming operation.

### 6.2.3 CATIA to LS-DYNA Using Altair HyperMesh

Building an LS-DYNA model with complex surfaces and associated composite laminate definition is time consuming and typically limited to projected (ideal) ply definitions and simple shapes (planer, radial etc.). Evaluation and optimization of design concepts and laminates using this manually intensive method was not practical for this project. Additionally, projected ply definition does not accurately capture draped or thermoformed ply orientations. This effort used a semi-automated methodology that was built using both existing tools and new translation methods to evaluate various design concepts under dynamic progressive failure loading. With the composite defined in a CATIA CATPart file, Altair's HyperMesh was used as the preprocessor to import this data, map to a FE mesh created within this environment and exported as a NASTRAN BDF file. When this process was initially carried out, the base geometry was cleaned up to aid in smooth mesh generation with congruent alignment as needed. A drape estimator was carried out for each ply with the result then applied to a laminate definition that was also imported from CATIA. Finally, the laminate was realized in the FE mesh with an accurate estimate of ply angle from draping mapped onto all elements. Once complete, this data could be exported as a solver input deck for subsequent analysis. Figure 6-11 shows the CAD to DYNA workflow through Altair HyperMesh.

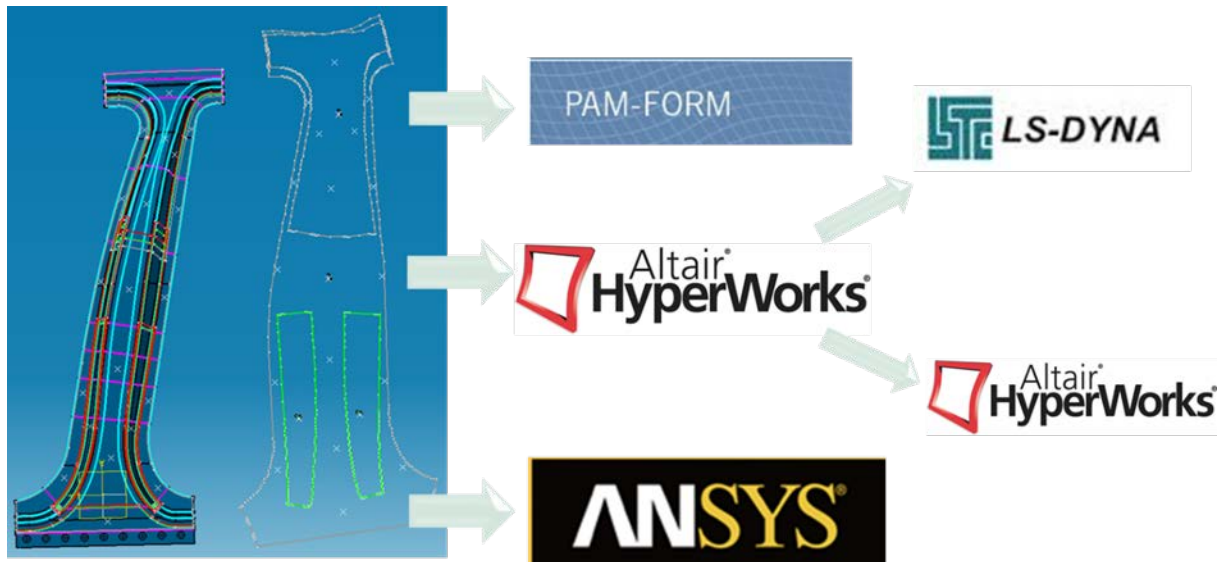


Figure 6-10. Composite Definition Exportable to Commercial Solvers



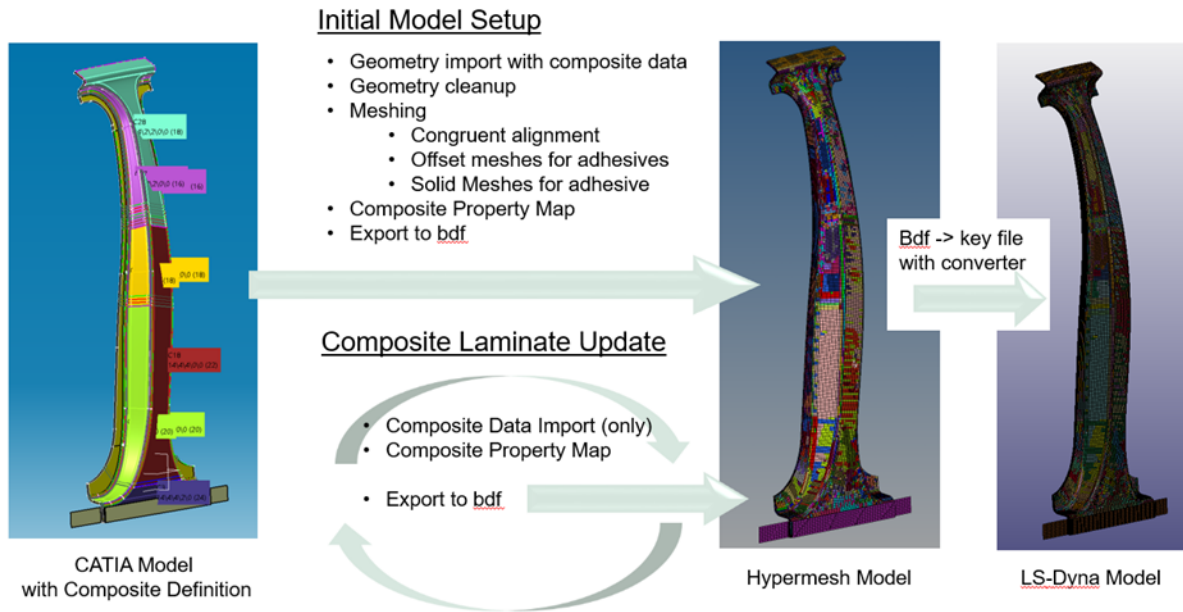


Figure 6-11. CAD to DYNA Workflow through Altair HyperMesh

## 6.2.4 NASTRAN BDF to DYNA Keyfile Translator

At the time of this project, HyperMesh did not export the required composite shell property data in \*.key format necessary for LS-DYNA. However, the NASTRAN \*.bdf format does contain this data when exported. To bridge this gap, a translator application written with NI LabVIEW and called bdf2key Converter was created, that reads \*.bdf files and converts the data to LS-DYNA \*.key format. To capture all information necessary for complete model generation the following BDF keywords were read and converted into their equivalent \*.key keywords.

- GRID to \*NODE coordinates
- CQUAD4 and CTRIA3 to \*ELEMENT\_SHELL
- PCOMPG to \*PART\_COMPOSITE
- Solid CHEXA and CPENTA to \*ELEMENT\_SOLID
- Node SET list to \*SET\_NODE\_LIST\_GENERATE
- Element SET list to \*SET\_ELEMENT\_LIST\_GENERATE

The solid (CHEXA) translation from NASTRAN BDF to LS-DYNA key format is added to include and solid adhesive region created and meshed in HyperMesh. The HyperMesh SET list to \*SET\_NODE\_LIST\_GENERATE and \*SET\_ELEMENT\_LIST\_GENERATE in LS-DYNA converters were added to facilitate the creation of the cohesive zone between both laminates necessary for multiple laminate assemblies. In addition to these conversion functions a number of additional features were added to the software that included: Replace or overwrite default ply thicknesses for each ply material, isolate changes to specific materials, translate geometry to ideal assembly location and overwrite material IDs for various composite material cards within LS-DYNA. Figure 6-12 shows a schematic of this standalone software application. It is planned to incorporate this converter utility within the next release of SMARTree so that material property inputs are transferred directly to the \*.key input file to ensure data connectivity between model and source measured properties.

## 6.2.5 Baseline Composite Model in CATIA

A parametric CAD model of a simple B-pillar was developed using a generic design provided by BMW. This model helped to establish the design space or envelope available for composite design and optimization using ABAQUS and LS-DYNA. The model, shown in Figure 6-13, uses approximately 60 geometric values to establish part geometry and that are ranked as either fixed (vehicle envelope) or variable geometry available for design and optimization. The geometric envelope for this design is based on a generic vehicle model provided by BMW with

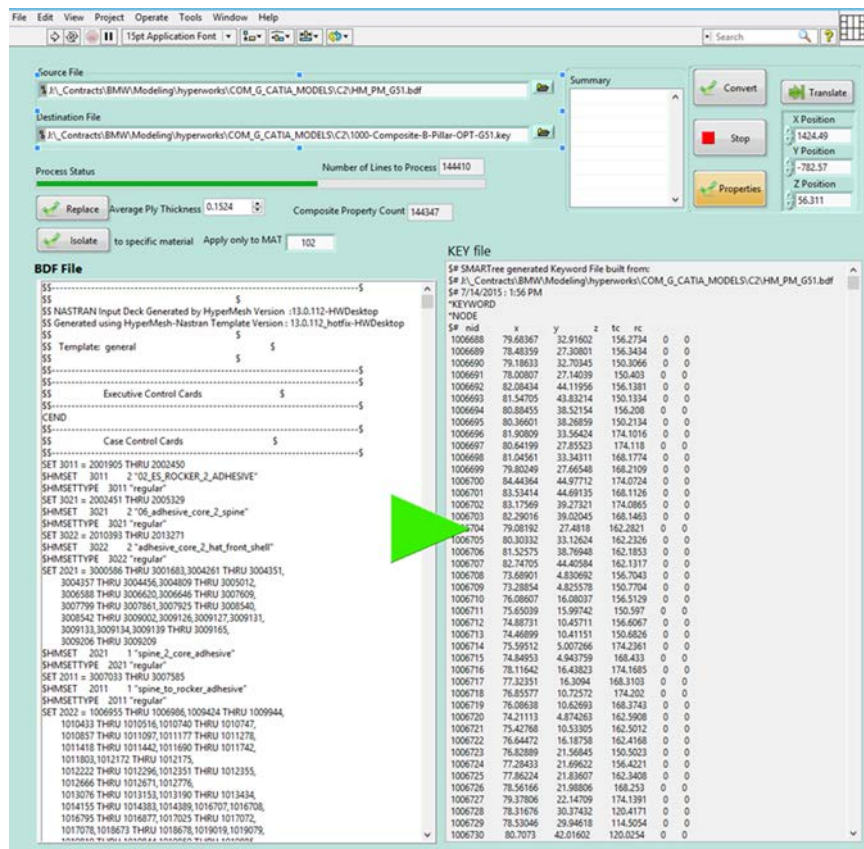


Figure 6-12. LS-DYNA Keyfile Generator

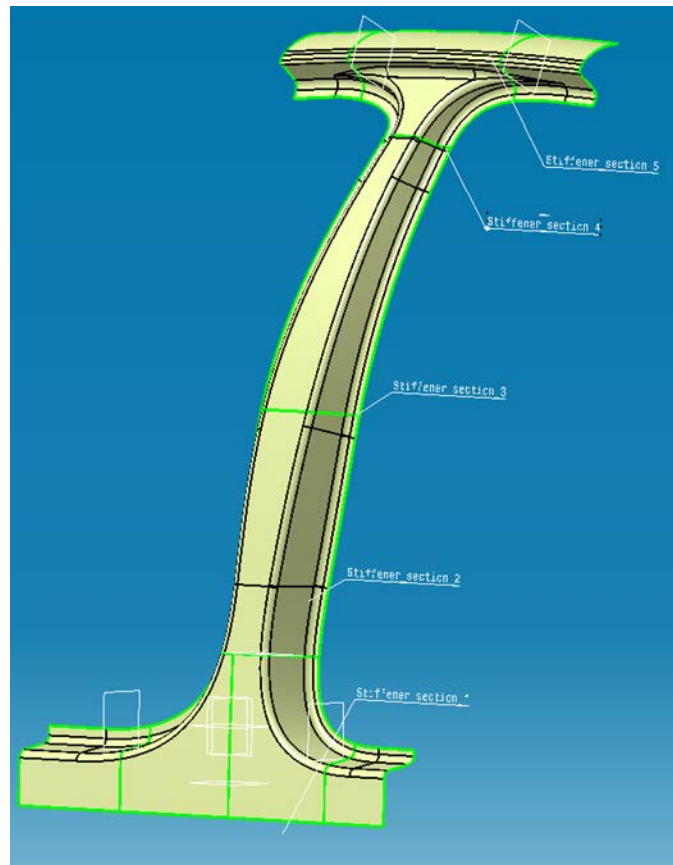


Figure 6-13. Initial Parametric CAD Surface Model

removal of some surface detail so as to simplify composite surface definition. This geometric model was used as the initial surface used for composite definition and export into HyperMesh and ultimately LS-DYNA for crash impact modeling.

### 6.2.6 Composite B-Pillar Design Studies

A wide variety of shapes and associated composite designs were evaluated. The first design considered an open hat section that was found to split and fail irrespective of laminate thickness as shown in Figure 6-14a. This led to the development of a two-part closed hat section with a smooth taper as shown in Figure 6-14b. However significant shear loading at the rocker region resulted in tension-shear failure at the base of the composite. The lack of hat section material available for progressive crushing near the rocker during loading led to the development of a two-part design that ultimately survived crash impact.

The two-part design considered two composite parts with a smooth “spine” laminate bonded to a “hat” laminate as shown in Figure 6-15. For the spine laminate, different materials that included high-strength AS4/PEI as well as infused AS4/Elium thermoplastic were considered. The hat structure comprised an optimized AS4/Nylon laminate configuration with an optimized layup with discrete functionality during a crash event. The spine was designed to survive the impact event without catastrophic failure while the high-elongation nylon-based hat structure absorbed the majority of the impact energy through deformation and crushing. The adhesive was modeled as a solid cohesive layer bonded to both structures using shell segments elements. Node and element SET definitions created in HyperMesh and converted using bdf2key aided in creation of the fastened connection property in LS-DYNA.

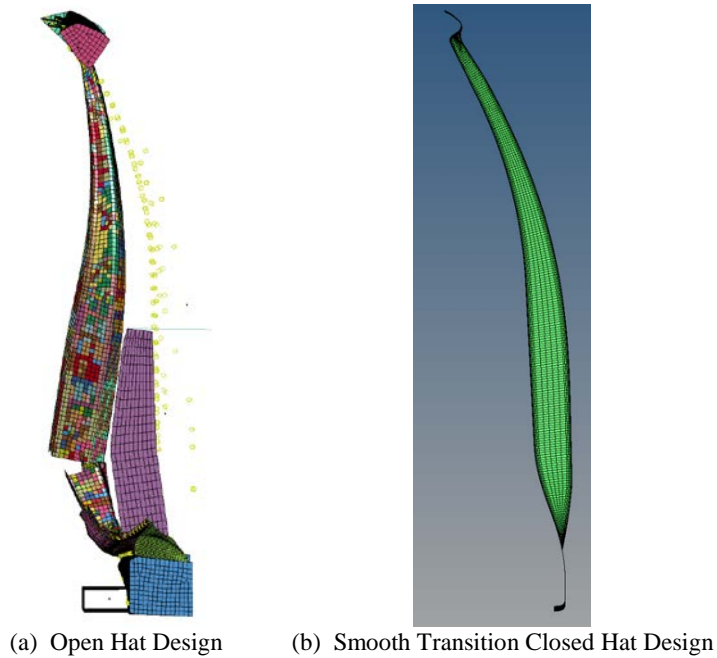


Figure 6-14. Design Iterations for Composite B-Pillar

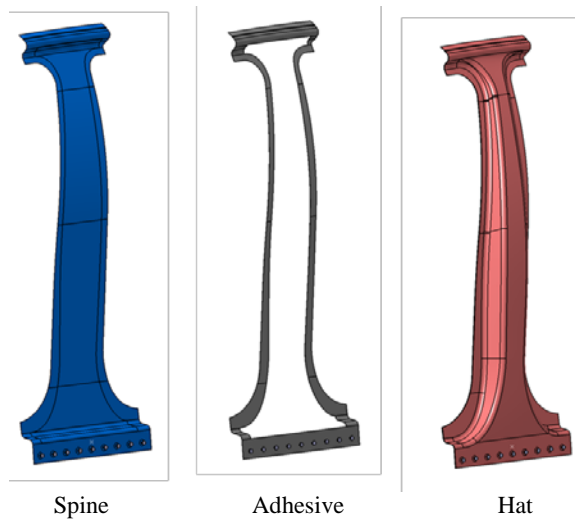


Figure 6-15. Spine-Hat Composite B-Pillar Adhesively Bonded Over Entire Boundary

The B-pillar hat structure was specifically designed to absorb as much energy as possible through progressive crushing of the sidewalls highlighted in green in Figure 6-16. To achieve this crushing effect, off-axis dominant laminates were prescribed in these sidewalls within CATIA using the Grid Method. The face of the hat structure included additional zero-degree plies to increase structural bending stiffness and increase axial load bearing capability during the crash event.

To reduce overall weight, the laminate thickness drops in the vertical axial direction as less material was needed in the less-loaded hat upper section. Transition regions were automatically built between these regions using rules and ply transitions defined with the Grid Method in CATIA. All property definitions were mapped to the FE mesh with adequate mesh densities at transition regions.

Figure 6-17a shows the FE model in HyperMesh with the ply boundaries shown in grey. Figure 6-17b shows the individual shells at the rocker location with three adhesive layers sandwiching four shell regions; rocker, spine and hat laminate and a metallic faceplate. This finalized and realistic two-part bonded design was optimized for laminate definition at the hat and spine for minimal weight while meeting crash peak deformation limit requirements.

Some design studies also considered a row of fasteners added to the model using point connections with inputs for elastic-plastic (failure) response of measured fasteners. A number of design iterations were carried out with this design configuration that resulted in a composite structure weight 5.13 kg, compared to the 8.98 kg metallic baseline.

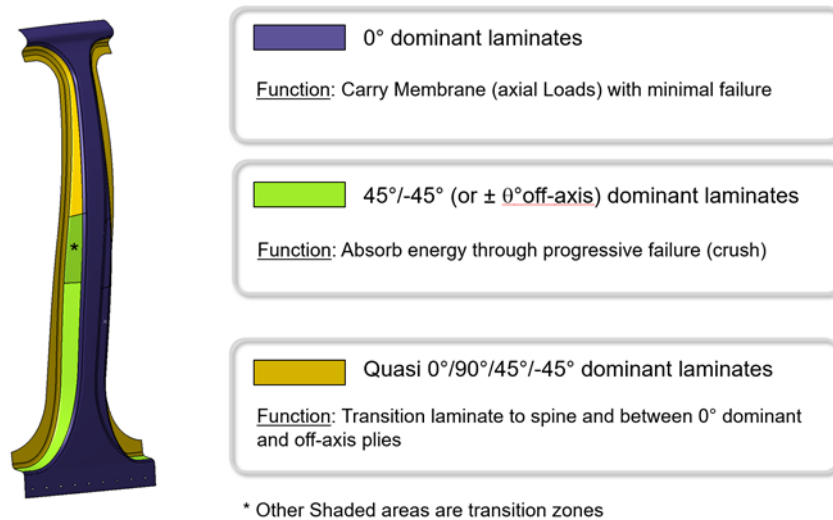


Figure 6-16. Hat Composite Designed With Discrete Functionality

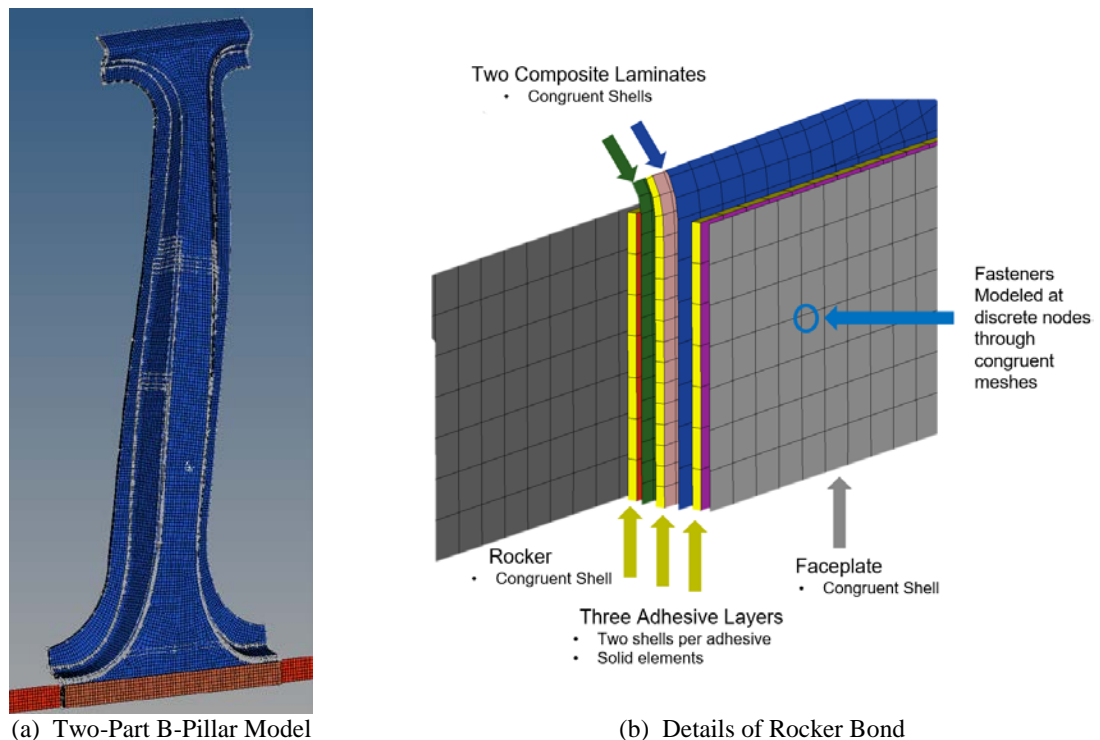
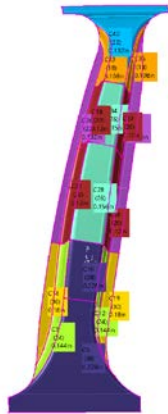


Figure 6-17. Two-Part Spine-Hat Bonded B-Pillar Design



Figure 6-18a shows the resulting laminate grid model of hat in CATIA and the layout for each grid region in Figure 6-18b. Note that this table presents half the laminate for each grid cell as each cell unit is symmetric. For example, region SA1 is comprised of 38 plies while region SA3 has 30 plies. Figure 6-19a shows how the AS4/PEI laminate spine design is configured with maximum thickness at the rocker location and Figure 6-19b shows the stacking configuration table. Because the number of layers in different grid region is different, thickness of the hat or spine structure is also different that is graphically shown in Figure 6-20a. Because of ply-drops in different grid regions, the ply layout calculated by CATIA shows necessary overlaps for smooth transition in thickness (Figure 6-20b). During production, these overlaps were fabricated as close to the CATIA specifications within the manufacturing constraints.

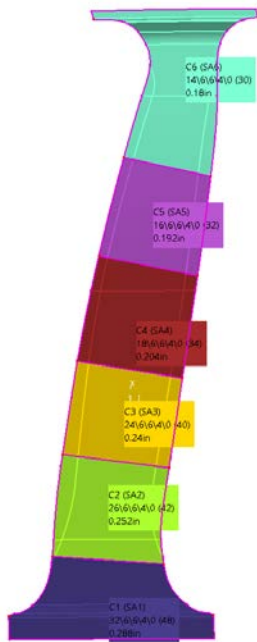


(a) AS4/Nylon Hat Composite Design

Sequence	Material	Rosette	SA1	SA3	SA6	SA2	SA5	SA8	SA4	SA7
1	Seq.1	AS4_NYLON_Prepreg	Axis System_FACE.1	45	45	45	45	45	45	45
2	Seq.4	AS4_NYLON_Prepreg	Axis System_FACE.1	-45	-45	-45	-45	-45	-45	-45
3	Seq.18	AS4_NYLON_Prepreg	Axis System_FACE.1	90	90	90				
4	Seq.7	AS4_NYLON_Prepreg	Axis System_FACE.1	0	0	0	0	0	0	0
5	Seq.2	AS4_NYLON_Prepreg	Axis System_FACE.1	45	45	45	45	45	45	45
6	Seq.5	AS4_NYLON_Prepreg	Axis System_FACE.1	-45	-45	-45	-45	-45	-45	-45
7	Seq.8	AS4_NYLON_Prepreg	Axis System_FACE.1	0	0	0	0	0	0	0
8	Seq.3	AS4_NYLON_Prepreg	Axis System_FACE.1	45	45	45	45	45	45	45
9	Seq.6	AS4_NYLON_Prepreg	Axis System_FACE.1	-45	-45	-45	-45	-45	-45	-45
10	Seq.11	AS4_NYLON_Prepreg	Axis System_FACE.1	0	0	0	0	0	0	0
11	Seq.9	AS4_NYLON_Prepreg	Axis System_FACE.1	-45	-45		-45	-45		-45
12	Seq.10	AS4_NYLON_Prepreg	Axis System_FACE.1	45	45		45	45		45
13	Seq.16	AS4_NYLON_Prepreg	Axis System_FACE.1	0		0			0	
14	Seq.15	AS4_NYLON_Prepreg	Axis System_FACE.1	45	45		45			
15	Seq.13	AS4_NYLON_Prepreg	Axis System_FACE.1	-45	-45		-45			
16	Seq.17	AS4_NYLON_Prepreg	Axis System_FACE.1	0		0			0	
17	Seq.12	AS4_NYLON_Prepreg	Axis System_FACE.1	-45	-45		-45			
18	Seq.14	AS4_NYLON_Prepreg	Axis System_FACE.1	45	45		45			
19	Seq.19	AS4_NYLON_Prepreg	Axis System_FACE.1	0		0				

(b) Stacking Configuration Table

Figure 6-18. AS4/Nylon Hat Composite Design and Stacking Configuration



(a) AS4/Nylon Spine Composite Design

Sequence	Material	Rosette	SA1	SA2	SA3	SA4	SA5	SA6
1	Seq.8	AS4_PEI_Prepreg	Axis System_BACK.1	45	45	45	45	45
2	Seq.11	AS4_PEI_Prepreg	Axis System_BACK.1	-45	-45	-45	-45	-45
3	Seq.14	AS4_PEI_Prepreg	Axis System_BACK.1	90	90	90	90	90
4	Seq.1	AS4_PEI_Prepreg	Axis System_BACK.1	0	0	0	0	0
5	Seq.4	AS4_PEI_Prepreg	Axis System_BACK.1	0	0	0	0	0
6	Seq.5	AS4_PEI_Prepreg	Axis System_BACK.1	0	0	0	0	0
7	Seq.2	AS4_PEI_Prepreg	Axis System_BACK.1	0	0	0	0	0
8	Seq.15	AS4_PEI_Prepreg	Axis System_BACK.1	90	90	90	90	90
9	Seq.9	AS4_PEI_Prepreg	Axis System_BACK.1	45	45	45	45	45
10	Seq.12	AS4_PEI_Prepreg	Axis System_BACK.1	-45	-45	-45	-45	-45
11	Seq.6	AS4_PEI_Prepreg	Axis System_BACK.1	0	0	0	0	0
12	Seq.7	AS4_PEI_Prepreg	Axis System_BACK.1	0	0	0	0	0
13	Seq.3	AS4_PEI_Prepreg	Axis System_BACK.1	0	0	0	0	0
14	Seq.13	AS4_PEI_Prepreg	Axis System_BACK.1	-45	-45	-45	-45	-45
15	Seq.10	AS4_PEI_Prepreg	Axis System_BACK.1	45	45	45	45	45
16	Seq.16	AS4_PEI_Prepreg	Axis System_BACK.1	0	0	0	0	0
17	Seq.17	AS4_PEI_Prepreg	Axis System_BACK.1	0	0	0	0	0
18	Seq.18	AS4_PEI_Prepreg	Axis System_BACK.1	0	0	0	0	0
19	Seq.19	AS4_PEI_Prepreg	Axis System_BACK.1	0	0	0	0	0
20	Seq.20	AS4_PEI_Prepreg	Axis System_BACK.1	0	0	0	0	0
21	Seq.21	AS4_PEI_Prepreg	Axis System_BACK.1	0	0	0	0	0
22	Seq.22	AS4_PEI_Prepreg	Axis System_BACK.1	0	0	0	0	0
23	Seq.23	AS4_PEI_Prepreg	Axis System_BACK.1	0	0	0	0	0
24	Seq.24	AS4_PEI_Prepreg	Axis System_BACK.1	0	0	0	0	0

(b) Stacking Configuration Table

Figure 6-19. AS4/Nylon Spine Composite Design and Stacking Configuration

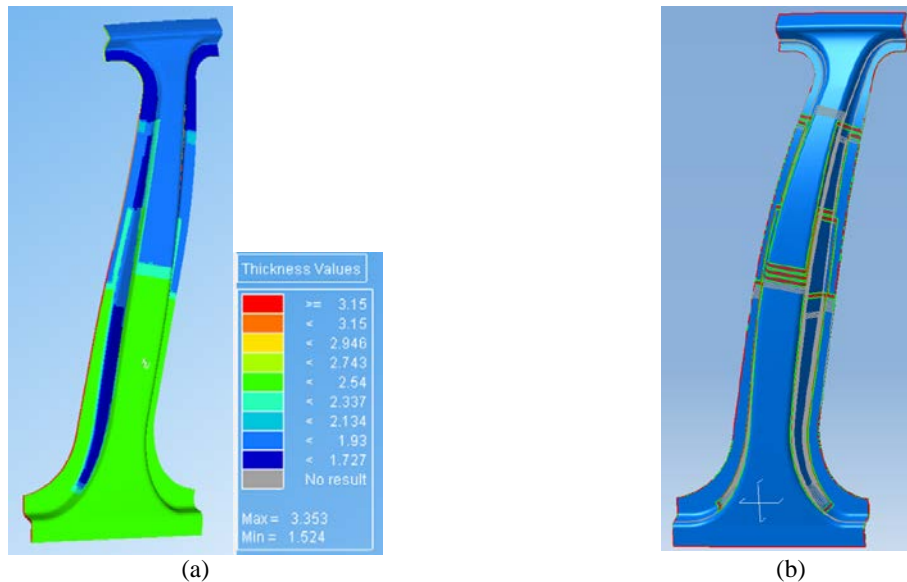


Figure 6-20. Thickness Maps of (a) B-Pillar and (b) Associated Ply Layout

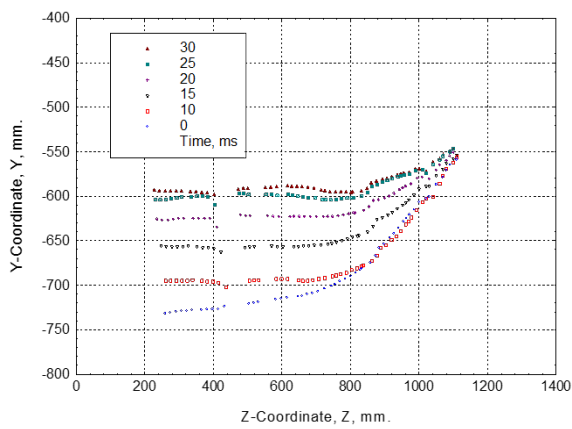
## 6.2.7 Analysis of Composite B-Pillar Design G50 and G51

The composite design procedure described in the previous section was used in developing the first-generation two-part (hat and spine) bonded composite B-pillar designated by G50. G50 composite B-pillar is designed with AS4/Nylon composite material properties for both the hat and the spine (described in Section 5) with a total weight of 7.26 kg as compared to the 9 kg metal baseline. Figure 6-21 shows the deformation profile of the G50 composite B-pillar at different time where the spine remained intact after the crash event. Crash simulation results of G50 composite-B-pillar were compared with the metal baseline results (presented in Figure 6-3) to evaluate the performance of the G50 composite B-pillar design. Figure 6-22 shows the deformation profile of the metal baseline and the G50 composite B-pillar at different times. The difference between the deformation profile at any time with the same at time zero is a measure of intrusion. Figure 6-22 shows the G50 intrusion at  $t = 10$  ms at Z-coordinate  $Z=400$  mm was equivalent while the intrusion at  $t = 30$  ms was less than the metal baseline. Time history of impactor Rigid Body Velocity (RBV, a measure showing how the impactor is slowing down transferring its momentum to the B-pillar assembly) and impact-contact force is presented in Figure 6-23a & b. G50 composite design showed higher initial crash force and higher average crash force (in the time range 5-15 ms) resulting in earlier drop in impactor velocity and overall lower rebound velocity (about 2 m/s). In the composite B-pillar design G51, AS4/Nylon material properties were used for the hat while AS4/PEI material properties were used for the spine. This design change further reduced the weight of the G51 composite B-pillar to 5.44 kg (40% weight reduction as compared to the baseline). The new G51 Nylon Hat PEI Spine hybrid B-pillar produced a lower average crash force similar to metal baseline while delaying the drop in velocity of the impactor yielding a better composite design. Rigid body velocity (RBV) of the impactor and the impact-contact force can also be plotted with the rigid body displacement (RBD) of the impactor to visualize the spatial reduction of impactor RBV and to calculate the work done during the crush event. Figure 6-24 shows the same in RBV versus RBD of the impactor and the Force versus impactor RBD plots. RBD of G51 design increased to 187 mm as compared to the 176 mm RBD of the G50 design, however, both were less than the RBD 196 mm of the metal baseline. The difference in RBD of the impactor and the maximum intrusion of the back face of the B-Pillar is a measure of relative crush, otherwise they are two different time dependent variables. Force versus RBD plot of G51 design closely resembled

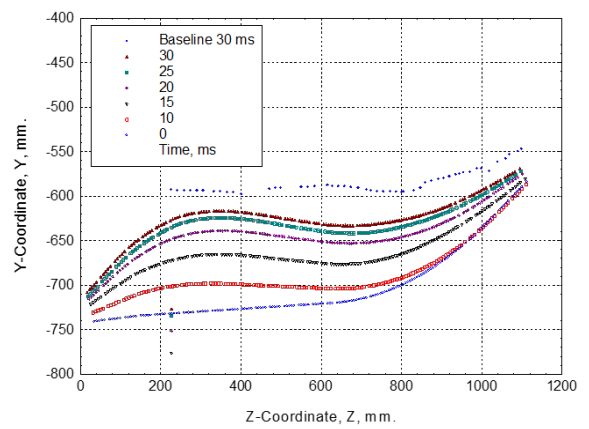
the metal baseline design revealing that the G51 was a composite design similar to the metal baseline in terms of energy dissipation yet 40 percent lighter in weight.



Figure 6-21. LS-DYNA Crash Simulation Result at Various Times  
 Composite B-pillar design G50 computational run #90 designated by "091-G50."  
 Material AS4/Nylon, Total Weight 7.26 kg as compared to Metal Baseline weight of 9 kg.



(a) Metal Baseline



(b) G50-Composite-B-Pillar

Figure 6-22. Dynamic Deformation or Intrusion at Different Times  
 G50-Composite B-Pillar, Material AS4/Nylon



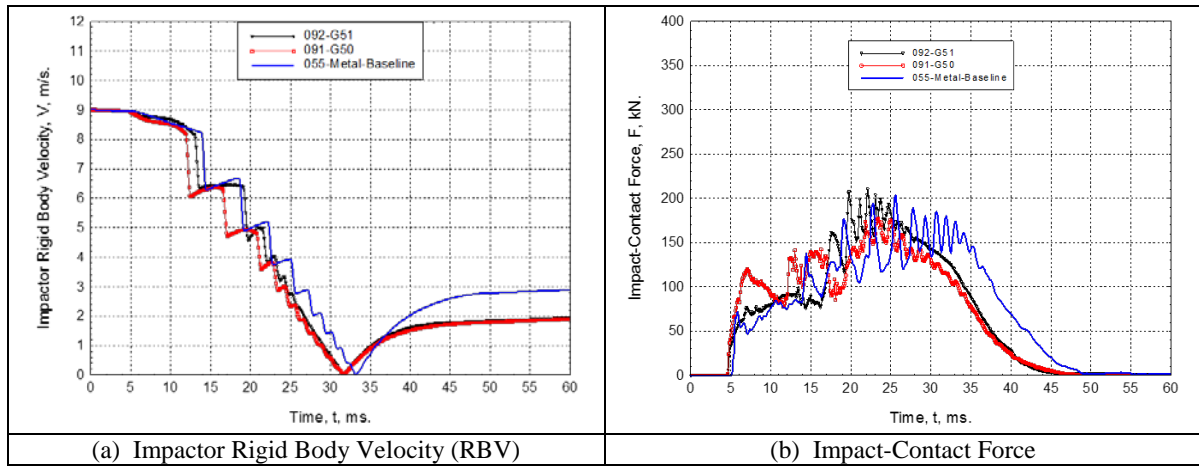


Figure 6-23. Time History of Impactor Ridge Body Velocity (RBV) and Impact-Contact Force G50-Composite B-Pillar, Material ZS4/Nylon; G51-Composite B-Pillar, Material AS4/Nylon Hat & AS4/PEI Spine

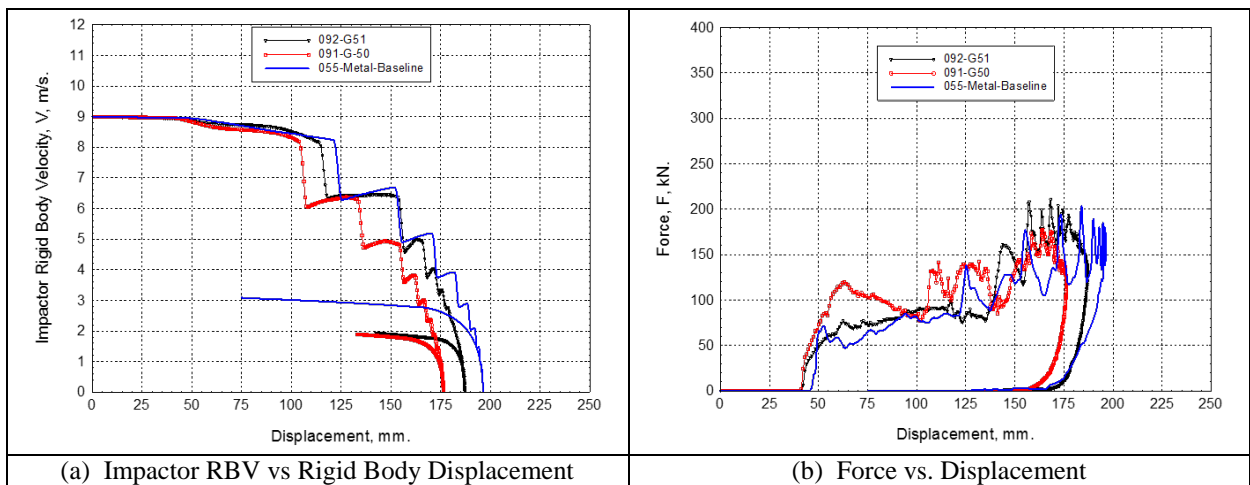


Figure 6-24. Impactor Rigid Body Velocity (RBV) and Impact-Contact Force Versus Impactor Rigid Body Displacement (RBD)G50-Composite B-Pillar, Material AS4/Nylon; G51-Composite B-Pillar, Material AS4/Nylon Hat & AS4/PEI Spine

In order to further reduce the weight of the G51 composite design, axial strain along the direction of the B-pillar centerline (strain along material direction 1, because the [0] plies are oriented approximately along the centerline of the B-pillar) of both the hat and spine were investigated (Figure 6-25). It was identified that the crush of the hat webs near the root of the B-pillar created strain concentration on the spine (Figure 6-25b). This observation led to the so-called TAB design of the B-pillar and is discussed further in the following section.

## 6.2.8 Finalized “TAB” Design of G81 TAB Composite B-Pillar

Modeling and simulations for the G51 composite B-pillar design identified localized bending strains in the spine near the root of the hat as shown in Figure 6-25. To alleviate these strains, cutouts were introduced in the hat stiffener to prevent the hat sidewalls from causing localized bending in these regions. These cutouts significantly reduced the strain concentrations and also resulted in a composite design that was lighter and more producible. This cutout feature was also introduced in the top of the B-pillar to reduce weight and also to improve the producibility at that location. This new G81 TAB composite B-pillar design is shown in Figure 6-26

showing the flat pattern for a full coverage ply. Crash simulation of the G81 TAB composite B-pillar design eliminated the local strain concentration at the root and better crushing of the hat on top of the spine (Figures 6-27 and 6-28). The crash performance of the finalized G81 TAB composite B-pillar design is compared with the metal baseline in Figure 6-29, which shows much less intrusion than the baseline, similar average crushing behavior in the time range 5-15 ms, and comparable rigid body velocity of the impactor. Weight of the finalized G81 TAB design was found to be 3.86 kg, a 57 percent weight saving as compared to the metal baseline.

A brief overview of composite B-pillar design process and corresponding weight and cost of different B-pillars are presented in Figures 6-30 and 6-31.

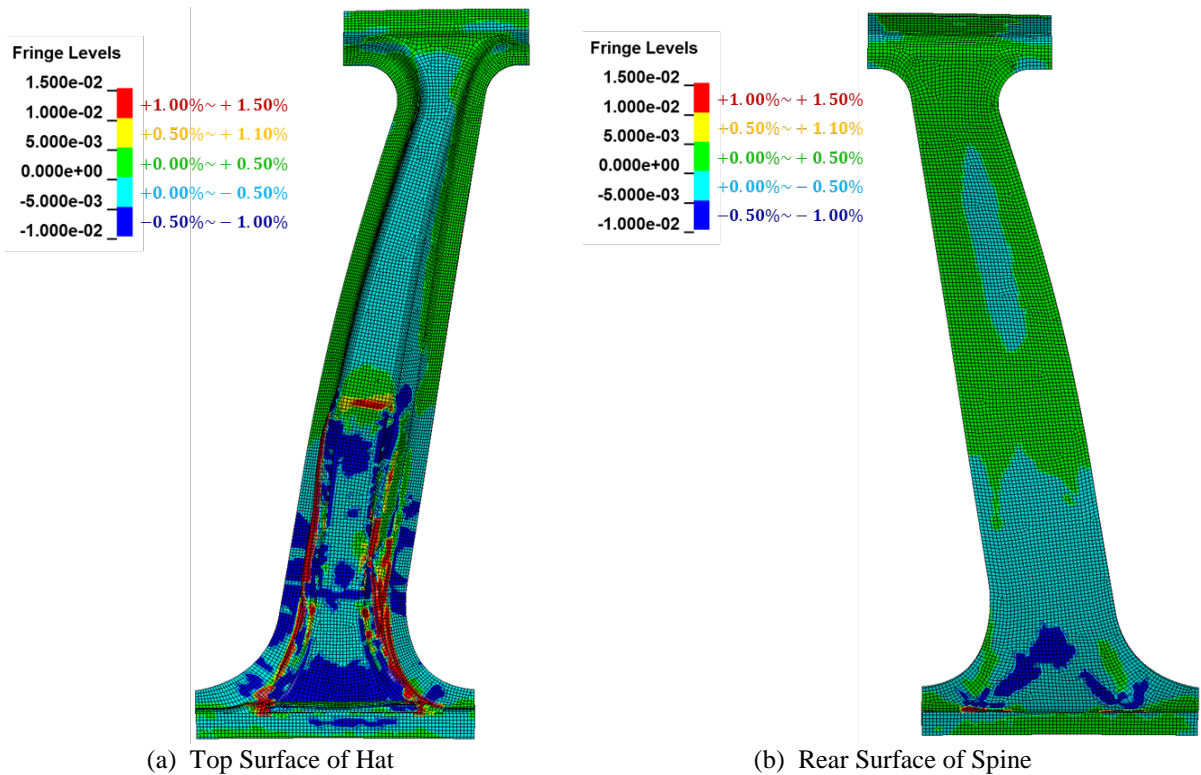


Figure 6-25. Axial Strain Distribution on G50 Hat and Spine G51-Composite B-Pillar, Material AS4/Nylon Hat & AS4/PEI Spine

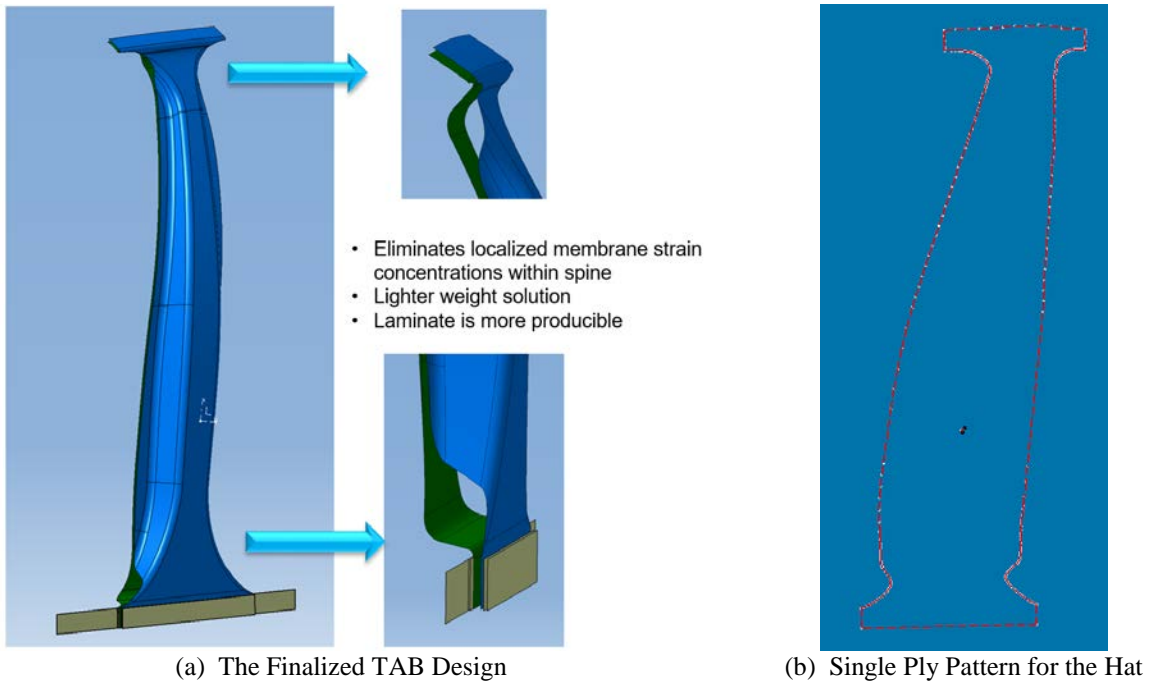


Figure 6-26. Finalized G81 TAB Composite B-Pillar Design to Reduce Strain Concentrations, to Reduce Weight, and to Increase Producibility

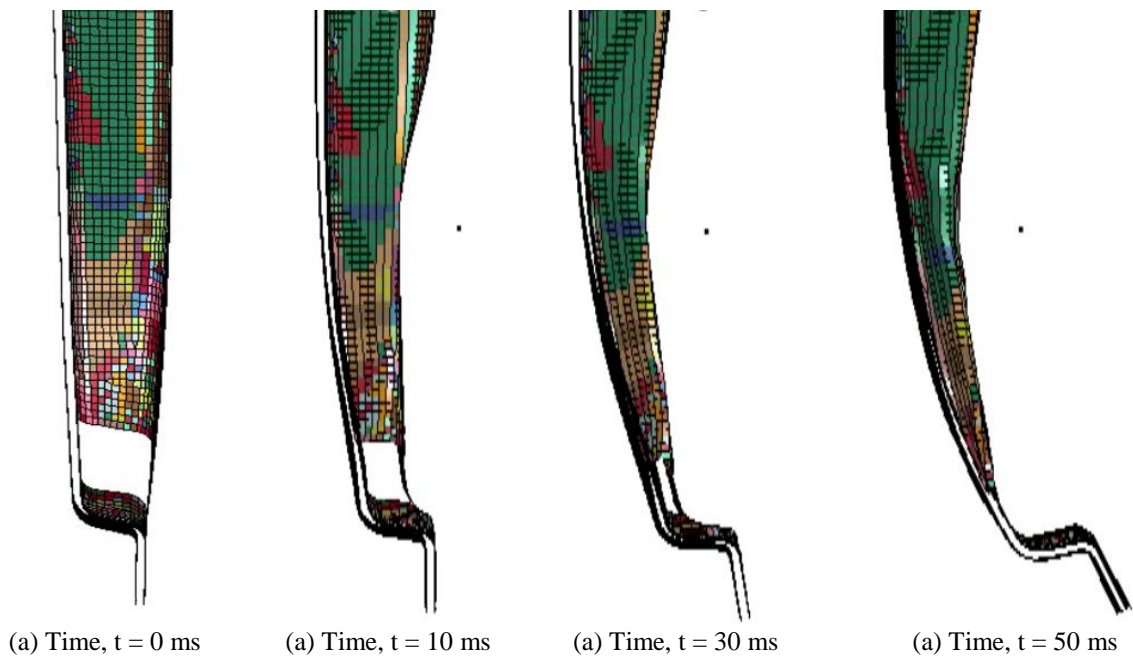


Figure 6-27. Dynamic Deformation at the Root of Finalized G81 TAB Composite B-Pillar Design  
Material AS4/Nylon Hat and AS4/PEI Spine. Total Weight 3.86 kg (57% weight reduction as compared to Metal Baseline)

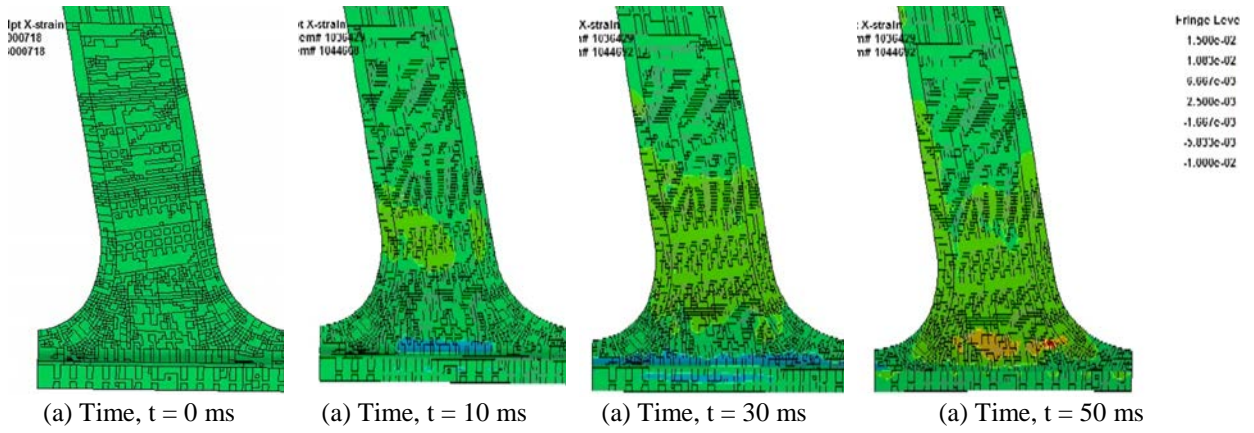


Figure 6-28. Strain Concentration of Finalized G81 TAB Composite B-Pillar Design

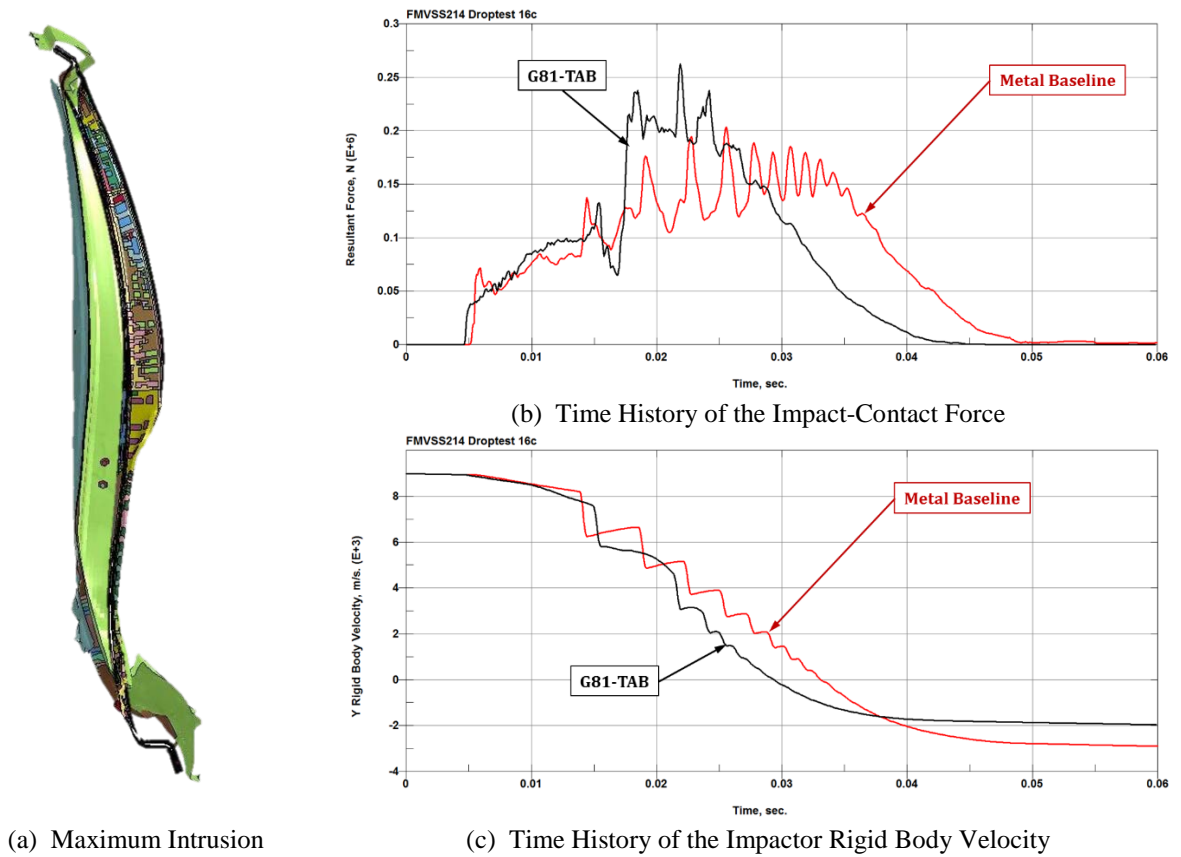


Figure 6-29. Crash Performance of Finalized G81 TAB Composite B-Pillar Design

Design Iterations	Material	Failure	Deformation Limit	Weight, lbs.	Observation
Hat Section Only	AS4/PEI	Yes	NA	6.3	Hat Spreading/buckling. Requires closed hat section
Partially Closed Section	AS4/PEI	Yes	NA	7.7	Tension Failure at the Root Requires fully closed Spine
Fully closed Hat Section smooth tapered Backing 056-32S-16H-QI*	AS4/PEI	Yes	NA	8.0	Spine Tension Failure, insufficient volume for crush
<b>Fully closed Hat Section</b>					
- 058A - 32S-16H- QI*	AS4/PEI	Yes	Exceeded	8.3	Additional Plies needed at rto prevent failure
- 059- 32S-16H-ALL-[+/-45]*	AS4/PEI	Yes	Exceeded	8.3	All 45 system too compliant
- 060-32S-QI-16H-[+/-45]	AS4/PEI	Yes	Exceeded	8.3	Additional Stiffening required for Spine
<b>Fully closed Hat Section + Adhesive</b>					
- 090-G50- Grid Design Constant Section Spine	AS4/Nylon	No	No	16	Heavy design due to low stiffness/strength, requires spine taper
- 092-G51- Grid Design Tapered Spine	AS4/PEI S AS4/Nylon H	No	No	12	Localized membrane strain concentration at root caused by hat section
TAB Design Concept	AS4/PEI S AS4/Nylon H	No	No	8.26	Localized Strains reduced

\*H = Hat, S = Spine, QI = quasi isotropic, G = Grid ply coverage

Figure 6-30. Brief Overview of Composite B-Pillar Design Process

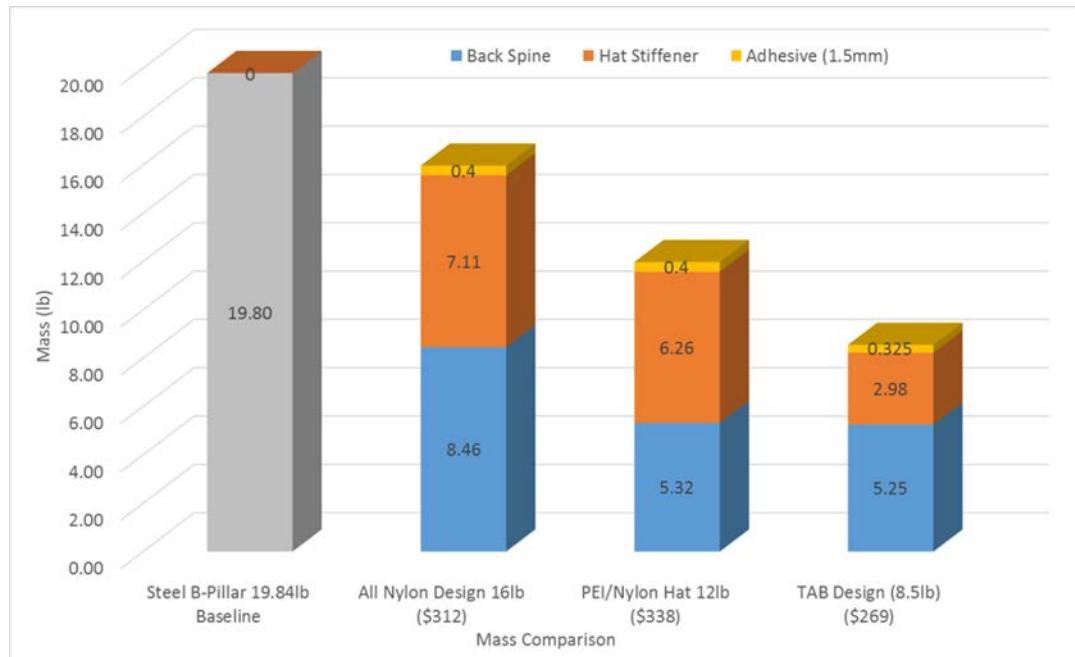


Figure 6-31. Weight and Cost of Different Composite B-Pillar Designs



## 6.3 Analysis Methodology for Composite B-Pillar

### 6.3.1 BMW Metal Baseline Reduced B-Pillar Impact Model

BMW provided a reduced model of side-impact on a baseline metal B-pillar (Figure 6-32) that is presented in Section 4.1. This metal baseline model was provided as a group of modular LS-DYNA input decks. It was decided that the new composite B-pillar should be integrated in this model by replacing the metal B-pillar components. This approach required a systemic removal of components from the metal baseline model and rerunning the simulations to make sure that the LS-DYNA input deck could run without any errors, and is described in the following section.

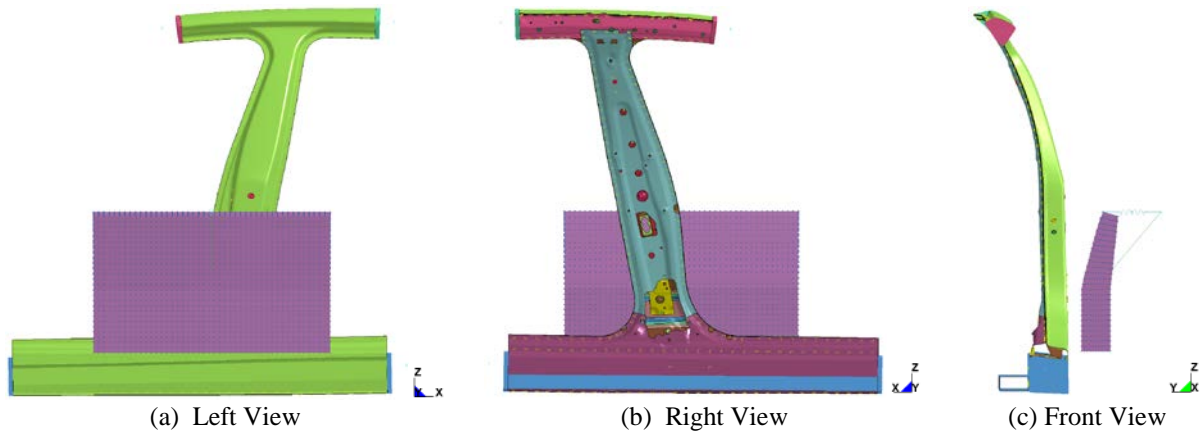


Figure 6-32. Different Views of Metal Baseline Reduced B-Pillar Impact Model  
Impact Mass,  $M = 375.31 \text{ kg}$ . Impact Velocity,  $V = 9.00 \text{ m/s}$

### 6.3.2 Separation of Metal B-Pillar From BMW Baseline Metal Model and Development of Modular LS-DYNA Input Deck System for Composite B-Pillar

Three orthogonal views of the metal baseline B-pillar are presented in Figure 6-32. On the left view, a full coverage outer skin is visible. It was decided that a cutout would be made at the root and roof locations such that the remaining rocker and roof sections could be kept unaltered. Visible in the right view, the inner parts of the metal B-pillar with other interior parts could be removed without any problem and was done accordingly. Other parts of the inner skin at the rocker and roof were kept intact. A group of spot welds were present in the model on all the edges of the B-pillar. In order to make the model clean up easy, the spot weld cards were kept without any interactions or effects on the remaining B-pillar model. Different views of the metal baseline model without the metal B-pillar are presented in Figure 6-33. Development of a composite B-pillar model is presented in Section 6.2. A composite B-pillar model needed to be attached with the rocker and roof through different contact definitions and is presented in the following section.

### 6.3.3 Contacts Between Metal and Composite Parts

The contact definitions between the rocker and the composite-B-pillar, and between the roof and the composite-B-pillar for the finalized G81 TAB design is presented in this section for brevity. At the roof location, the spine was adhesively bonded to the roof component and the hat was adhesively bonded to the spine (Figure 6-34a). Similarly, at the rocker location, The rocker was adhesively bonded to the spine, and the hat is also bonded to the spine (Figure

6-34b). In addition, the hat was also bonded to the spine at both the sides of hat-flange locations. Modeling details of the adhesive bonding is presented in the following section.

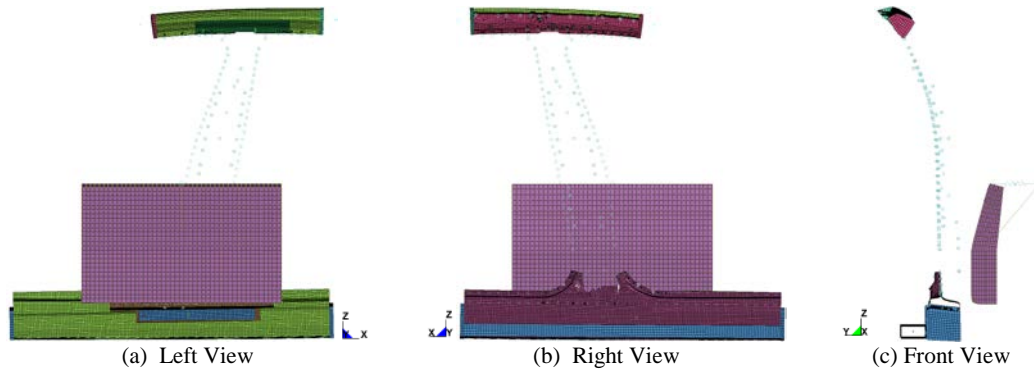


Figure 6-33. Different Views of Metal Baseline Reduced B-Pillar Impact Model With Metal B-Pillar Removed

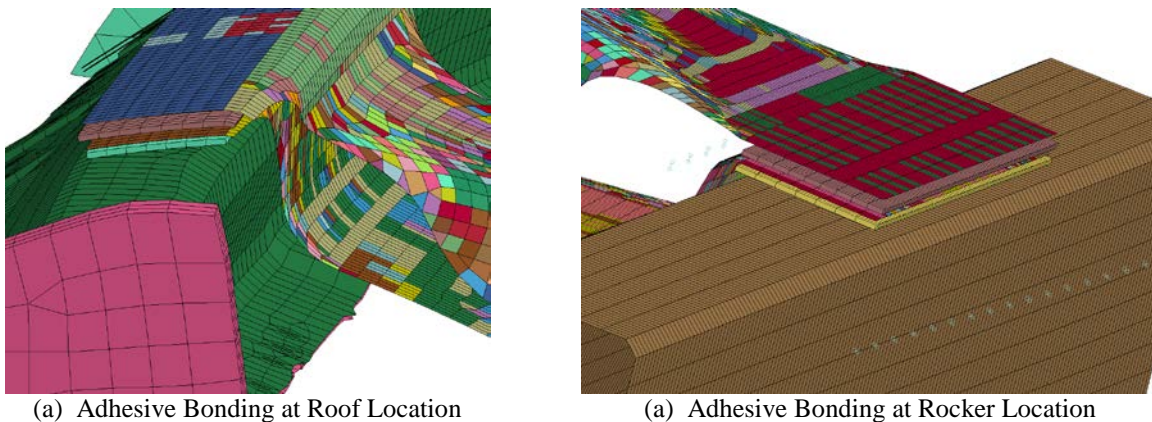


Figure 6-34. Adhesive Bond Between Roof and Composite B-Pillar and Between Rocker and Composite B-Pillar

### 6.3.4 Adhesive Joints

A non-congruent solid adhesive layer was modeled at all adhesive locations using \*MAT\_COHESIVE\_MIXED\_MODE element formulation with thickness offsets for the shell elements used for the roof, hat, spine, and rocker sections. Both surfaces of the solid adhesive elements were tied to the adjacent shell elements using the \*CONTACT\_TIED\_SHELL\_EDGE\_TO\_SURFACE\_BEAM\_OFFSET contact conditions to efficiently transfer the normal and the shear loads between the bonded joints. Material properties and parameters used for the cohesive elements will be presented in Section 6.3.7.

### 6.3.5 Selection of Composite Material Model for B-Pillar Applications

The subject composite B-pillar hat and spine components were manufactured using unidirectional prepreps or infusing the uni-directional fabrics laid following the designed laminate stacking sequence. In order to model the multi-layer composite laminates, layered shell elements were used where the draped laminate stacking sequences were defined using \*PART\_COMPOSITE keyword in LS-DYNA. Two LS-DYNA material models were considered, i.e., \*MAT\_054 and \*MAT\_059. Both of these material models have similar material model definitions and parameters except \*MAT\_054 is linear-elastic till maximum stress yield while \*MAT\_059 is non-linear up to the maximum stress yield. Even though \*MAT\_059 is non-linear, the parameters controlling the non-linearity is fixed and users have no control on those. With a

conservative approach, \*MAT\_054 was down-selected as the material model of choice for composite B-pillar application and are presented in the following section.

### 6.3.6 Material Model and Parameters

\*MAT\_ENHANCED\_COMPOSITE\_DAMAGE material model for shell elements is also known as \*MAT\_054 or simply MAT54. MAT54 is linear-elastic up to failure following maximum stress criteria, however, recent LS-DYNA version of R7 and later allows the stress to drop after failure to a limit value defined by the parameter **SLIMxx** (where, xx stands for T1, C1, T2, C2, & S; T for tension, C for compression, and S for shear). Figure 6-35 shows the representative MAT54 stress-strain behavior under axial and in-plane shear loading.

UD-CCM has used LS-DYNA composite damage model MAT54 (\*MAT\_ENHANCED\_COMPOSITE\_DAMAGE) for shell elements in the composite B-pillar design and analysis. Table 6-1 shows different important parameters (units used in parenthesis) of the MAT54 card with nomenclatures for different parameters.

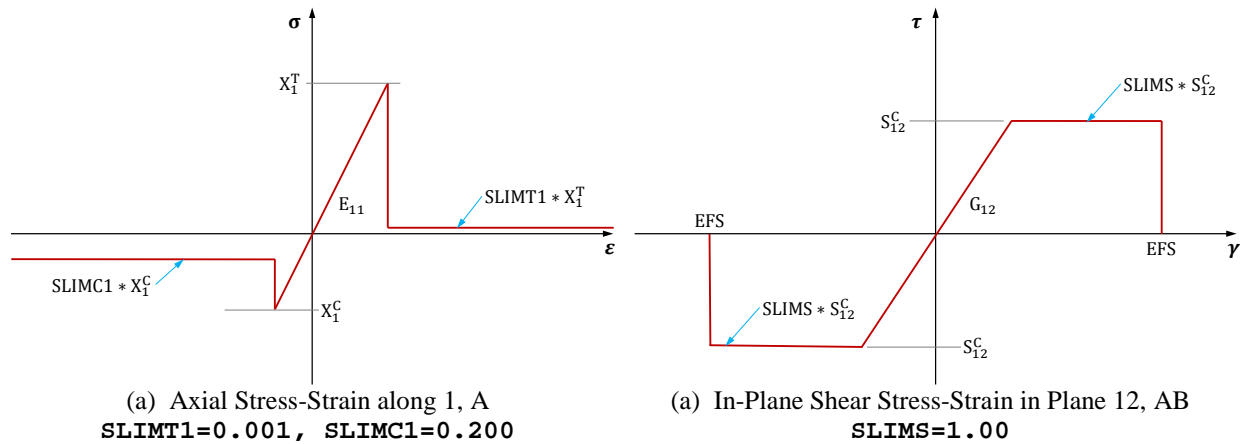


Figure 6-35. Stress-Strain Behavior Modeled in MAT54



Table 6-1. MAT54 Card Parameters

MID	RO	EA	EB	(EC)	PRBA	PRCA	PRCB
	(gmpcc)	(GPa)	(GPa)				
GAB	GBC	GCA	(KF)	AOPT	2WAY		
(GPa)							
XP	YP	ZP	A1	A2	A3	MANGLE	
						degrees	
V1	V2	V3	D1	D2	D3	DFAILM	DFAILS
TFAIL	ALPH	SOFT	FBRT	YCFAC	DFAILT	DFAILC	EPS
XC	XT	YC	YT	SC	CRIT	BETA	
(MPa)	(MPa)	(MPa)	(MPa)	(MPa)			
PFL	EPSF	EPSR	TSMD	SOFT2			
SLIMT1	SLIMC1	SLIMT2	SLIMC2	SLIMS	NCYRED	SOFTG	

### NOMENCLATURE

\$# RO: Material Density  
 \$# EA/B/C: Material Stiffness in 1, 2 and 3 directions  
 \$# GA/B/C: Material Shear Stiffness in 1, 2 and 3 directions  
 \$# XT/YT: Material Tensile Strength in 1 and 2 directions  
 \$# XC/YC: Material Compression Strength in 1 and 2 directions  
 \$# SC: Material Shear Strength in 12 Plane  
 \$# MANGLE: Material Angle  
 \$# DFAILM: Max. Matrix Axial Strain for Layer Removal (MAT54 & DFAILT>0)  
 \$# DFAILS: Max. Shear Strain for Layer Removal (MAT54 & DFAILT>0)  
 \$# TFAIL: Time Step Size for Element Deletion (<=0, No Deletion)  
 \$# ALPHA: Non-Linear Shear Stress Parameter (See MAT22)  
 \$# SOFT: Softening Factor for Crush Front Element (Default=0.10)  
 \$# FBRT: Softening Factor for Fiber Tensile Strength (XT = XT\*FBRT)  
 \$# YCFAC: Reduction Factor for Compressive Fiber Strength after Compressive Matrix Failure (XC = YCFAC\*YC, Default=2.0)  
 \$# DFAILT: Max. Tensile Fiber Axial Strain for Layer Removal (MAT54)  
 \$# DFAILC: Max. Compressive Fiber Axial Strain for Layer Removal (MAT54)  
 \$# EPS: Effective Failure Strain (MAT54)  
 \$# CRIT: Failure Criteria, 54.0=Chang-Chang, 55.0=Tsai-Wu  
 \$# BETA: Weighting Factor for Shear Term in Tensile Fiber Mode (MAT54) (MAT54, 0.0<=BETA<=1.0)  
 \$# PFL: Percentage of layers which must fail until crashfront is initiated  
 \$# EPSF: Damage initiation transverse shear strain  
 \$# EPSR: Final rupture transverse shear strain  
 \$# TSMD: Transverse shear maximum damage, default = 0.90  
 \$# SOFT2: Optional "orthogonal" softening reduction factor for material strength in crashfront elements (default = 1.0)  
 \$# NCYRED: Number of cycles for stress reduction from maximum to minimum  
 \$# SOFTG: Softening reduction factor for transverse shear moduli GBC and GCA in crashfront elements (default = 1.0)  
 \$# SLIMS: Factor-for-Minimum-Stress-Limit-after-Stress-Maximum (0<SLIMS<1)

### MAT54 Material Model Parameters and Material Cards for AS4/PEI Unidirectional Composites

The following MAT54 input cards are used to model AS4/PEI FVF = 0.55 unidirectional composites. These properties are based on experimental measurements and simplified assumptions described in Section 5.

**Material: AS4/PEI FVF = 0.55**

MID	RO	EA*	EB*	(EC)	PRBA	PRCA	PRCB
	1.588	133.76	9.722		0.0153		
GAB*	GBC	GCA	(KF)	AOPT	2WAY		
4.378							
XP	YP	ZP	A1	A2	A3	MANGLE	
						0.00	
V1	V2	V3	D1	D2	D3	DFAILM	DFAILS
						1000.0	1000.0
TFAIL	ALPH	SOFT	FBRT	YCFAC	DFAILT	DFAILC	EF5
0.000	0.100	1.00	0.100	5.165	1000.0	1000.0	0.300
XC**	XT**	YC**	YT**	SC**	CRIT	BETA	
1213.5	2406.0	128.24	53.99	113.94	54.00	0.500	
PFL	EPSF	EPSR	TSMD	SOFT2			
100.0	0.050	0.950	0.950	1.000			
SLIMT1	SLIMC1	SLIMT2	SLIMC2	SLIMS	NCYRED	SOFTG	
0.001	0.200	0.001	0.200	1.000	10.00	1.000	

\* Moduli values are in GPa. \*\* Strength Values are in MPa.

### **MAT54 Material Model Parameters and Material Cards for TENCATE AS4/NYLON Unidirectional Composites**

The following MAT54 input cards are used to model Tencate AS4/Nylon FVF = 0.44 unidirectional composites. These properties are based on experimental measurements and simplified assumptions described in Section 5.

**Material: TENCATE AS4/NYLON FVF = 0.44**

MID	RO	EA#	EB	(EC)	PRBA	PRCA	PRCB
	1.447	100.4	4.833		0.01637		
GAB##	GBC	GCA	(KF)	AOPT	2WAY		
2.41							
XP	YP	ZP	A1	A2	A3	MANGLE	
						0.00	
V1	V2	V3	D1	D2	D3	DFAILM	DFAILS
						1000.0	1000.0
TFAIL	ALPH	SOFT	FBRT	YCFAC	DFAILT	DFAILC	EF5
0.000	0.100	1.00	0.100	5.165	1000.0	1000.0	0.600
XC	XT	YC	YT	SC	CRIT	BETA	
570.80	1450.0	110.50	30.90	75.10	54.00	0.500	
PFL	EPSF	EPSR	TSMD	SOFT2			
100.0	0.050	0.950	0.950	1.000			
SLIMT1	SLIMC1	SLIMT2	SLIMC2	SLIMS	NCYRED	SOFTG	
0.001	0.200	0.001	0.200	1.000	10.00	1.000	

# E11C = 93.40 GPa is used in the final design. E22C = 7.075 GPa. ## G12 = 0.750 GPa is used in the final design.

### **MAT54 Material Model Parameters and Material Cards for ARKEMA AS4/ELIUM Unidirectional Composites**

The following MAT54 input cards are used to model Arkema AS4/Elium FVF = 0.50 unidirectional composites. These properties are based on experimental measurements and simplified assumptions described in Section 5.

Material: ARKEMA AS4/ELIUM FVF = 0.50

MID	RO	EA	EB	(EC)	PRBA	PRCA	PRCB
	1.588	122.11	7.86		0.01995		
GAB	GBC	GCA	(KF)	AOPT	2WAY		
3.585							
XP	YP	ZP	A1	A2	A3	MANGLE	
						0.00	
V1	V2	V3	D1	D2	D3	DFAILM	DFAILS
						1000.0	1000.0
TFAIL	ALPH	SOFT	FBRT	YCFAC	DFAILT	DFAILC	EPS
0.000	0.100	1.00	0.100	5.165	1000.0	1000.0	0.600
XC	XT	YC	YT	SC	CRIT	BETA	
959.75	2000.0	50.0	33.92	117.9	54.00	0.500	
PFL	EPSF	EPSR	TSMD	SOFT2			
100.0	0.050	0.950	0.950	1.000			
SLIMT1	SLIMC1	SLIMT2	SLIMC2	SLIMS	NCYRED	SOFTG	
0.001	0.200	0.001	0.200	1.000	10.00	1.000	

### 6.3.7 Adhesive Properties and Determination of Traction Law Parameters

Mixed-mode cohesive solid elements have been used to define adhesives used in the composite B-pillar design. Card image of the material model is presented below.

\*MAT\_COHESIVE\_MIXED\_MODE

MID	RO	ROFLG	INTFAIL	EN	ET	GIC	GIIC
XMU	T	S	UND	UTD	GAMMA		

```

$# EN-Normal-Stiffness : Unit=Stress/Length=MPa/mm
$# ET-Tangential-Stiffness : Unit=Stress/Length=MPa/mm
$# GIC-Mode-I-Energy-Release-Rate : Unit=Stress*Length=MPa-mm
$# GIIC-Mode-II-Energy-Release-Rate : Unit=Stress*Length=MPa-mm
$# XMU-Mixed Mode Exponent
$# T-Peak Normal Traction : Unit=Stress=MPa
$# S-Peak Tangential Traction : Unit=Stress=MPa
$# UND-Ultimate Normal Displacement = 2*GIC/T : Unit=Length=mm
$# UTD-Ultimate Tangential Displacement = 2*GIIC/S : Unit=Length=mm
$# GAMMA-Additional Exponent BK Law (Default=1.0)

```

BMW provided a set of adhesive properties for preliminary analysis and is presented below:

```

$# BMW ADHESIVE PROPERTIES
$# RO      1.00*gmpcc
$# EN      20.00*MPa/mm
$# ET      10.00*MPa/mm
$# GIC     10.00*MPa*mm
$# GIIC    60.00*MPa*mm
$# XMU     2.284
$# T       5.000*MPa
$# S       20.00*MPa
$# UND     4.00*mm
$# UTD     6.00*mm
$# GAMMA   1.00

```

Several adhesives have been characterized using through-thickness (TT) tension and lap-shear test methodology (see Table 5-6), and finally a Plexus adhesive with 50°C (122°F) cure was down-selected as the adhesive of choice. FE models of the TT-tension and lap-shear tests were developed to determine the adhesive parameters to be used in the B-pillar impact model. Figure 6-36 shows the schematic diagram, FE model, and the experimental results from TT-tension experiments. Load-displacement data obtained from TT-tension tests were reduced to nominal stress versus extension plots. These stress-extension plots were integrated to estimate the values of critical strain energy release rate (GIC) in MPa-mm unit. The average values of GIC and maximum traction T were found to be  $G_{IC} = 6.90 \text{ MPa} - \text{mm}$ , and  $T = 11.50 \text{ MPa}$ , respectively. From these average values, the maximum normal displacement was calculated to be  $u_{ND} = 1.20 \text{ mm}$ .

Figure 6-37 shows the schematic diagram, FE model, and the experimental results from lap-shear experiments. Load-displacement data obtained from lap-shear tests were reduced to shear stress versus shear displacement plots. These plots were then integrated to estimate the values of GIIC in MPa-mm unit. The average values of GIIC and maximum shear S were found to be  $G_{IIC} = 22.56 \text{ MPa} - \text{mm}$ , and  $S = 13.59 \text{ MPa}$ , respectively. From these average values, the maximum tangential displacement was calculated to be  $u_{TD} = 3.32 \text{ mm}$ .

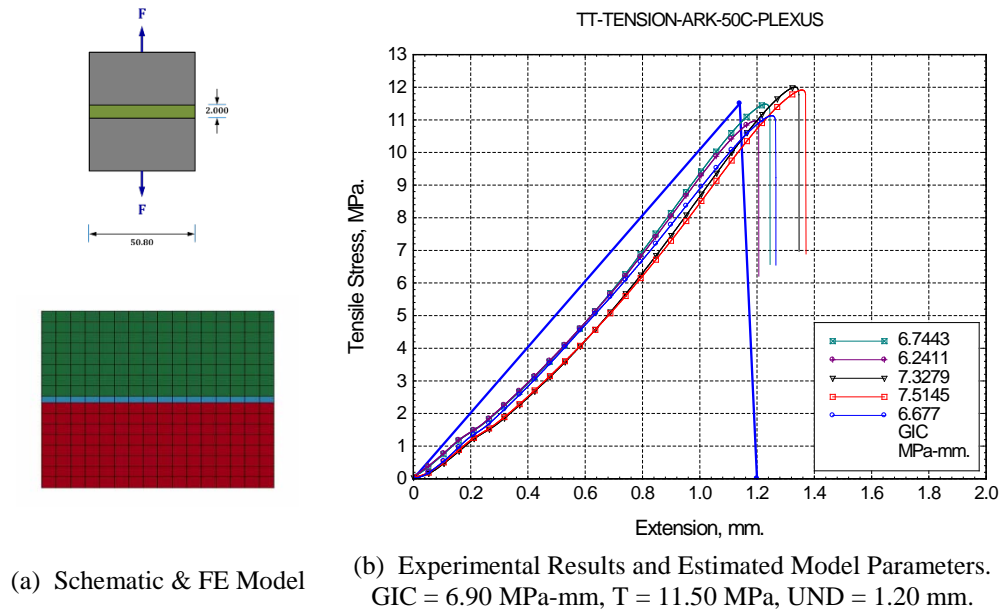
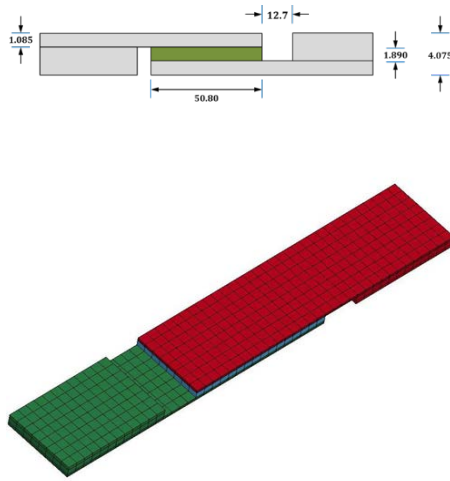
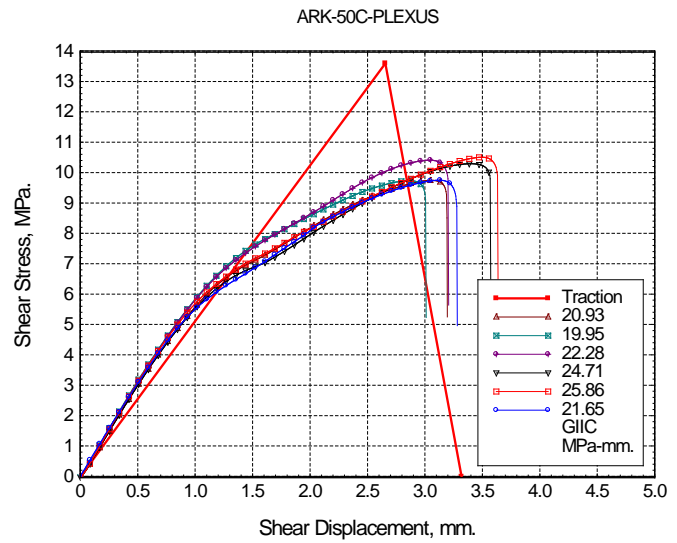


Figure 6-36. TT-Tension Tests and Estimation of Mode I Cohesive Parameters



(a) Schematic & FE Model



(b) Experimental Results and Estimated Model Parameters.  
 GIIC = 22.56 MPa-mm, S = 13.59 MPa, UTD = 3.32 mm.

Figure 6-37. Lap-Shear Tests and Estimation of Mode II Cohesive Parameters

From these estimated cohesive parameter, the normal and tangential stiffness were parametrically determined to be,  $E_T = 5.12$  MPa/mm, and  $E_N = 10.09$  MPa/mm.

In the parametric simulations, the normal and tangential stiffness were calculated using the following equations.

$$E_N = \frac{T}{u_{ND} \times f_{UND}}$$

And

$$E_T = \frac{TS}{u_{TD} \times f_{UTD}}$$

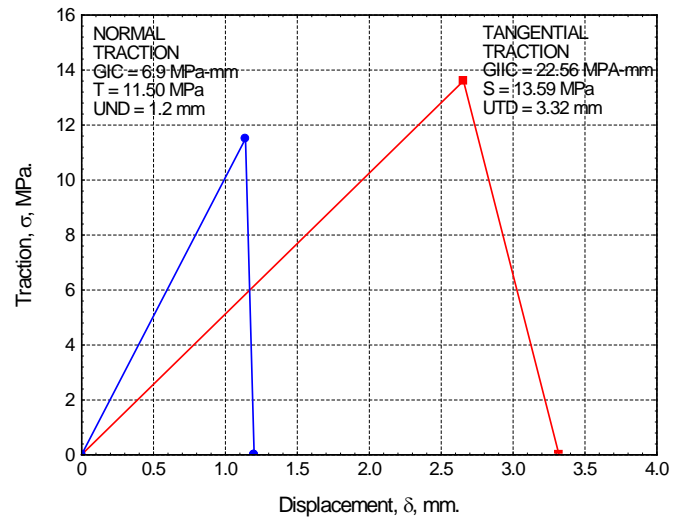
Where values of both  $f_{UND}$  (UNDFAC) and  $f_{UTD}$  (UTDFAC) were less than one. Figure 6-38a shows the values of these two factors determined parametrically to match the experimentally determines load-displacement plots. These cohesive parameters were used to model the adhesive elements and the use of the BMW adhesive was discontinued in subsequent simulations. Figure 6-39 shows the summary of cohesive parameters evaluated for different adhesives in this project.

```

$# UTD      3.320*mm
$# UND      1.200*mm
$# GIIC     22.56*MPa*mm
$# GIC      6.900*MPa*mm
$# S        2.0*GIIC/UTD
$# T        2.0*GIC/UND
$# UTDFAC   0.800
$# UNDFAC   0.950
$# ET       S/(UTD*UTDFAC)
$# EN       T/(UND*UNDFAC)
$# XMU      2.284
$# GAMMA    1.000
$# INTFAIL  4.000

$# ET       5.12*MPa/mm
$# EN       10.09*MPa/mm

```



(a) Values of Traction Law Parameters

(b) Traction Law Parameters for PLEXUS 50C Adhesive

Figure 6-38. Parametric Determination of Cohesive Parameters for Plexus 50°C Adhesive

Properties	BMW Adhesive	3M Adhesive	DOW Adhesive	PLEXUS	ARK-50c- PLEXUS
Density, g/cc	1.000	1.000	1.000	1.000	1.000
EN, Normal Stiffness, MPa/mm	20.00	0.2070	3.560	10.00	10.09
ET, Tangential Stiff., MPa/mm	10.00	0.1035	1.780	5.000	5.117
GIC, MPa*mm	10.00	0.8750	1.0012	4.500	6.900
GIIC, MPa*mm	60.00	5.2490	6.0071	28.00	22.56
XMU	2.248	2.248	2.248	2.248	2.248
T, Normal Traction, MPa	5.000	0.2302	0.6675	1.8687	11.50
S, Tangential Traction, MPa	20.00	0.9208	2.6700	7.4751	13.59
$u_{ND}$ , mm	4.000	8.000	3.000	4.816	1.200
$u_{TD}$ , mm	6.000	11.40	4.500	7.475	3.320
Gamma	1.000	1.000	1.000	1.000	1.000

Figure 6-39. Summary of Cohesive Parameters for Adhesives Evaluated

### 6.3.8 Model Validating Sub-Component Tests

A hat-section beam was down-selected as the sub-component test. AS4/Nylon prepreg tapes were used to fabricate several 18 layers hat-beams with constant cross-section and laminate stacking sequence  $[\pm 45/90/0_2/\pm 45/\pm 45]_s$ . The overall dimensions of these beams were measured to be  $L \times W \times H \times t = 360 \times 165 \times 80 \times t$  mm. The beams were crush tested in an Instron machine at a displacement rate of 600 mm/min (0.010 m/s) using a rectangular and a rounded rectangular loading block as presented in Figure 6-40.

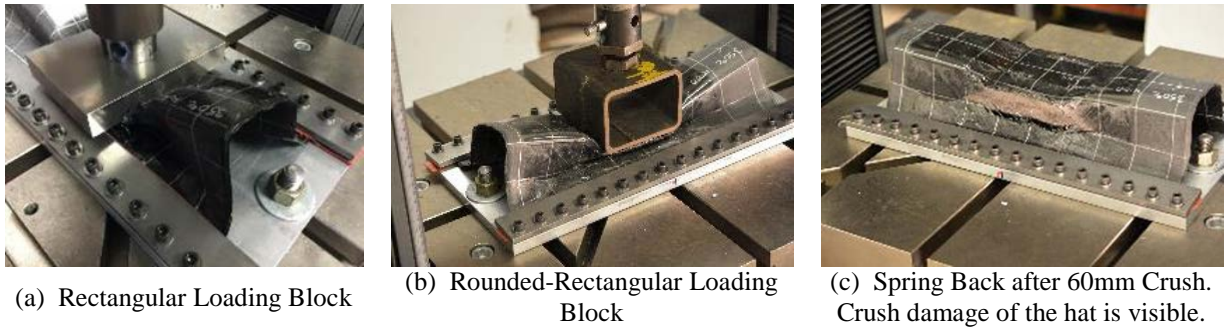


Figure 6-40. Hat-Beam Crush Test Setup

Three hat-beams were crush tested at a displacement rate of 0.010 m/s and is presented in Figure 6-41. All three beams showed similar crush behavior from which the work done for crush was calculated by integrating the load-displacement plots.

The minimum, average, and maximum values of crush energy or work done for crush were calculated to be 1813 J (minimum), 1970 J (average), and 2040 J (maximum). Tension and crush dominated damage modes are observed in the recovered hat-beam specimens.

An FE model of the hat-beam crush tests was developed to validate the MAT54 model parameters previously used in composite B-pillar simulations (Figure 6-42a). The baseline MAT54 simulation parameters (very conservative) used in this simulation is presented in Figure 6-43a. The crush behavior of the hat-beam predicted from this simulation is presented in Figure 6-42b, which shows that the average crush force is more or less constant and the crush work done (1356 J) is about 69 percent of the experimental average value (1970 J).

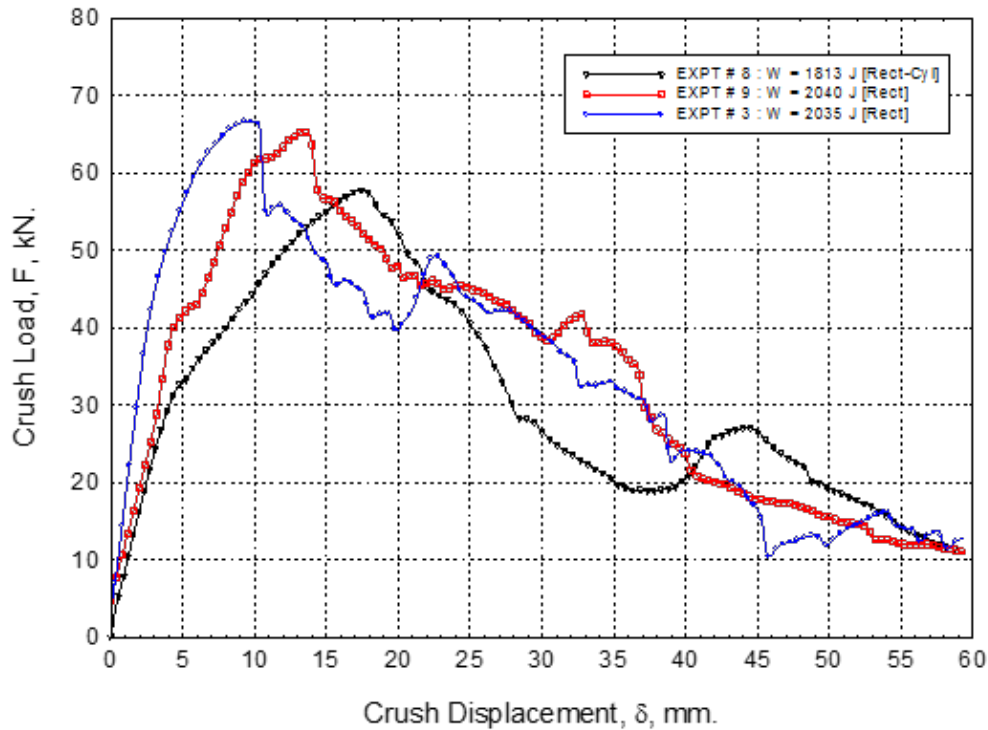
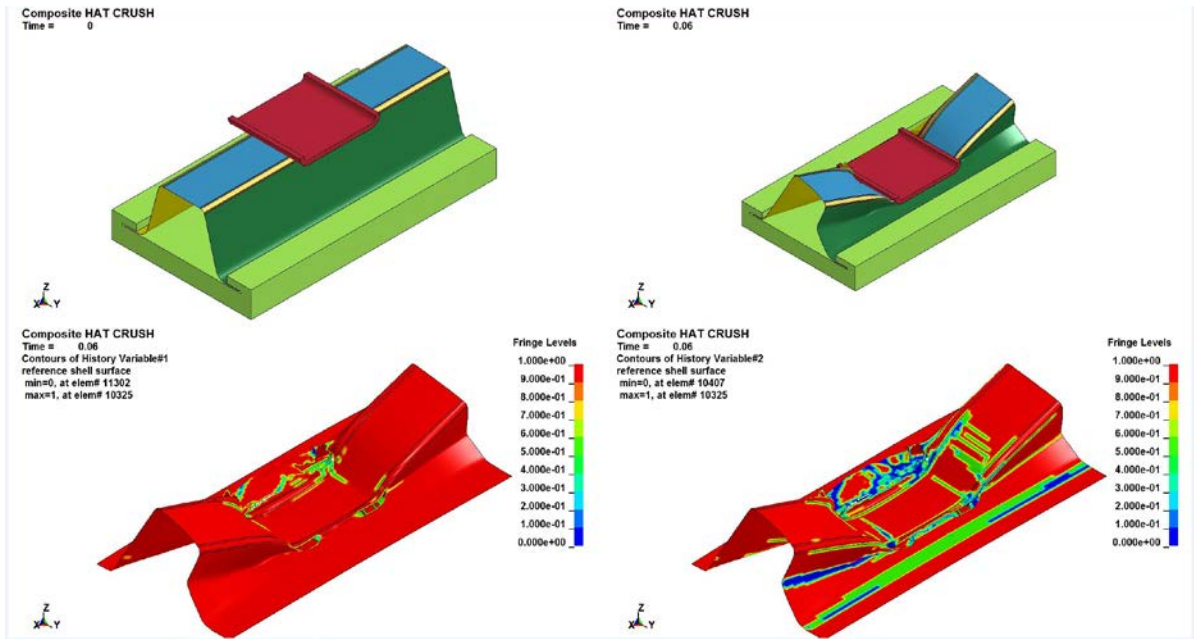
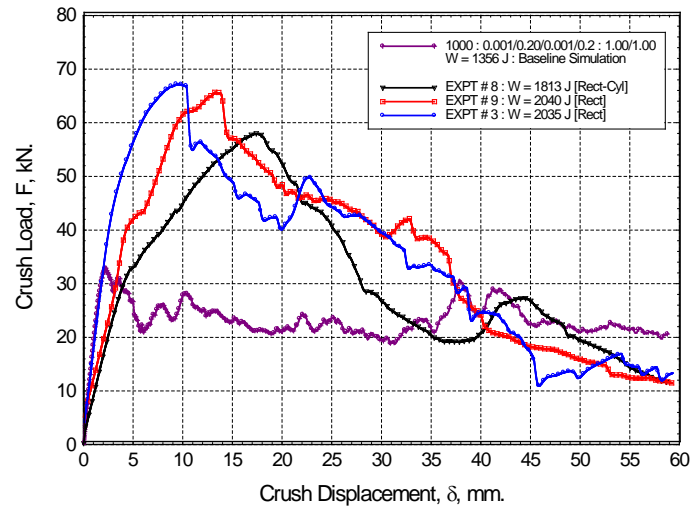


Figure 6-41. Load-Displacement of Hat-Beam Crush Tests  
Loading Rate = 0.010 m/s



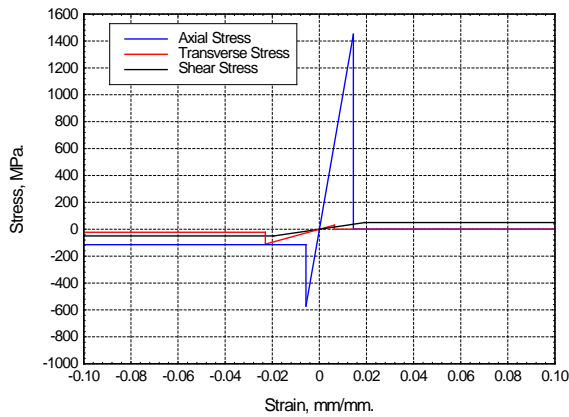


(a) FE Model of the Hat-Beam Crush Experiment and Predicted Deformation and Damage Modes.



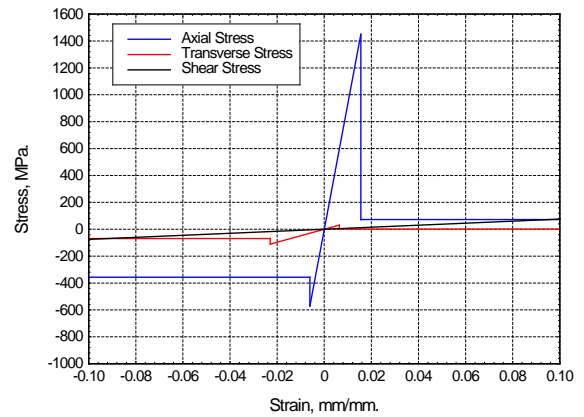
(b) Prediction of Load-Displacement using Baseline MAT54 Modeling Parameters.

Figure 6-42. FE Model of Hat-Beam Crush Test and Simulation with Baseline Parameters



SLIMT1 = SLIMT2 = 0.001  
 SLIMC1 = SLIMC2 = 0.200  
 SLIMS = 1.000

(a) Baseline MAT54 Simulation Parameters



SLIMT1 = 0.050, SLIMT2 = 0.100  
 SLIMC1 = SLIMC2 = 0.625  
 SLIMS = 1.000, G12 = G12/3.45  
 S12 = S12 x 1.50

(b) Optimized MAT54 Simulation Parameters

Figure 6-43. Baseline and Optimized MAT54 Simulation Parameters

The limit stress after failure (SLIM<sub>xx</sub>) used in the baseline hat-crush simulations (Figure 6-43a) were parametrically varied to obtain a set of optimized MAT54 parameters (Figure 6-43b and in the below input card for TENCATE/NYLON) that maximized both the crush force and the work done due to crush. Figure 6-44a shows the deformation and damage predicted using the optimized MAT54 modeling parameters, and Figure 6-44b shows the different parametric predictions of crush-loads.

### MAT54 Material Model Parameters and Material Cards for TENCATE/NYLON

Material: TENCATE/NYLON FVF = 0.44

MID	RO	EA	EB	(EC)	PRBA	PRCA	PRCB
	1.658	100.4	4.833		0.01637		
GAB	GBC	GCA	(KF)	AOPT	2WAY		
2.41 0.75							
XP	YP	ZP	A1	A2	A3	MANGLE	
						0.00	
V1	V2	V3	D1	D2	D3	DFAILM	DFAILS
						1000.0	1000.0
TFAIL	ALPH	SOFT	FBRT	YCFAC	DFAILT	DFAILC	EPS
0.000	0.100	1.00	0.100	5.165	1000.0	1000.0	0.600
XC	XT	YC	YT	SC	CRIT	BETA	
570.80	1450.0	110.50	30.90	50.00 75.00	54.00	0.500	
PFL	EPSE	EPSR	TSMD	SOFT2			
100.0	0.050	0.950	0.950	1.000			
SLIMT1	SLIMC1	SLIMT2	SLIMC2	SLIMS	NCYRED	SOFTG	
0.001	0.200	0.001	0.200	1.000	10.00	1.000	
0.050	0.625	0.100	0.625				

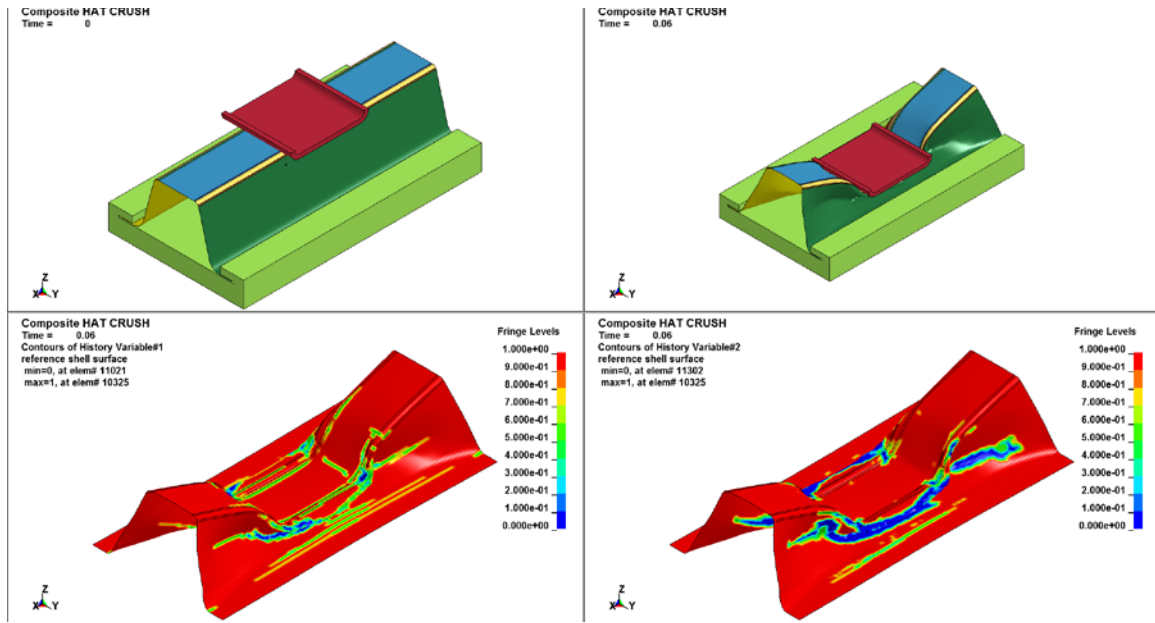
The deformation shapes and damage modes predicted using the optimized MAT54 parameters closely matched with the experimental observations. The peak load predicted was less than that of the experiment but the crush energy was matched with the average crush energy of the experiment. One important observation was that through-thickness interlaminar delamination (one to three) planes were observed in the crush tested specimens at the fillet radius of the hat-section. MAT54 with the layered shell elements used in the present analysis does not

consider interlaminar stresses and interlaminar delamination and remains as an unsolved problem as future work.

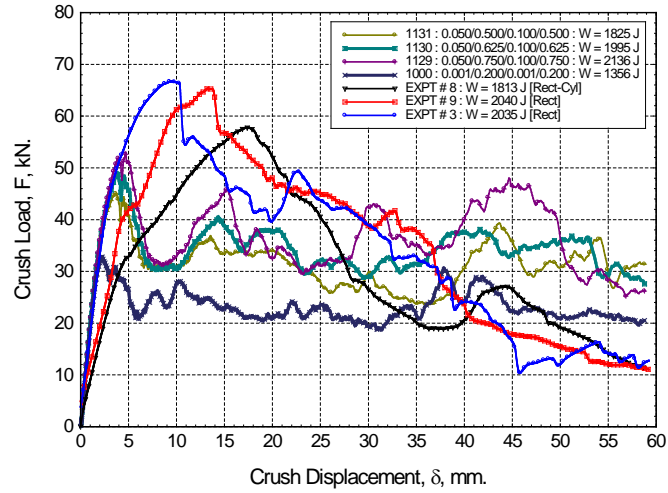
## 6.4 G81 TAB Composite B-Pillar Model Validation with New MAT54 Model Parameters

The G81 TAB Composite B-pillar model has been updated several times to accommodate as manufactured thickness and changes in laminate stacking sequences. The final run of this model was designated as 110C-G81. In the 110C-G81 run, the spine was modeled with the experimentally determined properties of Armema AS4/Elium UD composites and the hat was modeled with the experimentally determined properties of AS4/NYLON UD composites.

MAT54 optimized model parameters were used to simulate the B-pillar design 110C-G81 and compared with the metal baseline. The 110C-G81 run with updated material properties and parameters was designated as 110C-G81-NPP-THK (NPP – new properties and parameters, THK – as manufactured thickness). Figure 6-45 shows the time history of contact-force and impactor RBV, force-displacement, maximum intrusion profiles, and deformation shape at time  $t = 30ms$ .

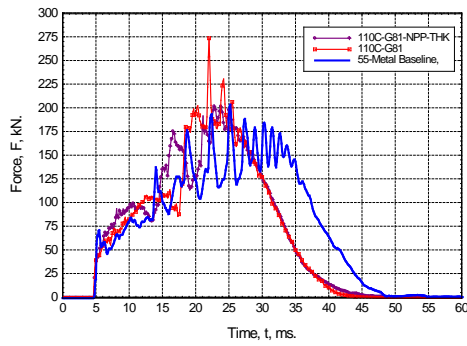


(a) Predicted Deformation and Damage Modes using the Optimized MAT54 Model Parameters.

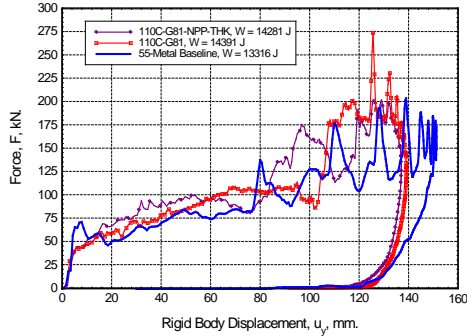


(b) Prediction of Load-Displacement varying the MAT54 Modeling Parameters.

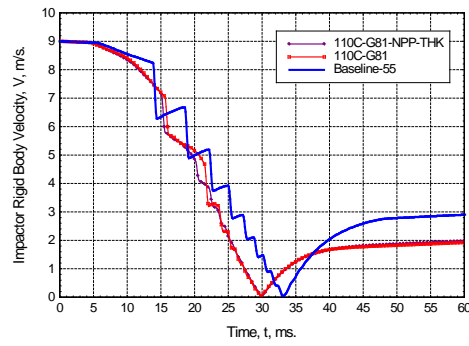
Figure 6-44. Parametric Optimization of MAT54 Model Parameters for Maximizing Crush Force and Crush Work Done



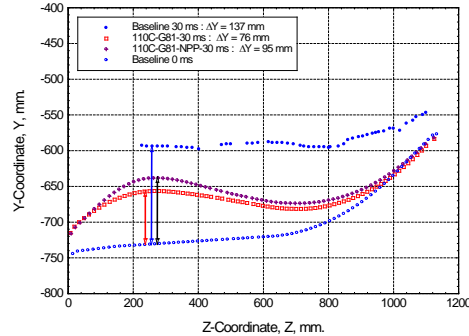
(a) Time History of Contact Force



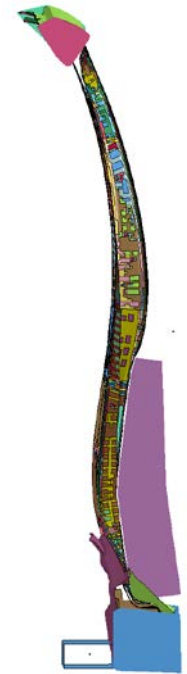
(c) Force-Displacement and Work Done



(b) Time History of Impactor RBV



(d) Comparison of Maximum Intrusion with Metal Baseline



(e) Deformation at 30 ms

Figure 6-45. Model Validation of Composite B-Pillar Design 110C-G81-NPP-THK-RUN-4 with Experimentally Validated MAT54 Material Parameters

Time history of contact force in the impact-contact phase ( $5 \text{ ms} < t < 30 \text{ ms}$ ) showed noticeable difference with the baseline 110C-G81 run. The average crush load was higher, peak loads are lower and comparable with the metal baseline. The rebound or unloading phase was very similar to baseline 110-G81 run. The difference in crush force appeared as some differences in the time history of the impactor RBV in the time range  $15 \text{ ms} < t < 25 \text{ ms}$ . Difference in the crush load was clearly visible in the crush force versus displacement plot.

Finally, the maximum intrusion of 110C-G81-NPP-THK was about 19 mm higher than the baseline 110C-G81 run, however was about 45 mm less than the metal baseline intrusion. Overall performance of the final B-pillar design (110C-G81-NPP-THK) was similar to the previous design run 110C-G81 and fulfilled all design requirements.

## 6.5 Summary and Conclusions

A design and analysis methodology for composite B-pillar were developed and demonstrated. Current modeling tools cannot directly provide keyword output of as-draped laminate stacking sequence for LS-DYNA analysis, however, provides NASTRAN BDF files. An automated tool has been developed to convert the BDF files to LS-DYNA keyword files. Future Hyperworks version will have this LS-DYNA export capability.

A grid-based CATIA modeling approach was undertaken to design the laminate stacking sequence and develop the ply pattern needed for part fabrication/processing. A two-part composite hat and spine B-pillar has been designed and analyzed to match or exceed baseline metal B-pillar performance. An adhesively-bonded TAB design featuring openings at the rocker and roof sections has been proven to eliminate strain concentration in the spine due to local

hat crush, and was down-selected as the final composite B-pillar design. The finalized G81 TAB design weighs 43 percent of the metal baseline, i.e., the composite B-pillar is 57 percent lighter than the baseline.

A sub-component hat-beam crush test method was used to validate the modeling properties using experimentally measured material properties. The validated material model was finally used to recheck the final design, and satisfied all the design requirements. The model validating sub-component test thus provided an experimentally determined and computationally validated set of material properties and MAT54 model parameters for shell elements for two different composite materials, i.e., AS4/Nylon (FVF = 0.44) and Arkema/Elium (FVF = 0.50) unidirectional composites.

# 7. Processing and Part Fabrication

## 7.1 Introduction

Low production rate (single to 10s of parts) chlorofluorocarbon structural components have been used in high-performance cars since the early 1990s and continued exponential growth will be observed over the next 20 years (Figure 7-1). CFCs are able to meet performance requirements without significant cost considerations reflected in the use of aerospace grade materials and processes such as hand layup and autoclave cure. Over the last 10 years, General Motors (GM) and Chrysler integrated composites into their sport cars (GM Corvette and Chrysler Viper) implementing higher-volume manufacturing processes improving affordability. For the first time, the introduction of the BMW i3 (2013) and i8 (2014) into the regular consumer market in Europe (2014 in the United States) required mass production processes and supply chain considerations to meet 20,000+ rates per year. Plasan has implemented a 17-minute cycle time process using epoxy prepreg material with production rates reaching approximately 2,000 units for the GM Corvette ZR1 hood. BMW is meeting its initial >20,000 units (including the frame structure and various body panels) per year goal using automated preforming in combination with high-pressure resin transfer molding. Automation of the preforming stage, resin infusion and joining process are key to reduce production times, variability and cost. Nevertheless, carbon fiber yield rate is still low due to incoming material rejects and waste during the preforming and infusion process increasing effective material costs significantly. Another potential automotive processing approach is forming of thermoplastic engineered blanks into final geometry. This would meet cycle time requirements but the process has not been proven out to meet quality in large complex geometries. For main stream vehicles (>100k units per year), material cost, as well as the need to meet cycle times for high-volume manufacturing methods (less than 3 minutes per part) is still limiting the widespread implementation of CFC in vehicle structures.

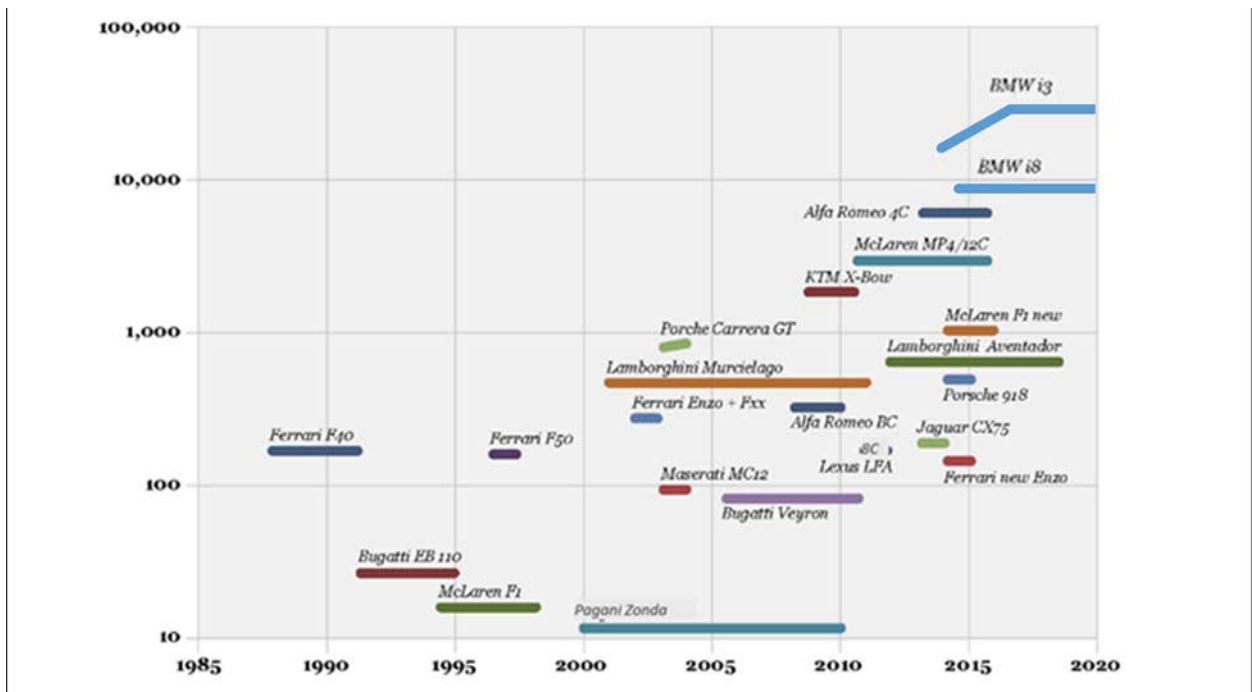


Figure 7-1. Several New Programs Considering Composites at Much Higher Volumes



This project involved evaluating both liquid molding processing and forming of engineered blanks to produce the spine and hat component of the B-pillar. The processing approaches are described, part quality was evaluated and the joining process to assemble the full B-pillar is explained. UD-CCM implemented a new forming cell to allow fabrication of engineered blanks and the forming of the blanks in a heated press system to produce the hat section. VARTM including fabrication of the dry preform followed by infusion and cure allowed spine production meeting the high-fiber volume fraction requirements. Tooling for both processes were designed, fabricated and met tolerance requirements. The tools were used as a tooling jig for final assembly. Developing these processes for thermoplastics materials required the development of innovative approaches due to the new materials and complex geometries designed. Inspection of individual components and final assembly as well as final drop tower test indicated that high-quality production of automotive parts is possible with these materials and processes.

## 7.2 Liquid Molding Processing of Spine

During liquid composite molding processing a dry fiber textile is impregnated with a liquid low-viscosity resin. The applied pressure gradient between the injection and vent gate allows resin infiltration of the fiber reinforcements. The quality of the cured composite part depends on the degree of compaction, impregnation and cure. The impregnation can be characterized using simulation tools based on Darcy's law. The important material parameters are the resin viscosity behavior and the permeability of the reinforcement. Processing variables include the magnitude of applied pressure – up to 100-150 bar in high-pressure resin transfer molding to 10 bars in RTM to vacuum only in vacuum-assisted RTM. Traditionally for RTM, the in-plane permeabilities need to be considered because flow gradients do not exist through the thickness of the part. Alternate LCM processes such as the VARTM process or the resin film infusion process exhibit significant through-the-thickness impregnation gradients and the out-of-plane permeability drive the cycle times of the infusion.

Various LCM variation including processing in the autoclave at higher pressures and elevated temperature infusion were evaluated in the project. Nevertheless, VARTM processing at room-temperature with long gel-time thermoplastic resin was down-selected to fabricate the spine parts. It allows low-cost tooling approaches while producing sufficiently high-volume fractions parts and can be readily applied for prototyping and large-scale structures manufacturing (Figure 7-2). VARTM incorporates a highly permeable distribution medium incorporated as a surface layer on the preform. During infusion, the resin flows preferentially across the surface and simultaneously through the preform thickness. VARTM is a closed process on a single-side tool thus reducing tooling cost. VARTM is an ideal composite process for prototyping and low-production rate manufacturing.

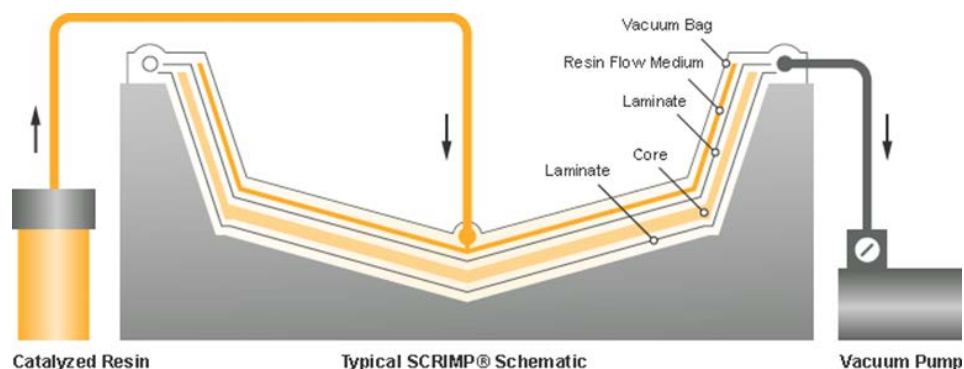


Figure 7-2. Schematic of VARTM Process [<http://www.tpicomposites.com/?id=9>]

Tooling was designed to accommodate the spine geometry and allowed placement of the vacuum bag and plumbing. Flat pattern of the preform design was generated and cut from unidirectional T700 carbon fabric supplied by Chomarat Textiles Industries, France (C-Weave UT270P 12k FOE) with a width of ~132.08 cm (52 in.) (Figure 7-3). An adhesive layer (Spunfab PA1203/1 – 0.250 oz./yd<sup>2</sup>) was added through a heat treatment to minimize any loss of individual tow bundles as the material was cut and handled. Spine plies included 0, 45 and 90-degree directions plies and as all zero ply length exceeded the roll length had to be assembled from two cut plies. All ply pattern were cut on an automated ply cutter, labeled and kitted for further processing. All plies were manually placed on the tool, corners were further heat treated and compacted using a heat gun and hand rollers to adhere to the tooling surface. This minimizes wrinkling and local bridging of the plies. Placement of each ply was recorded in a traveler to ensure correct placement. The final assembly was heat treated under vacuum at 121°C (250°F) for an hour and resulted in a good dimensional stable preform that was further processed for final infusion.

An air permeable membrane was applied on the tooling surface and separated by a peel ply from the preform. A distribution media was placed on top of another peel ply and two infusion ports were placed equally spaced on the surface (Figure 7-4). Plumbing to an injection bucket and two vacuum ports connecting to the tooling surface were hooked up. Vacuum at approximately 28 inches in mercury was applied and held throughout the infusion. A leak check was performed to ensure good sealing of the preform to atmospheric pressure.

Rheology of Elium 150 and 180 from Arkema was evaluated with a viscometer. Elium 150 with 2 percent AFR 40 (BPO) provides a gel time between 20-30 minutes after hand mixing while Elium 180 extended gel time significantly to more than 80 minutes. Initial starting viscosity was approximately 100cP and rises rapidly around the gel time of the mix (Figure 7-5). Elium 180 viscosity profile allows 4x longer infusion times and thus 2x improved flow distance in the preform reducing risk of any potential dry-spot development due to macroscopic flow issues. The membrane creates a vacuum surface on the tool and thus provides a possible air path in case dry-spots develop on that surface. This ensures robust infusion of the preform minimizing the risk of large void space being formed.

Initial infusions showed significant void space close to the injection locations. These areas were initially filled but emptied at the end of the infusion. Visual observation indicated an air bubble developing and growing in the injection tube. Tests were conducted to evaluate the evaporation of the resin at room temperature without catalyst indicating significant mass loss over an hour. The pressure in the injection gates at the end of infusion will drop to almost atmospheric pressure. It was speculated that this allows generation of vapors in the infusion areas resulting in an increase in vapor pressure pushing the resin out of the preform area locally. The effect led to the observed dry-spot development (Figure 7-6). In all further experiments, the injection ports were inverted to a vent as gelation in the resin bucket was observed. This minimized vapor generation and thus dry-spot development.

Over the project period 10 spines were produced with 5 being used for impact testing. The first 8 spines are shown in Figure 7-7. Geometry and quality were evaluated visually, through thickness measurements and ultrasonic C-scans and deemed acceptable for these 5 spines.



Figure 7-3. Preform Kitting and Assembly on Tool

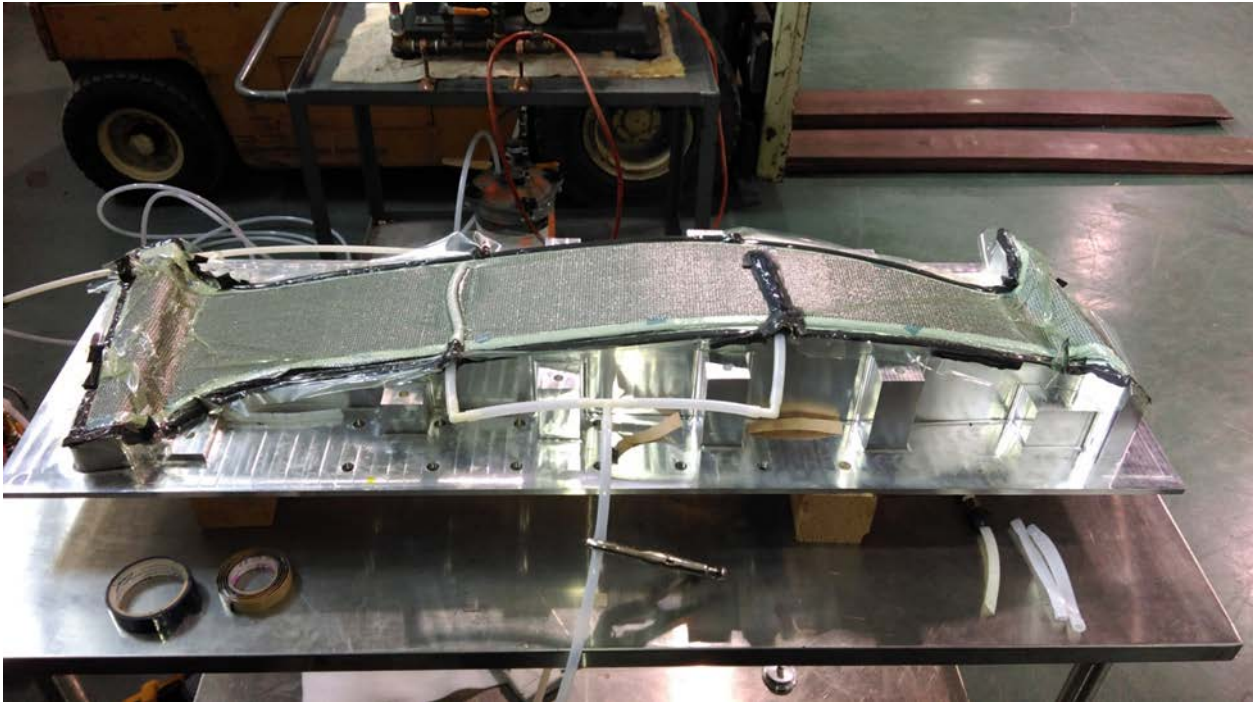


Figure 7-4. Final Infusion Setup of Spine

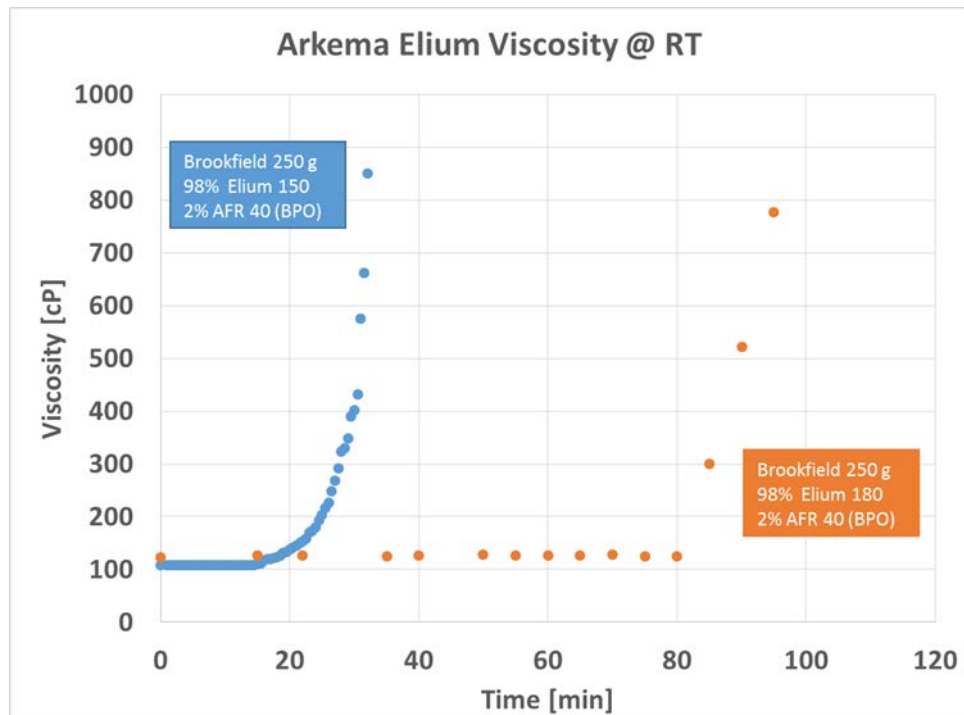


Figure 7-5. Viscosity Behavior of Elium Resin Systems



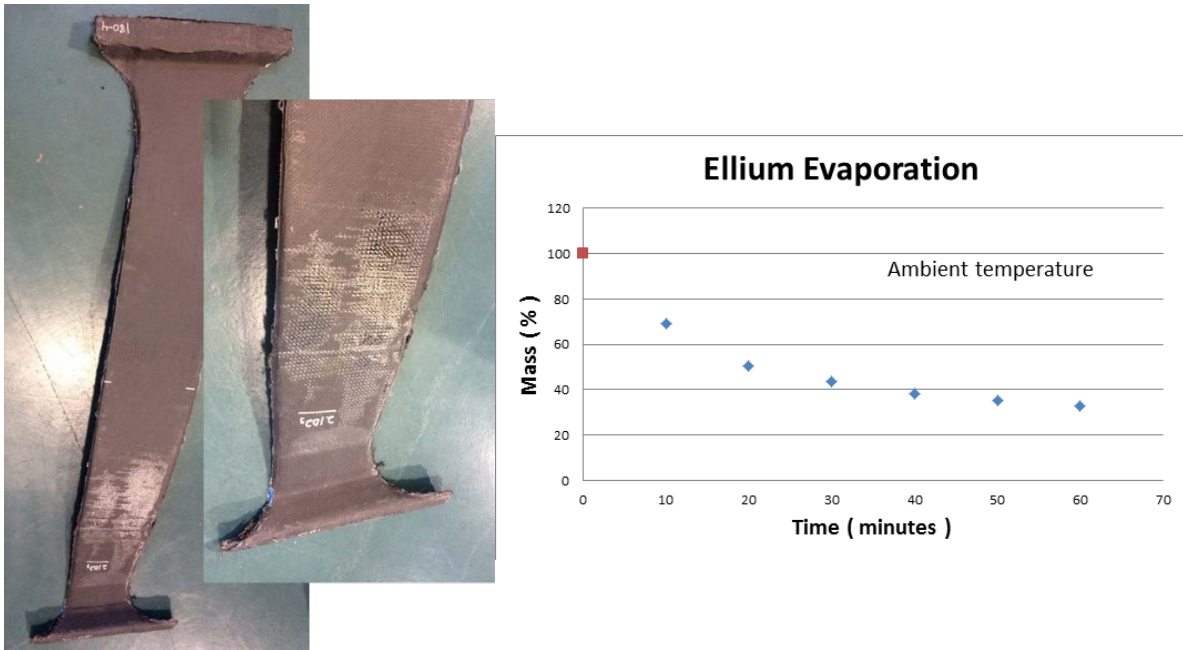


Figure 7-6. Dry-Spots After Infusion and Evaporation Behavior of Elixir Resin



Figure 7-7. Initial Production of 8 Spines

### 7.3 Hat Section Manufacturing

Forming of continuous unidirectional carbon fiber thermoplastic parts is still in its infancy with limited thermoplastic unidirectional prepreg material availability coupled with no established simulation tool to predict the forming process. The major processing challenge is the forming of the heated but still viscous blank material over the tool. Polymer and fiber movement is a function of the rheology of the composite material, temperature and temperature gradient in the blank as well as geometry and forming speed during pressing. This is in particular an issue when doubly-curved structures are being built. This manufacturability aspect was integrated in the design aspect and the hat section geometry featured a mainly singly-curved structure with

only a small section at the rocker and roof area being doubly-curved. Draping simulations of flat patterns were used to predict final orientation and has been outlined in Section 6. This allowed prediction of final fiber location and orientation in the pressed hat section.

The three major processing steps include consolidation of an engineered blank and heating of the blank followed by forming of the blank in a die. The NHTSA program established a three-stage thermoforming system at UD-CCM that integrated a 54 kW infrared (IR) heater station, blank preparation station with a shuttle in a 150-ton press system (Figure 7-8). The system allowed placement of the blank into the shuttle, rapid heating of the blank under the IR heater followed by forming in the press section. The system was used to produce flat components for mechanical tests and small-scale hat sections for sub-element testing. During full-scale hat production, the engineered blank was heated in the press using convection and then pressed in shape.

### 7.3.1 Incoming Prepreg Quality

The Tencate tape material has a unique microstructure where fiber tows are not spread equally resulting in a distinct separation of fiber bundles and resin with voids entrapped in the polymer (Figure 7-8). This microstructure has to be reprocessed during blank fabrication and final forming to result in a composite with good distribution of fibers without voids for full property translation.

### 7.3.2 Blank Evaluations

Various blanks were fabricated in an oven under vacuum conditions and microstructural quality were evaluated. Two different consolidation cycles were used and included a 222°C (431°F) and 250°C (482°F) heating and cooling ramp (3.5°C per minute). The ply thickness were measured and compared to the incoming prepreg material and autoclaved processed part (Figure 7-10). The incoming material was approximately 6.6 mm thick and consolidated to 5.34 mm [0]<sub>6</sub> and 5.7 mm [0/90]<sub>2S</sub> per ply thickness for the autoclave processed parts. The cross-ply layup does not allow significant nesting of the individual plies and thus results in slightly thicker parts. The vacuum processed ply thickness was significantly higher for the lower temperature ramp (6.44 mm and 6.72 mm) processed components but higher temperature vacuum processing allowed enough resin flow and void reduction to reach similar per ply thickness (5.76 mm and 5.75 mm) as the autoclave parts.

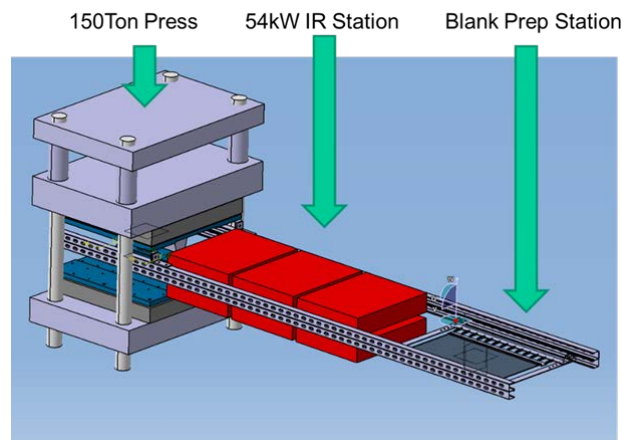


Figure 7-8. Schematic of Forming Station

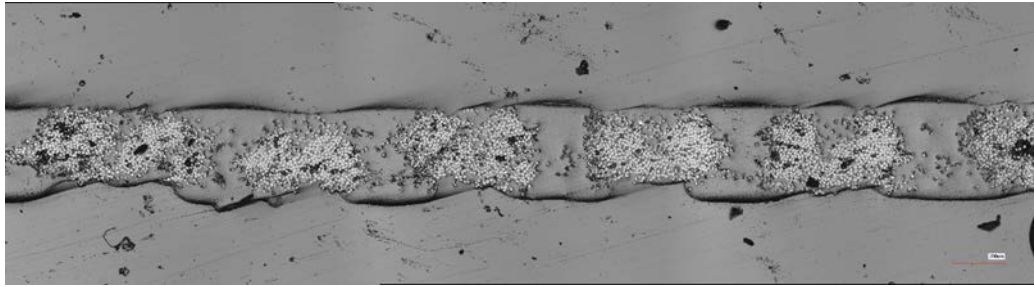


Figure 7-9. Microstructure of Incoming Tencate Tape Material

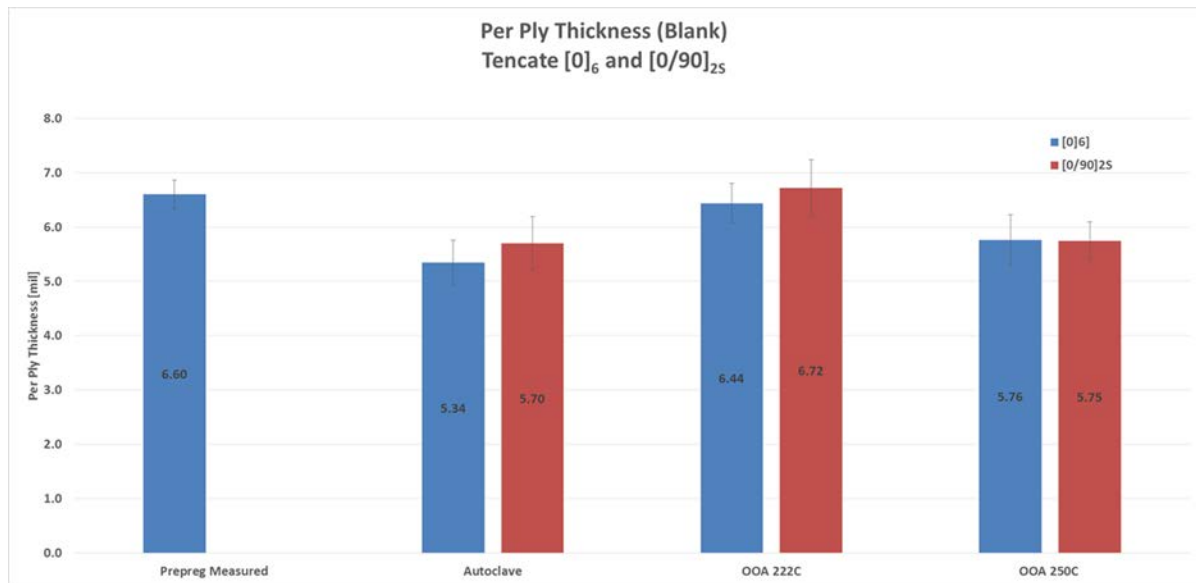


Figure 7-10. Thickness Information of Prepreg and Processed Material

Microstructural observation confirmed that the 250°C (482°F) process cycle allowed resin and fiber flow to create a more uniform microstructure similar to autoclave parts (Figure 7-11). No significant fiber movement is observed at the lower temperature consolidation cycle but individual plies were consolidated to each other. At the higher processing temperature, fiber bundles were broken up, voids were displaced and/or collapsed and good distribution of fibers was observed.

Final evaluation measured the blank quality using ultrasonic evaluation. The C-scan of the single ply had high attenuation but showed areas of lower attenuation along the fiber direction (Figure 7-12). Overall, the scan showed the non-uniformity of the incoming material. After autoclave and higher-temperature vacuum consolidation, per ply attenuation dropped significantly and the panel attenuation was more uniform. In contrast, the lower temperature vacuum consolidation cycle still showed the higher-attenuation features of the prepreg likely from the individual fiber bundle containing large void space.

The results showed that the high-temperature vacuum consolidation cycle resulted in high-quality components and this process cycle was used for all blanks produced in subsequent tests.



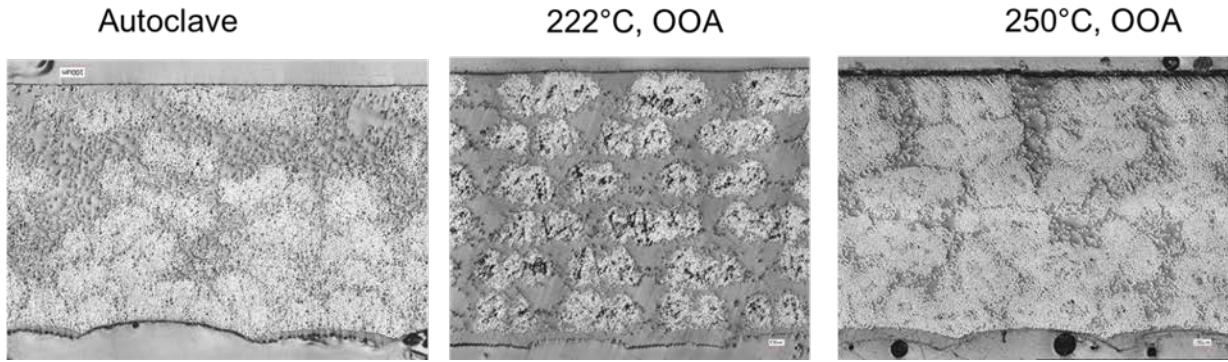


Figure 7-11. Microscopic Images Reveal Processing Effect on Microstructure

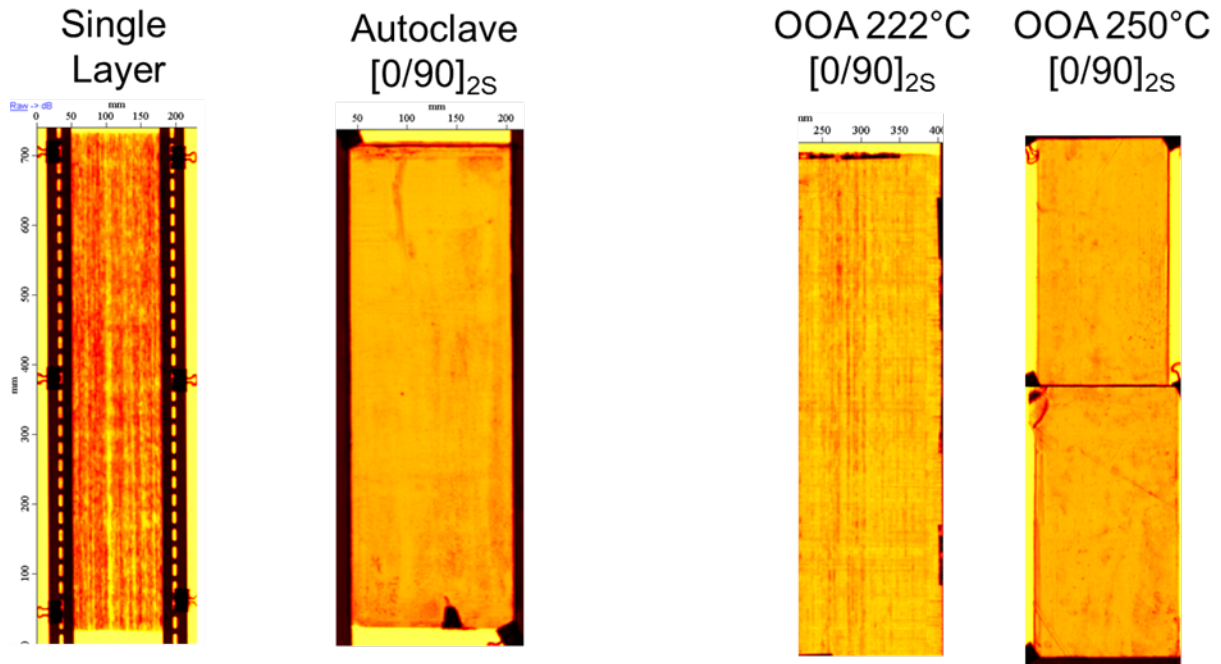


Figure 7-12. Ultrasonic C-Scan Indicate Part Variation for Different Process Conditions

### 7.3.3 IR Heating and Forming Process

As shown in Figure 7-13, blanks 30.48 cm x 30.48 cm (1 ft. x 1 ft.) were heated in the IR heating system and then formed under a flat tool in the press. The IR heaters were controlled to 400°C (752°F) and the temperature rise on the surface and center point were measured as the blank was located under the heater system. A processing temperature of around 250°C (482°F) similar to the blank fabrication was targeted. The target temperature was reached after approximately 45s resulting in a maximum heating rate of ~10°C/s at the start of the process. For the thin uni [0]<sub>6</sub> component, temperature gradient through the thickness was less than 5°C. The blank was shuttled from the IR heating area to under the press where the lower platen was engaged until pressure reached 3 tons. This process took less than 10 seconds and dropped the blank temperature by about ~15°C. Temperature significantly drops as the cold tool engages the part with cooling rates of up to 100°C/s.

Per ply thickness and quality was evaluated. Ply thickness reduced to autoclave level (5.24 mm and 5.37 mm respectively) that was both a result of squeeze out of material increasing the surface area slightly as well as improved consolidation (Figure 7-14). Void level was minimum and fiber distribution had not changed significantly compared to the blank.

Overall, the analysis shows that deconsolidation was either not occurring during heating or that the forming process reconsolidated the parts to acceptable levels.

### 7.3.4 Sub-Element Hat Section Production

Aluminum hat tooling was fabricated and integrated into the press system (Figure 7-15). The tool was designed to have a maximum coupon thickness of 0.762 cm (.3 in.), but rubber inserts allowed good pressure translation for thinner blanks.

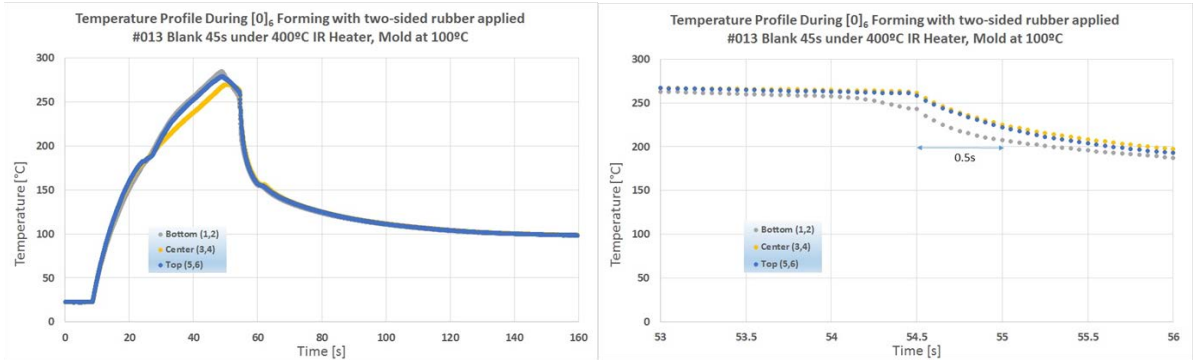


Figure 7-13. Temperature History During Heating and Forming of Blanks

OOA 250°C  
Formed, [0]<sub>6</sub>

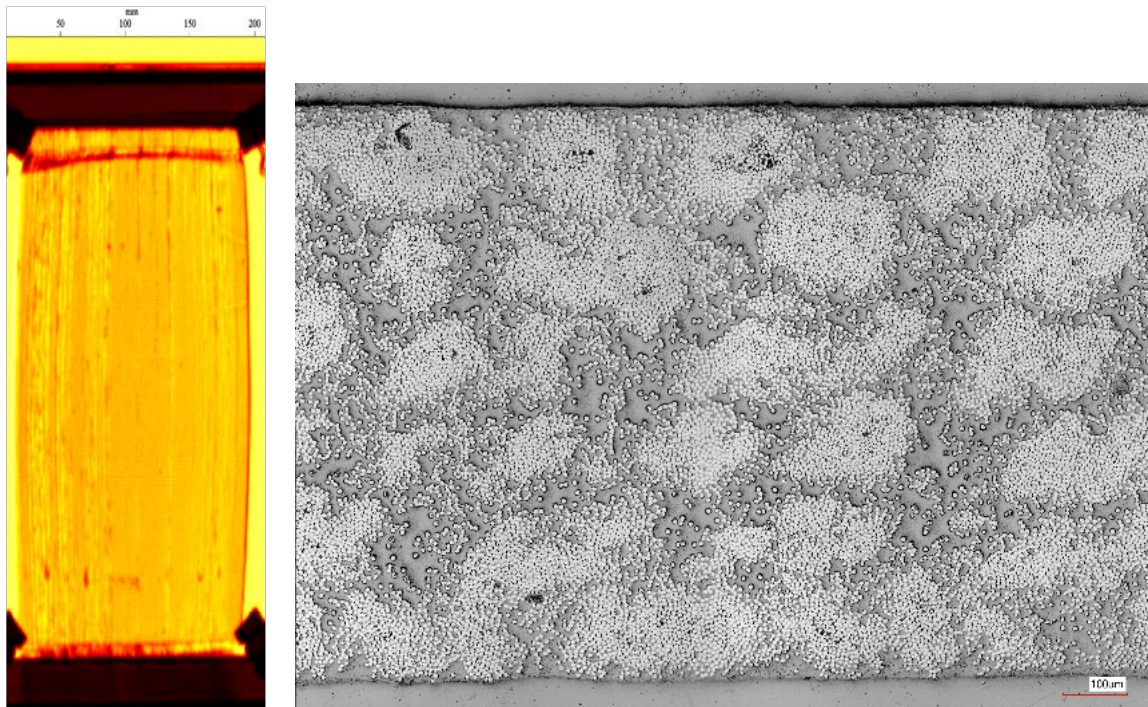


Figure 7-14. Optimized Forming Process Leads to Desired Microstructure and Quality

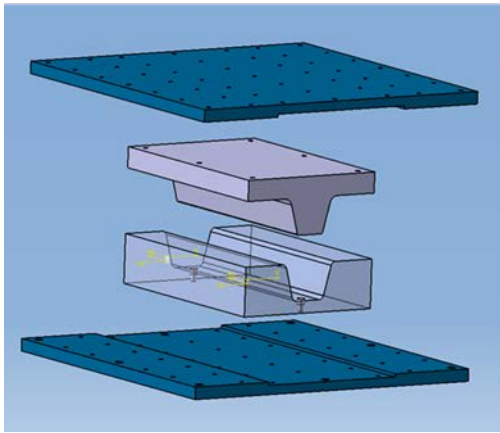


Figure 7-15. Sub-Element Hat Tooling

Trials were conducted with  $[0/90]_{2S}$  blanks to evaluate forming issues on this single-curved component with the forming process described before. Microscopic analysis of the cross-sections at various points in the components were evaluated and compared to the flat components. Visual inspection indicated some limited squeeze-out of material on the top and side flanges. This indicated that the applied pressure moved some of the polymer to the part edges and squeezed out excess resin. Surface quality was very good on the direct tool side. The radii were well developed but some small wrinkles were observed at the left and right wall close to the radii. The mold was in contact with the vertical walls as the die was closing and the draped material at the radii bridged the section and was captured as a minor wrinkle.

The microscopic photos clearly indicate good consolidation translation from the blanks into the formed parts. Void content in all areas is minimum. Thicknesses were well maintained except in the top radii where thicknesses were reduced by 15 percent. Here the material was in contact with the mold for an extensive period of time during closure, the 90-degree radii material was thinning out due to both vertical compaction pressure as well as horizontal tension pressure coming from the wall areas.

The blank thickness was measured prior to forming and showed an average per ply thickness of 5.28 mm with standard deviation of 0.16 mm. After forming thickness was 5.28 mm  $\pm$ 0.41 mm confirming the microscopic analysis. Overall, quality of blanks seemed adequate, and further detailed investigation would be required to evaluate effect of processing parameters (blank heating set points, shuttling time, press speed and tonnage, effect of mold surface i.e., rubber versus metal and others) on final part quality. The process yielded a high-fiber volume fraction, low-void content component and the process was used during sub-element fabrication with the designed fiber layup described in Section 6.



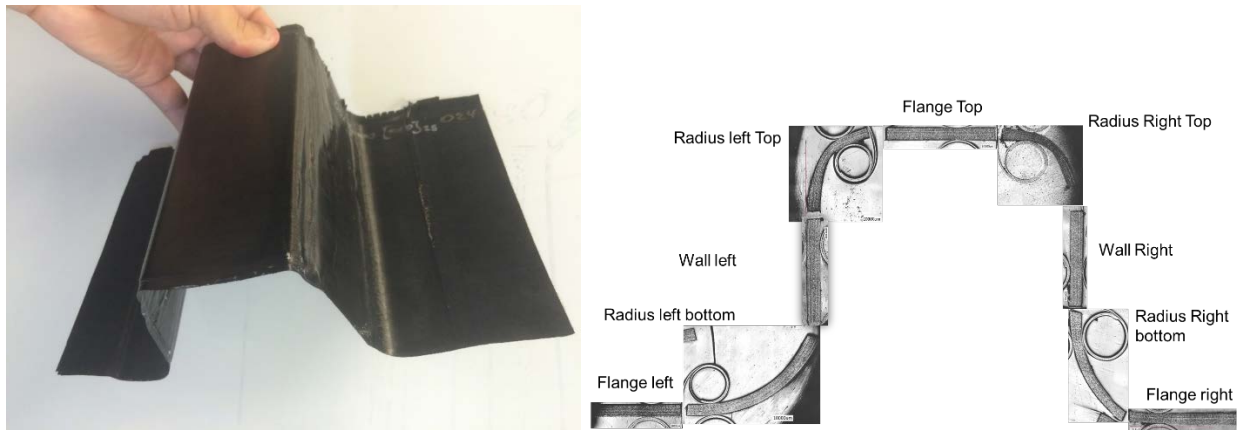
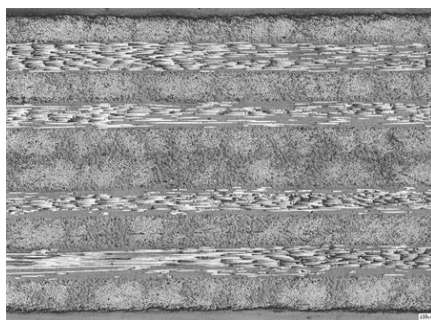
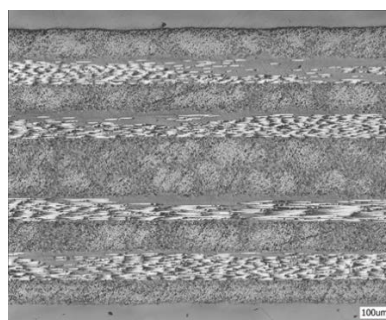


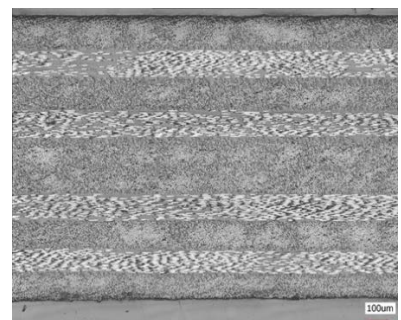
Figure 7-16. Photo of Sub-Element Specimen and Assembled Microscopic Image



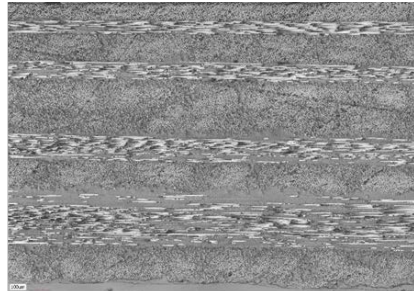
a) Flange left



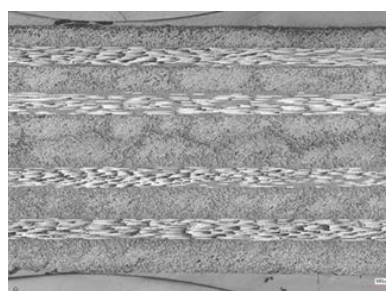
b) Radius left bottom



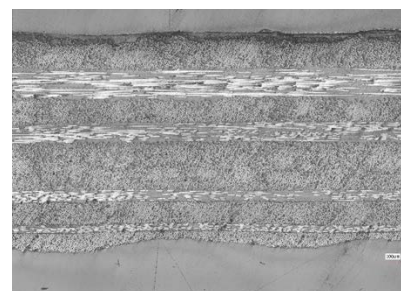
c) Wall left



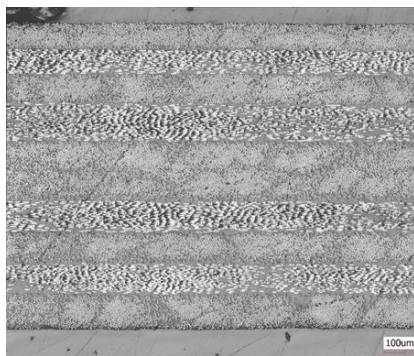
d) Radius left top



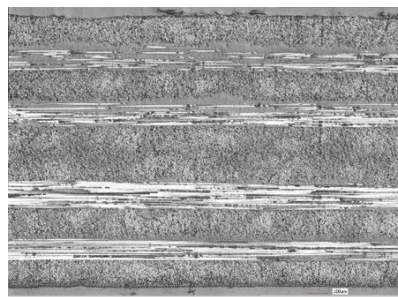
e) Flange top



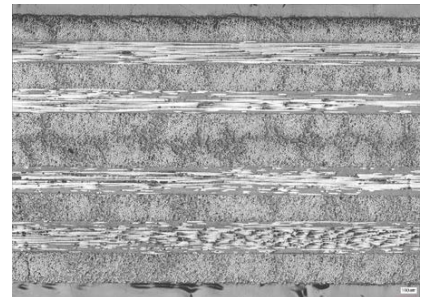
f) Radius right top



g) Wall right



h) Radius right bottom



i) Flange right

Figure 7-17. Microscopic Photos Taken from Sub-Element Hat

### 7.3.5 Hat Production

Full-scale hats were produced using the forming approach. Engineered blanks based on the design outlined in Section 7 were assembled manually (Figure 7-18). Twenty-six prepreg layers were arranged to form the blank with the majority of the off-axis plies being located on the vertical walls of the hat. The prepreg roll width was limited to about 15.25 cm (6 in.) and thus a single off-axis ply required about 10 individual pieces to be connected. Plies were manually cut using a pattern master and pieces were attached to the main body using a point welding process. The final blank was consolidated under vacuum.

The IR heating cell, shown in Figure 7-19, was extended to accommodate a larger blank but uniform heating was difficult to accomplish using the heater bank system. Heat gradient between individual heater units as well as temperature losses along the cell edges resulted in unacceptable temperature gradients of more than 10°C. The lead time to purchase a new continuous heater system did not allow the project to apply the advanced rapid radiation heating approach to fabricate the full-scale hats. Thus, the press and molds were insulated and the cavity was heated using the integrated press and external convection heaters. A blank was placed on the mold surface and the system was heated.



*Figure 7-18. Assembly of Prepreg Pieces to Form Hat Blank*



*Figure 7-19. Forming Cell for Full-Scale Hats*



Temperatures at the mold and blank surfaces were monitored and final temperature gradients were minimized.

The stamping process was initiated as temperature readings exceeded 232°C (450°F) and the press was moved upwards to form the parts in between the tools. After forming, the internal cooling of the press was turned on and the part was cooled to room-temperature and taken out of the system. A total of six parts were manufactured successfully using this approach. The first three hats produced are shown in Figure 7-20. Part thickness variation was less than 10 mm with most variation in the flanges of the part. Visual inspection showed no obvious major defects but the initial part did indicate small wrinkles near the rocker and roof area. Subsequent parts formed were produced with some material being taken out in this area to reduce the doubly-curved features and resulted in significant less wrinkles.



*Figure 7-20. Photo of First Three Hats Produced*

## 7.4 B-Pillar Assembly

As documented previously, the B-pillar consists of two sub-components – a lower spine section fabricated from T700/Elium using the infusion process, and a thermoformed AS4/Nylon-6 upper hat section. Both sub-components were bonded together using the Plexus MA530 adhesive during the assembly process to form the B-pillar and then subsequently bonded to the steel rocker prior to impact testing. The overall adhesive bonding and assembly process is documented below.

### 7.4.1 Adhesive Bonding Procedure

Initial tests to identify the appropriate adhesive system, surface preparation process and bonding time have been documented in Section 5. The final outcome of the study was to identify the Plexus MA530 system as the appropriate adhesive for all three substrates – Elium, Nylon-6 and Steel. Both thermoplastic substrates only require grit blasting of the surface, while the steel surface requires a primer (PC 120 from Plexus) after grit blasting. The final adhesive bonding cycle selected is as follows.

- 3 hours at room temperature in assembly fixture (30-45 minutes working time)
- 2 hours free standing cure at 50°C

Studies on working time and bond strength identified a maximum working time of 20 minutes prior to loss of adhesion performance. Consequently, the entire bonding process (whether spine to hat or pillar to rocker), including dispensing and assembly, must be performed within 20 minutes. Peel-and-stick dots with adhesive backing (Poron dots) were used to control bondline thickness to 60 mm.

#### 7.4.2 Hat to Spine Assembly and Bonding

The tool used to manufacture the hat in the thermoforming process also served as a jig for assembly and bonding of the hat to the spine. After both hat and spine were fabricated by their respective processes and trimmed to final shape, they were both grit-blasted using a handheld pencil blaster, with carbide grit, followed by wiping clean with cheesecloth. The pencil blaster provided a narrow and controlled spray of grit and provided excellent roughened surface for adhesive bonding. This system was previously used on bonding studies for fastening metal and composite studs and fasteners to airframe structures, and was also used in the lap-shear adhesion studies documented in Section 5. Figure 7-21 shows a photograph of a grit-blasted spine, with a similar process for the hat.

Adhesive dispensing was performed with the UD-CCM robot, using a fixed flow rate adhesive applicator integrated into the robot head (Figure 7-22). The surface treated and trimmed hat was placed in the aluminum tool for adhesive dispensing and assembly with the spine. The robot head velocity was varied to control adhesive volume dispensed at any point on the hat. RobotStudio was used to generate virtual tool paths and pre-program robot motion prior to actual dispensing trials. The Plexus MA530 adhesive was dispensed using pre-programmed tool paths and head velocity calculated based on the desired volume of adhesive at each location on the hat. Four paths were programmed – along the top, bottom and the two sides of the hat and adhesive dispensed accordingly. The overall dispensing time was approximately four minutes, well within the 20 minute requirement.



*Figure 7-21. Surface Treated (grit-blast) Spine Section Ready for Assembly*



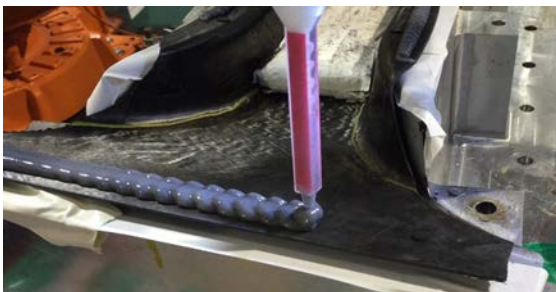


*Figure 7-22. Adhesive Dispensing with Robot Head on Hat Prior to Assembly*

Following adhesive dispensing, the spine was manually placed on the hat, with markers for alignment. Pressure was applied with weighted metal blocks along the length of the hat and proved sufficient in trials to squeeze the bondlines to the thickness of the Poron spacers. The bonded assembly was allowed to sit in the fixture at room temperature, for a minimum of 3 hours per the selected cure cycle, followed by a free standing cure in an oven at 50°C for an additional 2 hours. Excess adhesive on the exposed edges was trimmed and the completed B-pillar weighed prior to bonding to the rocker assembly. The assembled B-pillar, prior to bonding to the rocker assembly for testing is shown in Figure 7-23.



*Figure 7-23. Adhesively Bonded Hat and Spine Assembly*

### 7.4.3 B-Pillar to Rocker Assembly and Bonding

The carbon fiber thermoplastic B-pillar was then bonded to the steel rocker assembly for impact performance assessment in UD-CCM's high-energy drop tower. Design and geometric details of the rocker assembly are documented in Section 6. Figure 7-24 shows the rocker assembly with the B-pillar in position. Note that the B-pillar is not bonded yet, but positioned to show the relative locations of the overall assembly prior to impact testing. The B-pillar is bonded to the rocker location (upper steel component with hat shape) only and simply clamped in place at the roof rail location (lower steel clam-shell fixture).

Surface preparation of the steel rocker is a two-step process – grit-blasting the surface and wiping, followed by application of the PC120 primer. Primer application followed instructions provided by the supplier (Plexus), with a brush-on application followed by allowing it to air dry for 10 minutes. Figure 7-25 shows the grit-blasting process for the steel rocker, and the primed steel rocker. Surface preparation for the B-pillar surface (spine) followed spine surface preparation procedures, as documented previously.

The same adhesive (Plexus MA530) was used with a manual applicator to dispense adhesive on the primed steel rocker surface. Poron dots (60 mm thickness) were placed on the bottom of the spine. Following adhesive dispensing, the pillar was placed on top of the rocker in the overall assembly to ensure correct alignment and fit during impact testing. Pressure was applied with a heavy metal block on top of the B-pillar to ensure sufficient adhesive squeeze-out and the assembly was allowed to cure at room temperature for 3 hours, followed by a cure in an oven at 50°C (122°F) for 2 hours. The completed assembly of the B-pillar and rocker is shown in Figure 7-26.

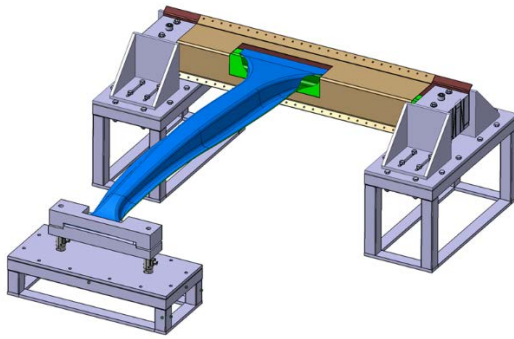


Figure 7-24. Assembled B-Pillar in Rocker Assembly and Impact Fixtures in Drop Tower

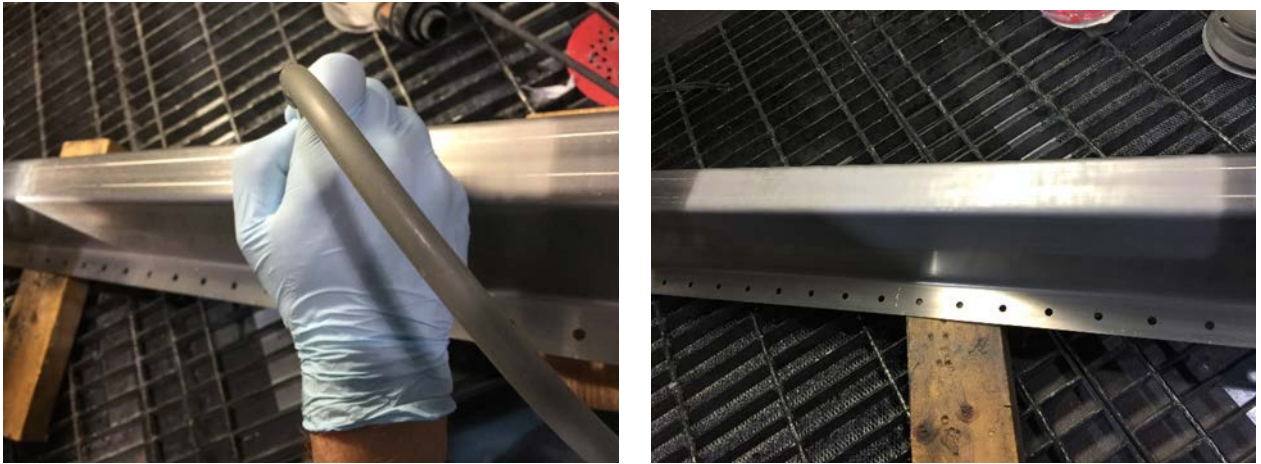


Figure 7-25. Surface Preparation of Steel Rocker



*Figure 7-26. Adhesively Bonded Assembly of B-Pillar and Rocker*



## 8. Full-Scale Testing and Simulations

The final design of composite B-pillar was been manufactured as two components, i.e., the hat and the spine following the processing method described in Section 7. The spine and hat were then bonded using Plexus 50°C cure adhesives following surface preparation and automated adhesive placement and trimming using UD-CCM's Automated Material Placement system mounted on an ABB robot (Figure 8-1a). The assembly was post-cured at 50°C in an oven. Figure 8-1b shows first three as manufactured composite B-pillars, and Table 8.1 shows the mass property comparison to the model prediction. The fabricated B-pillar was about 8 percent lighter than the modeled design. A smaller amount of adhesive was used during bonding due to a slightly smaller average gap between hat and spine. Some push-out of the carbon prepreg during forming and additional material loss occurred during routing of the final B-pillar. An approximately 60 percent weight reduction compared to the steel B-pillar was accomplished.

These composite B-pillars were impact tested using UD-CCM's Tower of Power low-velocity impact test facility following the protocols described in this section.

### 8.1 UD-CCM Tower of Power Low-Velocity Impact Testing Facility

A high-energy custom designed drop tower (called Tower of Power or TOP2000) was used to test the B-pillar sub-assembly. The TOP2000 was custom designed and built at UD-CCM as commercially available systems did not have the necessary specifications for high-energy impact testing of large structures. The tower, shown in Figure 8-2a, incorporates adjustable x-y-positioning and has been used for multi-impact (durability) testing of armor panels and joining systems as well as testing of as automotive structures. In this project, the tower was used to test the composite B-pillar sub-assemblies shown in Figure 8-2b.

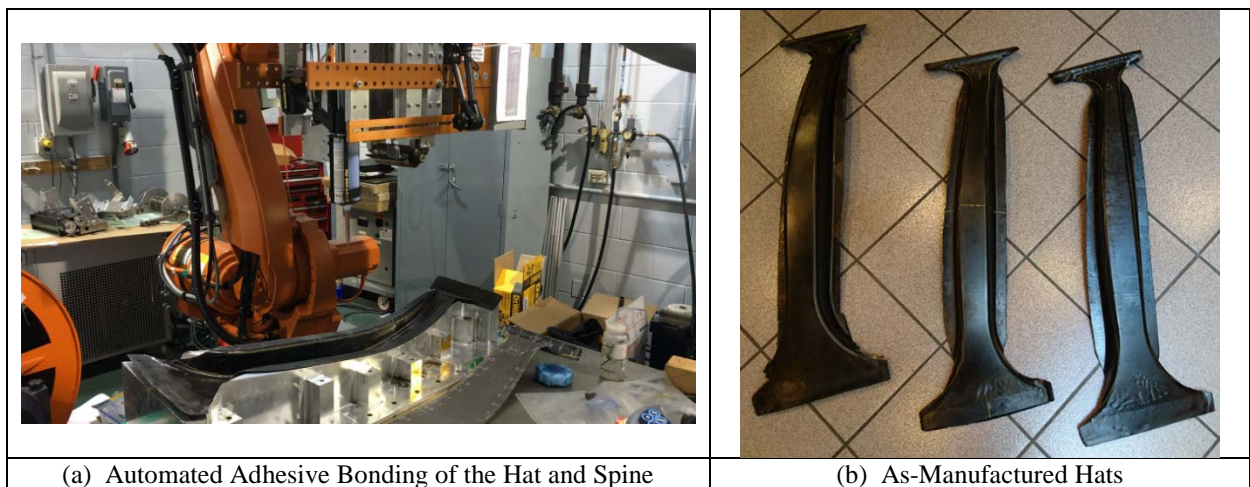


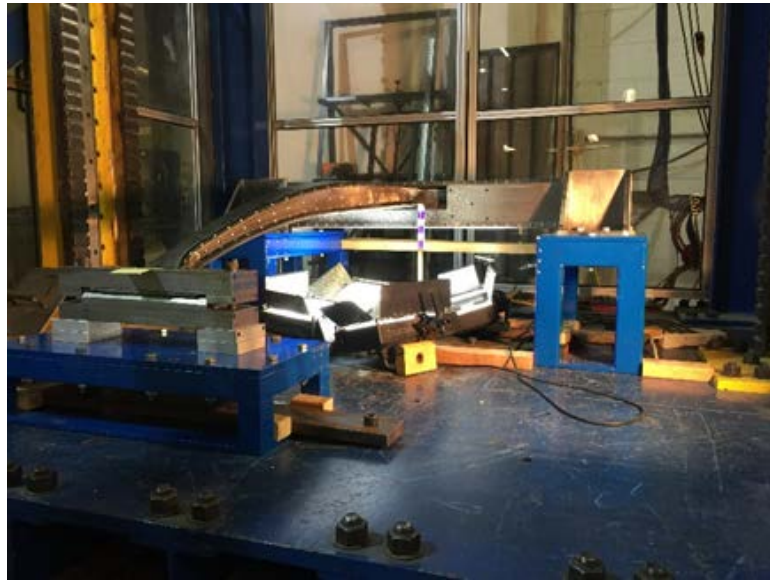
Figure 8-1. Different Views of As-Manufactured Composite B-Pillars

Table 8-1. Mass Properties of B-Pillar

B-Pillar	Mass in Pounds	Mass in Kilograms	Normalized
Steel	19.84	9.0	100%
Average CFRP Manufactured	7.54	3.42	38%
Model CFRP Prediction	8.26	3.74	41%



(a)



(b)

Figure 8-2. (a) High-Energy Drop Tower (TOP2000) and (b) Cross-Beam Showing B-Pillar Fixture Hardware Mounted in Place and Ready for Testing

The TOP2000, shown in Figure 8-2a, is approximately 6m (20 ft.) high, has an available free fall drop of 3.66 m (12 ft.) with a standard 907.2 kg impact mass and 8.6 m/s (27 fps) impact velocity giving a total available energy of 32,500J (24,000 ft-lb.). A 90,718 kg (200,000 lb.) load cell with built in accelerometer is mounted on a custom cross-beam. Four 453 kg (1,000 lb.) load cells are mounted on the top of the tower on a cross-beam attached to a Coffing 2-ton hoist to measure the static drop weight. The floor consists of 10 WF flanges sandwiched between six 3 m x 0.762 m x 25 mm (120 in. x 30 in. x 1 in.) thick steel plates that are drilled and tapped for mounting fixtures and assemblies. The tower provides a 1.88 m x 2.54 m (74 in. x 100 in.) flat open floor space available for testing. Having a hollow sandwich floor construction also allows for insertion of suspended optical and Differential Interference Contrast (DIC) image capturing and additional instrumentation for measuring forces and deflection. The drop is initiated by release of a high-energy magnet. Linear magnetic sensors mounted in the cross-beam measures location prior to testing and displacement during testing. The load cell and accelerometer mounted in the top adapter assembly measure force and acceleration data up to 100 kHz per channel on a custom built National Instruments PXI chassis mounted in a movable electronics tower. The Data Acquisition System (DAQ) is capable of recording high-speed data from 16 accelerometers, 8 load cells and also allows the capture of strain and other data recorded directly from the specimens.

The vertical motion of the cross-beam is controlled by two precision rails with eight roller bearings. The rebound is captured with two ratchet mechanisms mounted on the cross-beam that engage four vertical rails mounted on the I-beams shown in Figure 8-3a. The ratchets engage after impact and catch the cross-beam at the peak rebound height.

Digital image correlation for impact events was performed with a commercial system from Correlated Solutions, Inc. It employs proprietary software to acquire (Vic-Snap) and process (Vic-3D) stereoscopic images in 3D of any object with a suitable visual texture such as paint speckling. A full spatial calibration is first performed with the software using special calibration boards that employ a grid of dots. The analysis software then analyzes objects, motion, and

strain within the calibrated area so long as the cameras do not move. This can be performed for low-speed events in real time, or for high-speed events using a suitable high-speed camera system to acquire and store the images. A Fastcam MC2 camera system from Photron Inc. with a control and storage box is used. The camera system employs small, C-mount digital CMOS cameras and is networked via Ethernet to the computer. The cameras use Schneider 4.8 mm Cinegon compact wide-angle lenses with manual focus, allowing the optimal viewing area in the entire back surface of the impacted panel at a distance of only 0.6m (2 feet). A detailed field of view (FOV) analysis was carried out in CATIA to ensure that the B-pillar and associated hardware would be fully visible with the appropriate section of lens and offset location as shown in Figure 8-4.

The camera pair was mounted on a free-floating adjustable beam system shown in Figure 8-5a that passes through the WF sandwiched floor of the drop tower. The floating beam is mounted on a pair of adjustable lifts that are attached through a series of rubber washers to further minimize vibration during impact. The floating beam can be adjusted both vertically and horizontally for accurate positioning prior to testing.

The cameras were placed 20.3 cm (8 in.) apart to allow for stereoscopic imaging, and were aimed through a viewport in the floor of the drop tower under the panel fixture to focus on the spine directly under the line of action of the impactor. The system was armed before the impact event and is manually triggered at the moment of impact, recording several seconds of images before and after the event at the rate of 1,000 frames per second.

Image analysis subsequent to the test was performed in the Correlated Solutions software on the image pairs containing the event. The Vic-Snap software is designed to interface with several popular types of camera systems including the Photron system so that separate software normally used to control it is not required. Once the acquired images are loaded into the Vic-3D environment, a variety of analyses can be performed and displayed, such as displacement, both in and out of plane, and any type of strain reduction. Data can be output numerically for points and lines of interest, and the entire acquired area can be displayed visually in either 2D or 3D visualizations using color contour maps with many display options. The high precision with this non-contact system allows for sub-millimeter and low microstrain measurements even at long distances. All impacts and the deflection fields caused in the panel test were characterized in this way.



Figure 8-3. (a) Ratchet Catch Mechanism and (b) Vertical Ratchet Rails Mounted on Guide Beams



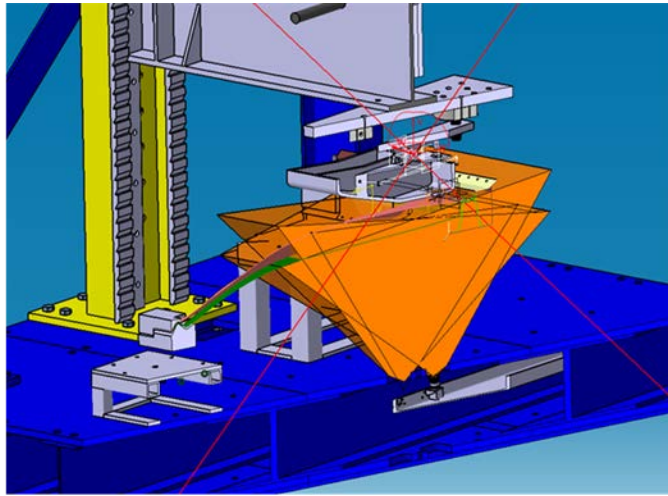
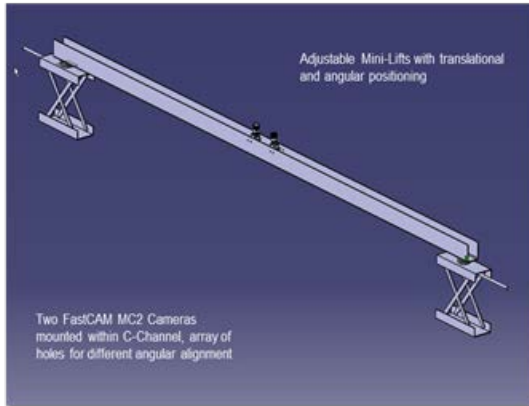


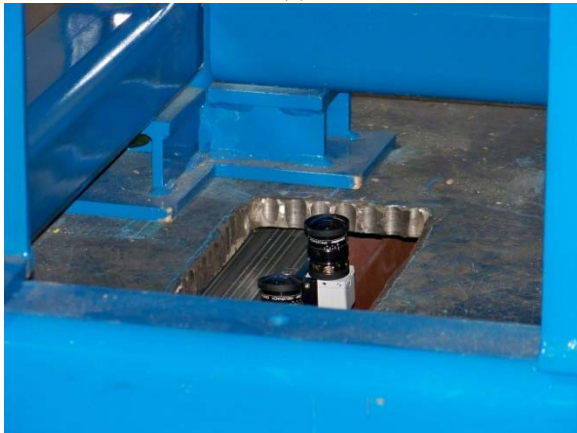
Figure 8-4. FOV Modeling in CATIA for B-Pillar Impact Test to Confirm View Area



(a)



(b)



(c)



(d)

Figure 8-5. (a) Floating Beam With Camera Mounting, (b) FOV for DIC System, (c) Opening for Camera, and (d) Floating Platform Within Floor of TOP2000

The TOP2000 electrical control system is built around a National Instruments NI PXI-1042 8-Slot chassis connected to a DELL R5400 using a NI PXIe-PCIe8371 x4 MXI-Express for PXI Express connection. PXI units include a NI PXI-6251 (16 Analog Inputs, 24 Digital I/O, 2 Analog Outputs) and a NI PXI-4496 (24-bit, 204.8 kS/s, 16 Input, 2 Gain, TEDS, AC-Coupled). A BNC-2144 rack unit is attached to the 4496 unit and a SCC-68 I/O Connector is attached to the 6251 unit. An additional PXI-6251 unit is installed internally within the R5400 for added digital and analog I/O, and the entire system is mounted within a 42U Server Rack.

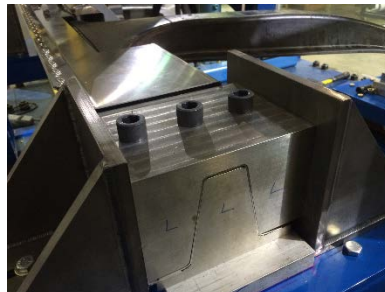
A custom build graphical user interface was developed in LabVIEW to control all elements of the impact tower as well as acquire and save data synchronously from all input channels. The software interface is built with a number of redundant controls that ensure all channels are active with correct input voltages, data saving is active and safety systems are in check. The data acquisition system records impact data in a burst mode at 100 kHz from each channel and post processed as needed. The raw and filtered synchronized data can be cropped and saved to a standard spreadsheet format. Data recorded includes impact force, acceleration and striker displacement. Also saved is filtered data (Butterworth filter) as well as up to 4 channels of strain gage data if required. Additional strain and acceleration channels are available for more complex testing and assemblies.

## 8.2 Experimental Setup for Impact Testing of Composite B-Pillars

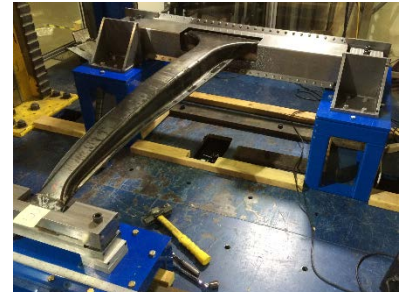
An impact test fixture was designed and built to test the composite B-pillars under side-impact crash conditions similar to the B-pillar side-impact simulations of the vehicle sub-component. The impact test fixture consisted of three components, i.e., (i) consumable steel rocker assembly and end clamps, (ii) clamps for the composite B-pillar at the roof, and (iii) the impactor assembly. Figure 8-6 shows different component of the impact test fixture for composite B-pillar.



(a) Consumable Steel Rocker Assembly



(b) Clamp at the end of the Rocker



(c) Clamps at Roof Location



(d) Illumination for the DIC



(e) Speckle Pattern for DIC



(f) The Impactor Assembly

Figure 8-6. TOP Impact Test Fixture for Testing Composite B-Pillar

TOP Drop Height  $h_1 = 26924 - mm = 106 - inches$ , TOP Drop Mass  $m_p = 1265 - lbs = 568.80 - kg$ , TOP Impact Velocity  $V_1 = 23.82 - ft/sec = 7.26 - m/s$ , TOP Impact Energy  $E_1 = 15.02 - kJ$

The composite B-pillar was adhesively bonded to the steel rocker hat-section and cured using the Plexus adhesive and primer prior to the rocker assembly. Once the rocker box assembly was complete, the composite B-pillar was then clamped at the rocker end clamps, and at the roof clamps. The high-speed DIC cameras and high-speed digital camera were set in their respected positions and the composite B-pillar was ready to be tested under TOP impact.

The impactor assembly consisted of a pin joint between the impact box and the dead weight of the TOP drop-beam (Figure 8-6f). The pin joint allows the rotation of the impact box by about 8-degrees to mimic the impact box rotation observed in the baseline metal B-pillar side-impact simulation. Hard stops are added at both the rocking ends such that the rotation of the impact box could be stopped after 8-degrees of rotation. The total mass of the drop-beam-impact-box assembly was measured to be  $m_p = 568.80kg$  (1265lbs). Given the maximum drop height of  $h_I = 2.6924m$  (106 inches) of the drop tower, this combination of this drop height and drop mass provided an impact velocity of  $V_I = 7.26m/s$  and an impact energy of  $E_I = 15.02kJ$ . This level was very close to the impact energy of the baseline metal B-pillar side-impact simulations (15.20 kJ).

### 8.3 TOP-LVI Experimental Results

Five composite B-pillars designated by B1 to B5 were impact tested with identical impact conditions, i.e.,  $h_I = 2.6924m$ ,  $m_p = 568.80kg$ ,  $V_I = 7.26m/s$ , and  $E_I = 15.02kJ$ . Figure 8-7 shows time history of impact contact forces for all five experiments done. Investigating the high-speed photography of the first test (TOP-LVI on B-pillar B1) revealed that the roof clamp fixture, although firmly bolted to the floor, slid inward towards the rocker during impact. This was not an ideal boundary condition and for this reason additional measures were taken such that the roof clamp fixture cannot move (spacer plates were added to prevent sliding). The inadequate boundary conditions in the first test resulted in additional compliance, longer duration impulse loading and a reduction in the peak load as shown in Figure 8-7. All other instrumentation was proven out in this initial test.

After the second impact test on B2, post-impact inspection of the rocker clamps revealed that the two 12.5 mm bolts used to clamp the rocker end were plastically deformed and the rocker end clamp rotated approximately 10-degrees. This additional compliance also had the slight effect of reducing peak loads. The rocker clamps were modified to accommodate three 17.5 mm diameter bolts of high-strength steel and the base of the clamp was strengthened to prevent any rotation of the rocker ends (Figure 8-6b). All remaining TOP-LVI experiments were conducted with these improved boundary conditions and were found to be quite repeatable as shown in the figure. This configuration was very close to the boundary conditions used in the modeling of these experiments.

Experiments B2 to B5 showed consistent results while Experiment B3 provided the highest resistance force. Figure 8-8 shows the snapshots of the deformation sequence of the composite B-pillar B3 at four different time, i.e., at 0 ms, 30 ms, 60 ms, and 90 ms. These snapshots clearly demonstrate the crushing of the hat under the impactor, and S-shaped deformation of the spine-hat assembly. Further comments on the damage modes of the B-pillar is presented later.



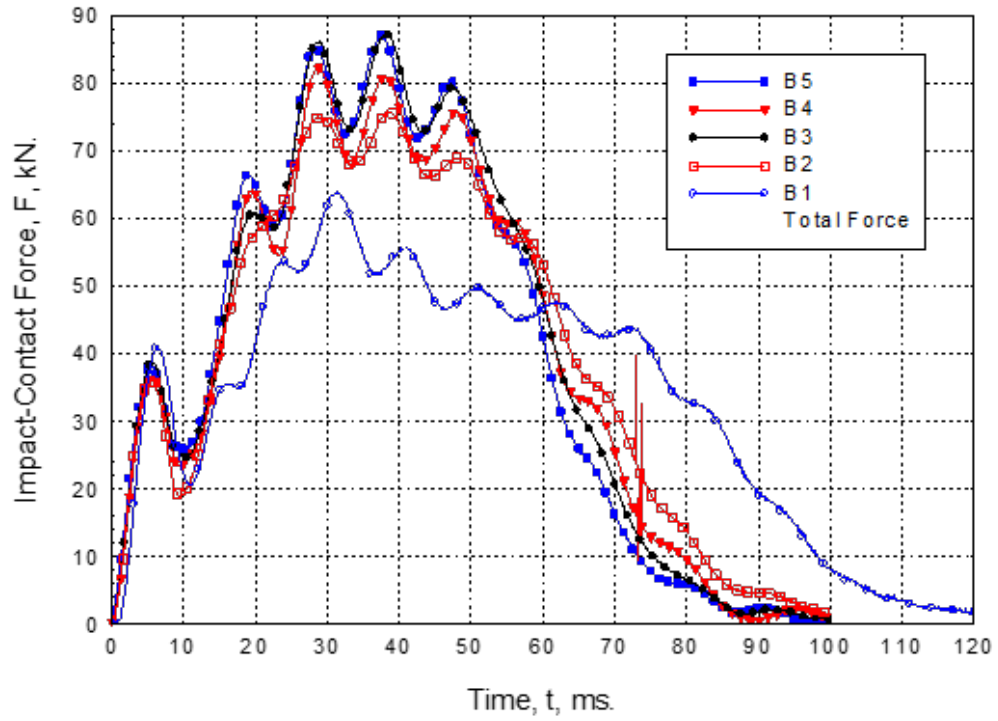


Figure 8-7. Time History of Impact-Contact Force

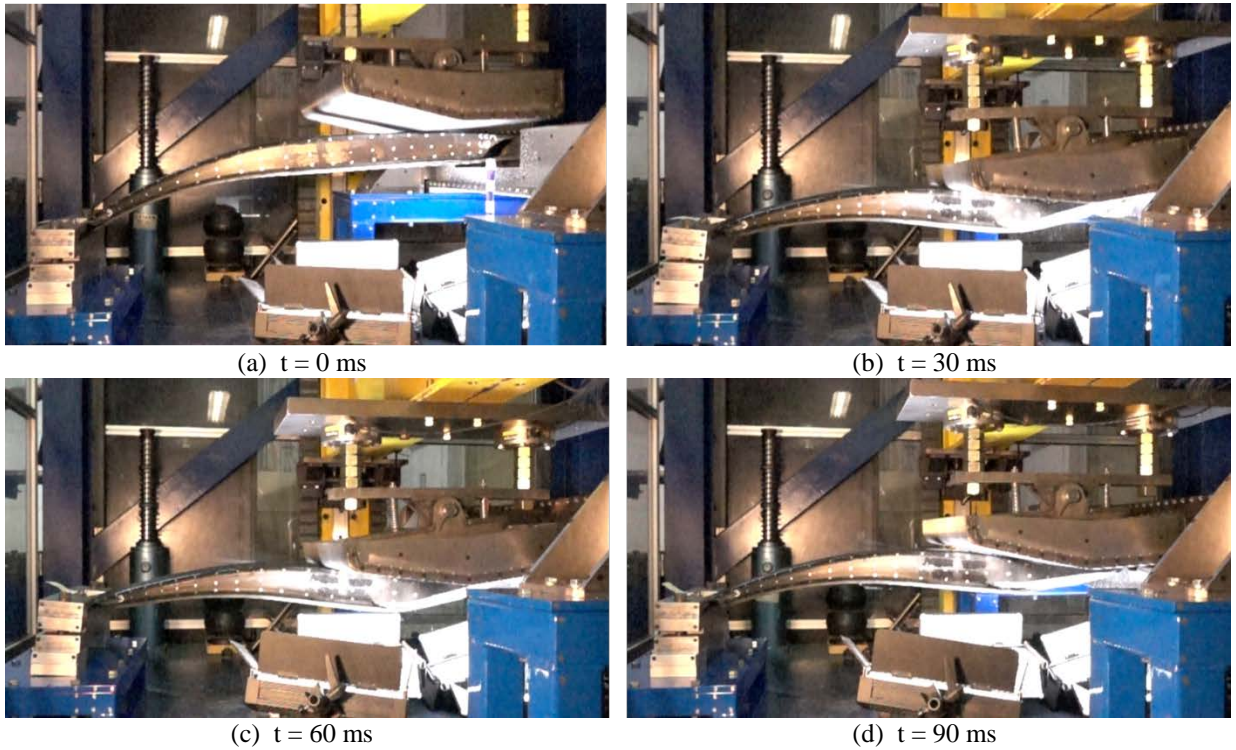


Figure 8-8. Snapshots of Deformation of Composite B-Pillar Under TOP-LVI Loading

Typical experimental data of composite B-pillar B3 is presented next.

### 8.3.1 TOP-LVI Experimental Results of Composite B-Pillar B3

Figure 8-9 shows the typical LVI experimental results of the composite B-pillar B3. The composite B-pillar was recovered after the TOP-LVI experiment (Figure 8-9a) for post-impact damage evaluation. Time history of the impact contact force was measured with two load cells and added to get the total impact contact force (Figure 8-9c). The time averaged force in the time range 25-45 ms was found to be 80 kN (with a peak force of 86kN). The load was split approximately one-third at the roof and two-thirds at the rocker support based on the impact location. DIC data was used to compute the displacement of the spine along its axis at different points in time (Figure 8-9d). Dynamic deformation of the spine in the time range 0-15 ms shows a smooth profile, however shows a kink at location 325 mm from the rocker in the time range 20-50 ms. At this time, the hat had undergone significant crushing (Figure 8-8) and lost section modulus such that the spine was carrying more of the transverse load and associated bending. The spine displacement reached its peak value of 173 mm at time 50 ms (as discussed below a significant portion of this displacement was plastic deformation of the steel rocker). From the DIC data, surface axial strain along the spine central axis was also computed. Figure 8-9b shows the axial surface strain distribution at the time of maximum displacement of the spine that ranged from -1.2 percent to 0.6 percent (strains at the edge of the speckle pattern were not considered accurate). This force time history, and the axial mapping of spine displacements will be compared further in Section 8.4.2.

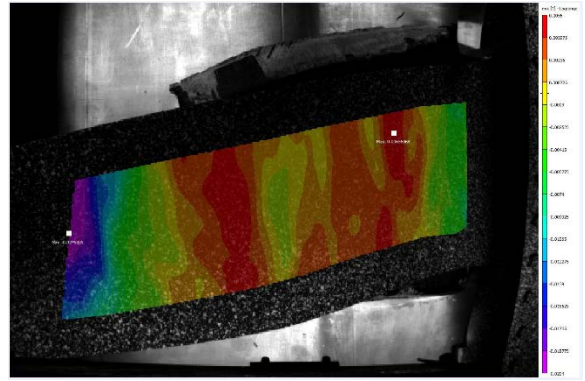
### 8.3.2 Post-Impact Damage Analysis of Composite B-Pillar B3

The composite B-pillar with the rocker box-beam assembly (Figure 8-9a) was recovered from the TOP-LVI experimental setup, the composite B-pillar was first inspected for visual damage and then removed from the rocker beam. The deformed rocker box-beam assembly was scanned with a handheld laser scanner in 3D. The cloud data of the scan was used to construct the surface of the impacted structure. Figure 8-10 shows the surface plot of the deformed rocker box-beam assembly. The original un-deformed geometry was superimposed of the deformed data and maximum vertical plastic deformation of the rocker box-beam assembly was determined to be 72 mm.

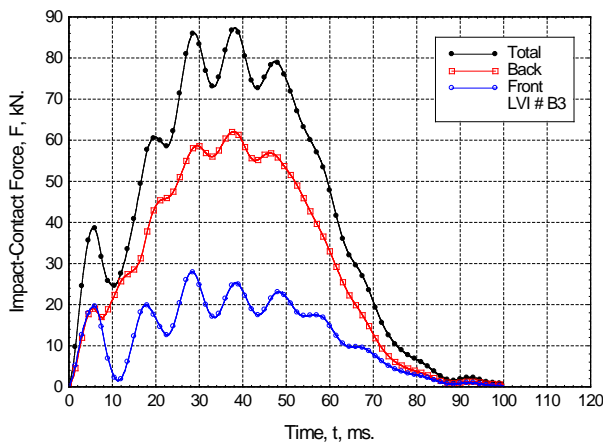
Different damage mechanisms within the composite B-pillar are presented in Figure 8-11. These damage mechanisms included (i) crush damage of the hat and associated fracture of the web (sidewall), (ii) damage of the hat at the rocker root during crush, (iii) failure of the spine and hat joint at the impact and crush location, and (iv) delamination of the spine at the rocker-spine adhesive joint. The first three damage modes (i-iii) were predicted and integral to the energy absorption design capabilities of the composite B-pillar design. The spine to metal rocker adhesive joint was designed to withstand the impact induced shear and peel loads using mixed-mode cohesive traction laws measured on test coupons. Inspection of both joints showed that joints did not fail within the adhesive bondline indicating outstanding adhesion and toughness of the pretreatment and Plexus adhesive between dissimilar materials (nylon to acrylic and acrylic to steel). Failure of the joints in the crush zone and at the rocker occurred cohesively in the first few layers of the spine.



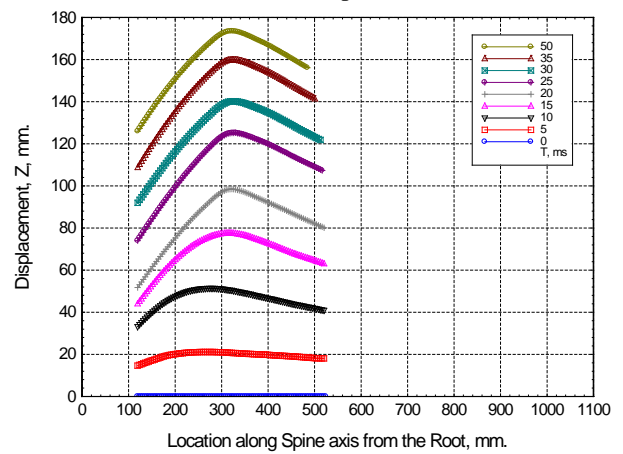
(a) Post-LVI Deformation and Damage



(b) DIC Image of Strain Axial Distribution on Spine at max. Deflection. Violet-Compression, Red-Tension

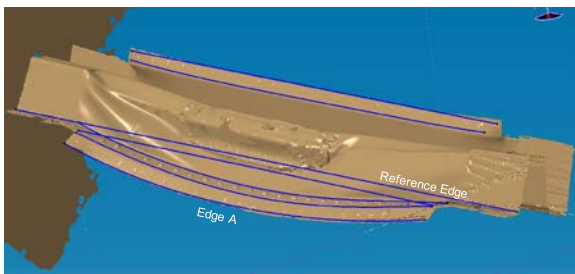


(c) Time History of Contact Force. Average Peak Force = 80 kN in the Time Range 25 ms to 45 ms.

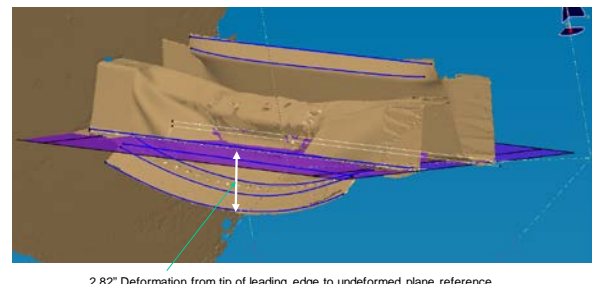


(d) Dynamic Displacement of the Spine at Different Time (from DIC)

Figure 8-9. TOP-LVI Experimental Results of Composite B-Pillar B3



(a) 3D Laser Scan of the Rocker Box of TOP-LVI Experiment # B3.

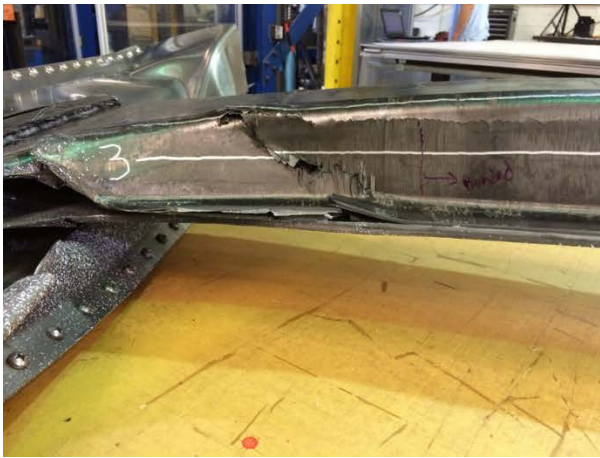


2.82" Deformation from tip of leading edge to undeformed plane reference

(b) Plastic Deformation of the Rocker Box. Max. Displacement = 2.82 inches = 71.63 mm.

Figure 8-10. Plastic Deformation of Rocker Box Assembly of Composite B-Pillar B3





(a) Hat Crush and associated Web Fracture



(b) Damage at the Hat Root



(c) Failure of the Hat and Spine Joint Region in the Crush Zone



(d) Delamination of the Spine at the Rocker-Spine Adhesive Joint

*Figure 8-11. Different Damage Mechanisms of Composite B-Pillar B3*

These damage mechanisms will further be discussed in the TOP-LVI simulations presented in the next section.

## 8.4 Simulation of Full-Scale Full Energy Impact Experiments on Composite B-Pillars

### 8.4.1 FE Model of TOP-LVI Experiment

A FE model of the TOP-LVI experiment was developed from the CATIA solid model for LS-DYNA simulations. Solid elements were used to model the impactor assembly, roof clamp, and rocker clamps. Shell elements were used to model the composites and sheet metal rocker components. The adhesive bondline (1.5 mm thickness) was modeled with solid elements where congruent node-merged solid elements were mapped between two adhering surfaces. This approach improved the computational accuracy and stability of the simulation by eliminating tied contacts between solid adhesive and adhering non-congruent shell meshes.

Figure 8-12 shows different parts of the FE model of the TOP-LVI experiment. The impactor assembly (Figure 8-12a) consisted of an impact beam with flanges for the journal bearing or pin to connect to the lower impact box. The impact box can rotate 8-degrees in both the



clockwise and anti-clockwise directions. Two cylinders were used to restrict the motion of the impact box. The upper impact beam can only move in the vertical direction (y-direction in the FE model) and all other movements are restricted. All contacting parts at the pin location were in a single surface contact such that the impact box can rotate around the hinge/pin. The total mass of the impactor except the impact box is distributed on the remaining parts of the impactor assembly by increasing the density of the material. The entire impactor assembly was assigned an initial velocity equal to the impact velocity corresponding to the impact height of the experiments.

Figure 8-12b shows the clamps used to clamp the roof end of the B-pillar. An automatic surface to surface contact was defined between the roof clamps and the composite hat and spine, while the motion of the roof clamp top and bottom was restricted in all directions.

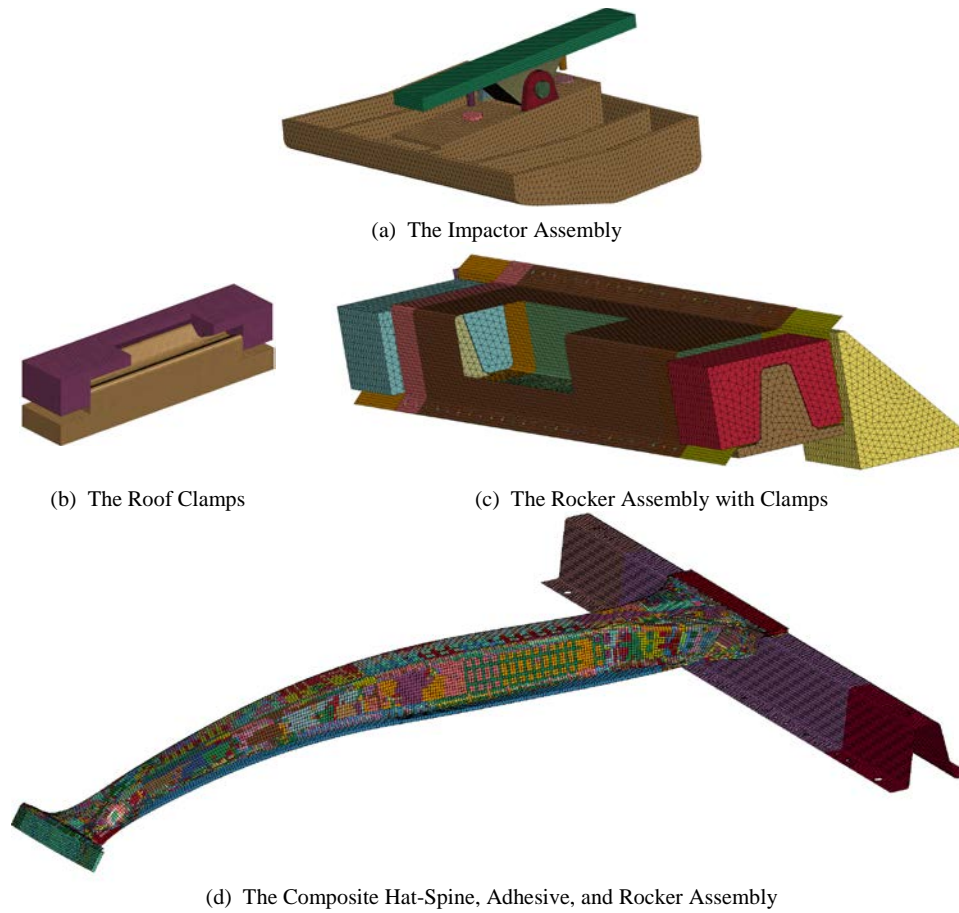
Figure 8-12c shows the rocker box assembly without the central rocker hat-beam. The rocker box and hat-beam were clamped at the edges by contact with friction and constraining all motions of the clamping solid blocks.

Figure 8-12d shows the composite hat and spine bonded with solid adhesives and the spine was bonded to the rocker beam at the root. A single surface contact was defined between the hat, spine, the impact box, the rocker box and the rocker beam.

The entire model was run in a Linux cluster using 96 cores and the problem was solved for 100 ms in 10 hours and 10 minutes. Results obtained from this model are presented next and compared with the experimental results to assess the accuracy of the model.

The material model used to model the steel rocker box and beam is \*MAT\_SIMPLIFIED\_JOHNSON\_AND\_COOK. The yield stress (A) and plateau stress (A+B) parameters suggested by BMW for the European steel specification is  $A = 390$  MPa and  $B = 410$  MPa. Because the material for the rocker was not readily available, an equivalent steel was identified by BMW and was procured from a local source. Since all other properties in this project were measured the yield stress of the steel was measured from coupons machined from the rocker box and beam. Figure 8-13 shows the stress-displacement output of the test for two material thickness, i.e., 2.6 mm and 1.5 mm. The yield stress of both these materials were found to be significantly lower than those provided by BMW. The JC parameters used in the present simulation are  $A = 273$  MPa and  $B = 10$  MPa.

The parameters for steel predicted a maximum permanent deformation of the steel in the TOP-LVI experiment B3 of approximately 60 mm that is slightly lower than the experimental measurement at the same location (72 mm).



(d) The Composite Hat-Spine, Adhesive, and Rocker Assembly  
*Figure 8-12. FE Model of the TOP-LVI Experiment*

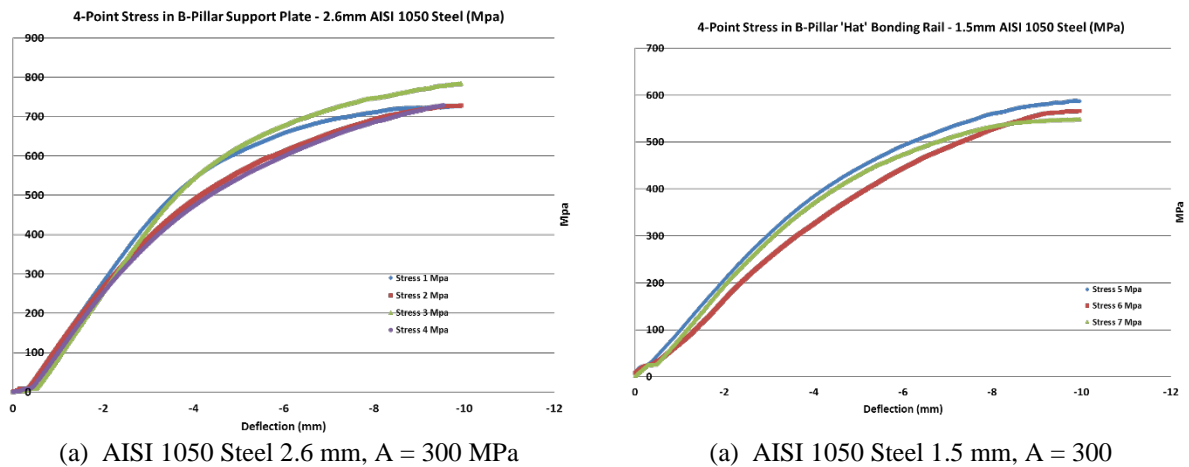


*Figure 8-13. Four-Point Bend Test Results of As-Received AISI 1050 Steel*

In the experiments, delamination of the joint was observed as predicted in the crush zone immediately under the impactor between the carbon/nylon hat and the carbon/acrylic spine. This joint separation was accurately predicted using the cohesive traction laws measured from adhesively bonded Mode I and Mode II coupon tests. The joint separation starts at the location where the hat and spine are first bonded and extends to the end of the impactor. The effects of this debonding on dynamic deflection of the B-pillar were included in the simulations. As discussed below this level of debonding between the hat and spine in the crush zone exceeded the level predicted in the vehicle sub-component configuration. One possible reason was that

the steel rocker support in the vehicle sub-component configuration underwent significantly less deformation than in the experimental setup resulting in less severe loading of the bondline (and less debonding).

Delamination failure mode in the spine near the rocker-spine adhesive joint was observed. One approach to study the effect of this failure mode on dynamic deflection was to reduce the traction and fracture toughness of the adhesive traction law between the spine and the metal rocker beam to mimic the delamination in the spine. An alternate approach would be to use multiple shells or 3D elements (layer by layer) in the joint to predict these cohesive/interlaminar joint failure modes. As will be shown below, excellent correlation has been achieved over the entire duration of the impact that implies that this failure mode did not contribute significantly to the overall response of the B-pillar.

## 8.4.2 Results and Discussion on TOP-LVI Simulations

Snapshots of the impact event are presented in Figure 8-14 at different times. The hat was found to crush under the impactor, the impact box rotated and stopped at 8-degrees of rotation (around 30 ms) and the hat-spine assembly underwent large deformation achieving maximum displacement (around 50-60 ms) before rebounding. Snapshots and animation from the simulations were compared with the snapshots and animations shot during the experiments and good correlations between the simulation and experiments were observed. During the experiment, the adhesive joint between the hat and spine failed under the impact box, and was accurately predicted in the simulation of this experiment. The adhesive bonding at the root between the spine and the steel rocker beam was subjected to significant peel and shear loads during impact inducing significant plastic deformation in the steel without joint failure. The modeling approach using 3D adhesive elements with mixed mode traction laws derived from independent adhesively bonded coupons was effective. However, the delamination of the spine cannot be modeled accurately with shell elements that did not accurately predict interlaminar stress and the associated interlaminar failure modes. Future work should consider the use of multiple shells that include cohesive surfaces to model the composite or MAT162 solid elements can be used that models delamination without the need for cohesive elements. The computational expense of a full 3D layer by layer model may require hybrid approaches where laminated shells and 3D elements are combined in an optimal manner. An alternative approach would be the characterization of the overall strength of the bonding region. These properties would then be incorporated into the cohesive elements. This approach has shown good correlation in BMW series production vehicles and does not affect model performance.

Figure 8-15 shows the time history of the impact contact force and impactor displacements (measured at the impactor hinge/pin) from the simulation and is also compared with the data experimentally measured by DIC from the experiments for the TOP-LVI B3. The total impact contact force (Figure 8-15a) matched reasonably well with a slight time offset of the peak location and a faster unloading rate. Time history of the impactor hinge/pin RBD in Figure 8-15b shows that the peak RBD of the hinge/pin was about 50 mm less than that of the B3 experiment.

Reviewing the movie of the B3 impact and the movie obtained from the simulation revealed that the crush of the hat was less in the simulation than it had been observed in the experiment. This difference was the most probable explanation for the slight differences presented in Figure 8-15. Further quantitative analysis is presented below.

Force and RBD of the pin was plotted in Figure 8-16 by eliminating the time axis, which showed that the experimental displacement was  $\Delta_{PIN} = 50\text{mm}$  larger than simulation. If the crush of the hat was less in the simulation than the experiment, this behavior of the force-displacement was expected. To determine the actual degree of hat crush, the deformation of the spine below the crush zone was determined from both the simulation and the DIC experimental measurements.

The deformed shape of the spine along the spine centerline from simulation at different time is presented in Figure 8-17a, where maximum deformation was observed at 50 ms. Dynamic displacement of the spine (with respect to shape of the spine at  $t=0$ ) is presented in Figure 8-17b along with the experimental values using the location of peak displacements at time  $t = 50\text{ ms}$  as the reference. Dynamic displacement profiled showed a very good correlation between the experiment and simulation where the peak displacement of about  $\delta_{Spine} = 175\text{mm}$  was observed at time  $t = 50\text{ ms}$ . Based on these spine results, the simulation has been experimentally validated with respect to occupant intrusion safety.

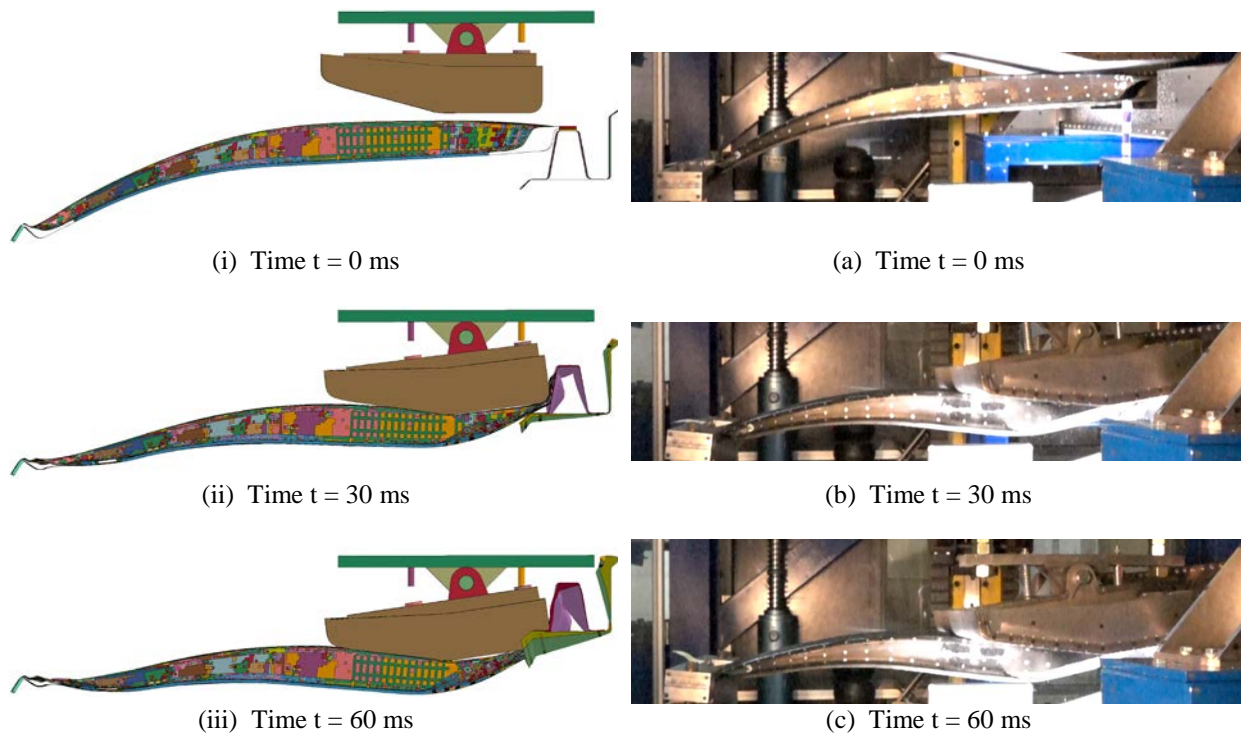
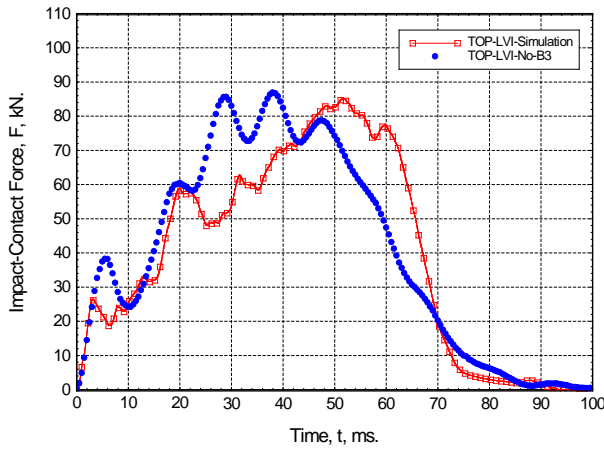
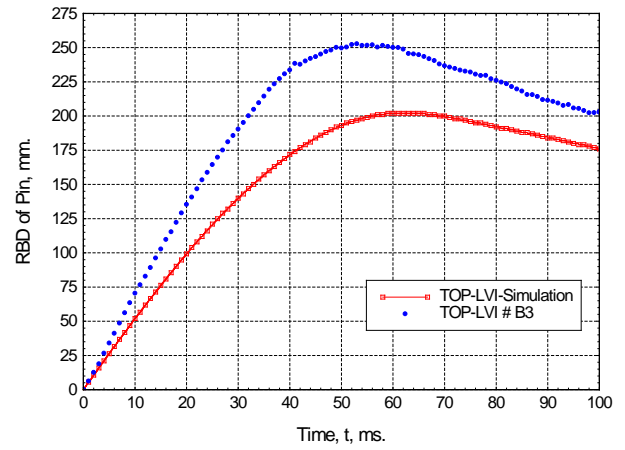


Figure 8-14. Snapshots of Composite B-Pillar Deformation at Different Times



(a) Force vs. Time



(b) Pin Displacement vs. Time

Figure 8-15. Time History of Impact-Contact Force and RBD of Impactor Pin Comparison between the simulation and experiments

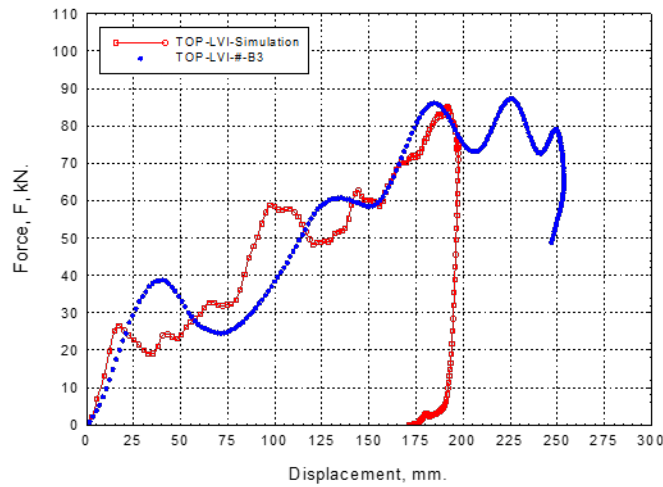
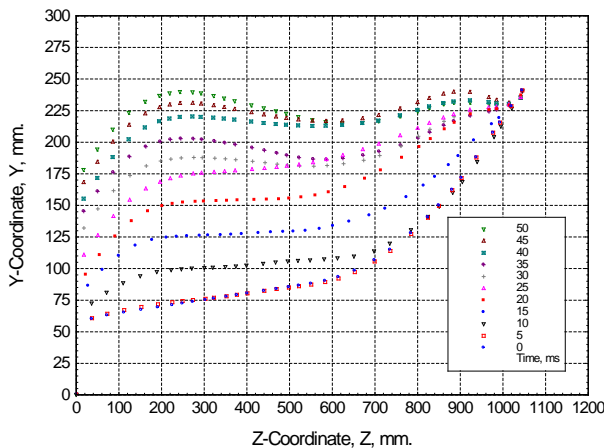
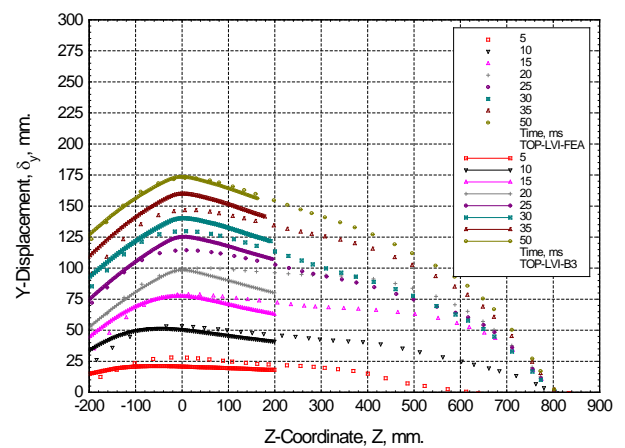


Figure 8-16. Impact-Contact Force versus RBD Simulation and Experiment B3



(a) Dynamic Deformation



(b) Shifted Dynamic Displacement

Figure 8-17. Dynamic Deformation and Displacement of Spine Centerline Simulation and Experiment B3

If one now considers the displacement of the hat and the spine versus time, the difference corresponds to the degree of hat crushing. In the case of the experiment the degree of crush was 75 mm (see Figures 8-15b and 8-17b) that was near 100 percent collapse of the initial hat height and consistent with the high-speed video. The simulation predicts 25 mm of crush. Reasonably good agreement of hat crushing during the quasi-static sub-component test was achieved. Additional study at the sub-component level under dynamic loading is recommended to improve the understanding of the material and improve simulation predictions. It is very interesting to note that the B-pillar that has undergone 100 percent collapse has tremendous ductility with elastic recovery to the original shape after unloading. This design using carbon thermoplastic composites has inherent robustness and significant strength retention with the ability to carry the impactor weight after impact testing.

It was also desirable to compare the results from the simulation/experimental setup to the vehicle side-impact of the metal baseline and associated occupant intrusion requirements. Recall there were five stages of vehicle modeling as shown in Figure 8-18. The first stage was the full vehicle model with the crushable barrier system. This model was reduced in complexity to a Stage 2 model with an equivalent crushable barrier system. The Stage 3 model was further simplified to just the side of the car with the rest of the vehicle mass placed at the centroid to retain correct momentum and energy transfer during side-impact. Stage 4 was further simplified by removing the doors and hinges and the crushable barrier was replaced with a contoured rigid impactor that rotated. This showed that a similar degree of deformation and a similar amount of energy absorption could be achieved in the B-pillar while removing the doors from the model. This was done to improve model complexity and generate a manufacturable test condition. Crushing of the doors did show a 5 ms delay existed between initial contact with the doors and the onset of dynamic loading of the B-pillar. This delay was factored into the correlations.

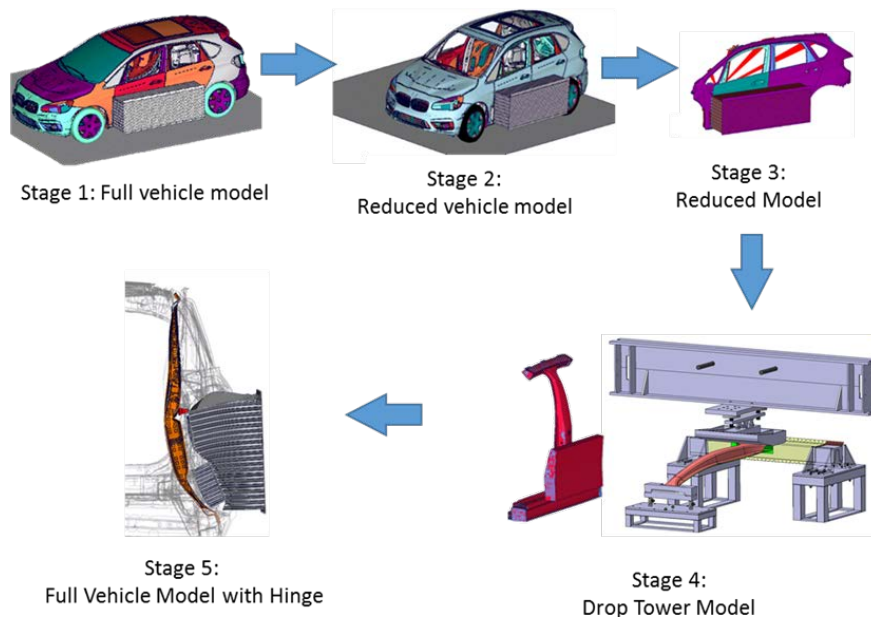


Figure 8-18. Various Stages of Vehicle Models Used to Predict Occupant Intrusion



The basis for these stage simplifications was to ensure that the dynamic deflection at time of air bag deployment and maximum deflection were equivalent. All of these stages included the metallic B-pillar baseline. Stage 4 without doors and hinges was defined as the baseline configuration for design of the composite B-pillar.

Stage 4 also became the basis for developing the experimental fixturing for high-speed crash studies. The boundary conditions and the grade of steel used in the low velocity impact experiment differ from the Stage 4 vehicle configuration. The approach was to model the experiment to validate the model of occupant intrusion based on the experimental measurements of the spine dynamic deflection. As a second step, the level of plastic deformation in the experiments was adjusted to account for the higher yield strength steels used in the Stage 4 vehicle configuration. This allowed direct comparison of the experimental measurements to the occupant intrusion limits established for the metallic baseline. Based on Stage 4 results, the experiments and models were found to be in good agreement and meet the occupant intrusion requirements of the metal Stage 4 baseline. Details are provided next.

One of the major differences was the degree of plastic deformation of the steel rocker originating from the different boundary/clamping conditions and the lower yield strength steel used in the experiments. Figure 8-19 shows the total simulated dynamic displacement of the spine at different points on the B-pillar centerline where the individual displacements were maximum. Recall that the total experimental displacement (175 mm) was the sum of the B-pillar and the steel rocker displacements. In the case of the experiment, the measured plastic deformation was 72 mm (the simulation of this experiment with the lower measured yield strength was 60 mm). However, in the Stage 4 model, the plastic deformation of the rocker was constrained by a rigid beam. Consequently, the plastic deformation of the rocker was subtracted from the experimental value that showed the maximum deformation of the composite B-pillar to be 115 mm. The permanent displacement of the rocker in the simulation of the metal baseline having slightly stiffer rocker configuration and much higher yield strength was only 17 mm. Consequently, the metal B-pillar rocker support structure deflects 43-55 mm less than the experimental composite B-pillar rocker setup when impacted under the same conditions. To adjust the total displacement of the experiments to approximate the response of the composite B-pillar with the vehicle metal rocker support, one would simply add deformation of the steel support structure. In the case of B3, this would give an adjusted maximum total deflection between 120-132 mm in the vehicle sub-component configuration.

Based on these estimates, the vehicle intrusion requirements at certain crucial points in time given in Figure 3-2 (Section 3) can now be compared to the composite B-pillar response in both the vehicle sub-component and experimental configurations. Intrusion displacements were defined on the interior surface of the B-pillars. In the case of the composite B-pillar the results were taken from the spine that has been shown above to be accurately predicted by the model. The key results are given in Figure 8-20 and compared to the metal baseline. Overall the composite B-pillar in the vehicle sub-component configuration was predicted to be lower than the metal baseline for all times. In the case of the results from the experimental setup, the composite B-pillar was experimentally shown to be lower than the metal baseline requirements at the lower impact times of 9, 11 and 14 ms where the degree of rocker deformation was largely elastic and exhibit equivalent response as shown in Figure 8-19 for both configurations. At the time of peak displacement (approximately 60 ms), the experimental displacement of the composite B-pillar was adjusted for excessive plastic deformation of the rocker (explained above) was equivalent to the metal baseline. In contrast to the lower times, the experimental results were measured to be higher than the vehicle sub-component model of the composite at peak displacement. This difference was due to the fact that the experimental setup subjects

the composite B-pillar to higher displacements (total displacement of 175 mm) that resulted in the debonding (as predicted) of the hat and stiffener within the crush zone. In the vehicle configuration, minimal debonding was predicted.

Based on the results given in Figure 8-19, the composite B-pillar response in the vehicle sub-component configuration satisfies all of the intrusion safety requirements based on Stage 4 configuration. In addition, all composite B-pillars exhibited rebound and post-impact structural integrity in terms of fully supporting the impactor dead weight of 568.80 kg.

Stage 5 in Figure 8-18 places the composite B-pillar back into the full vehicle simulation including the doors and hinges.

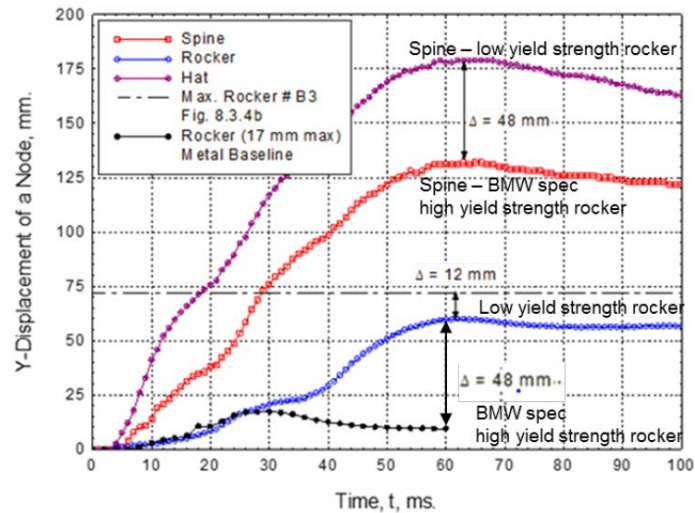


Figure 8-19. Time History of Dynamic Displacement on Centerline of B-Pillar at a Point Location of Maximum Dynamic Displacement of Individual Components

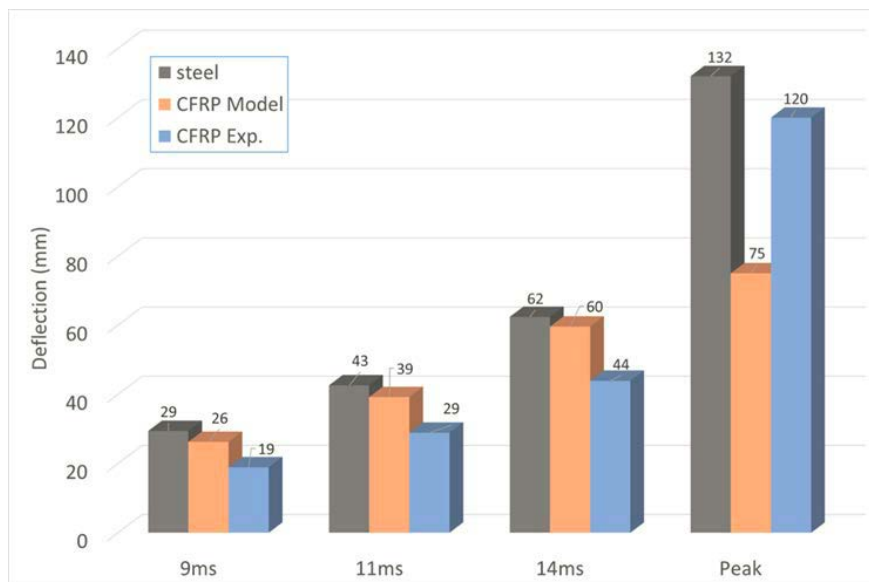


Figure 8-20. Spine Deflection at Key Times With Peak Deflection for Metal Baseline, CFRP Model and Experiment

## 9. Feedback from Vehicle Simulation

---

The final design of the composite B-pillar as produced and tested by UD-CCM is described in Section 6. As a proof of concept on the vehicle level the predictive design model was integrated into the Stage 2 vehicle simulation model.

Integration of the composite B-pillar into the vehicle simulation model required some modification of both the geometry of the BIW FE representation and the material models used for crash modeling of composites at BMW.

### 9.1 Geometrical Vehicle Integration

In the original metal design BIW, the B-pillar was a highly integrated component and thus part of the side frame assembly. The composite B-pillar designed by UD-CCM, on the other hand, is bonded to the connecting metal parts (rocker and roof rail) using adhesive. Therefore, the steel B-pillar was cut out and some adjustments were made in the flange regions to generate space for the bonded B-pillar assembly, as shown in Figure 9-1.

Due to the greater wall thickness in the composite design compared to the metal B-pillar, some minor intersections with the outer surface of the roof rail and the doors had to be resolved. These minimal changes are expected to have no major influence on the performance of these parts.

#### 9.1.1 LS-DYNA to ABAQUS Translation

At BMW, vehicle crash simulations were performed using the FE solver ABAQUS/Explicit. Since the design model used at UD-CCM was run in LS-DYNA, the model had to be translated back into the ABAQUS environment. Changes to the mesh as well as the composite information such as material orientation and stack information, could be performed using commercial software such as BETA CAE's ANSA preprocessor. This process was not completely automated since it was only done once and was only necessary due to the use of different FE solvers among the partners in this project. However, if necessary, this process could easily be automated.

Section 5 describes the unique properties of the material used in this project. In particular, the chosen materials offer a great amount of ductility that is not common in thermoset CFRP materials. The material model used for crash simulation of CFRP materials at BMW, provided by the FE solver ABAQUS/Explicit, was limited to modeling more brittle material characteristics. This has been proven suitable for the thermoset materials used in the BMW i-Models. For this project however, the material model was adapted to capture a greater amount of ductility provided by the thermoplastic matrices.

Figure 9-2 shows a comparison between the material model stress strain output under compression loading in fiber direction between the initial ABAQUS material model and the MAT54 model used in LS-DYNA. The grey curves show test results from material characterization, the **green** curve is the ABAQUS output and the **red** curve represents the LS-DYNA output.

The LS-DYNA model features an instant drop off in stress after initial failure, which represents fiber damage. As described in detail in Section 8, the stress does not drop to zero but is held at

a stress limit value that represents the residual strength of the composite after initial failure. The area under the curve can be interpreted as absorbed energy.

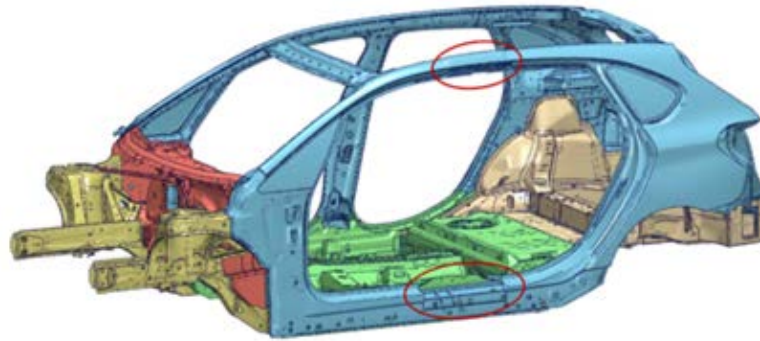


Figure 9-1. BIW Model With Cut Outs and Adjustments for Composite B-Pillar Integration

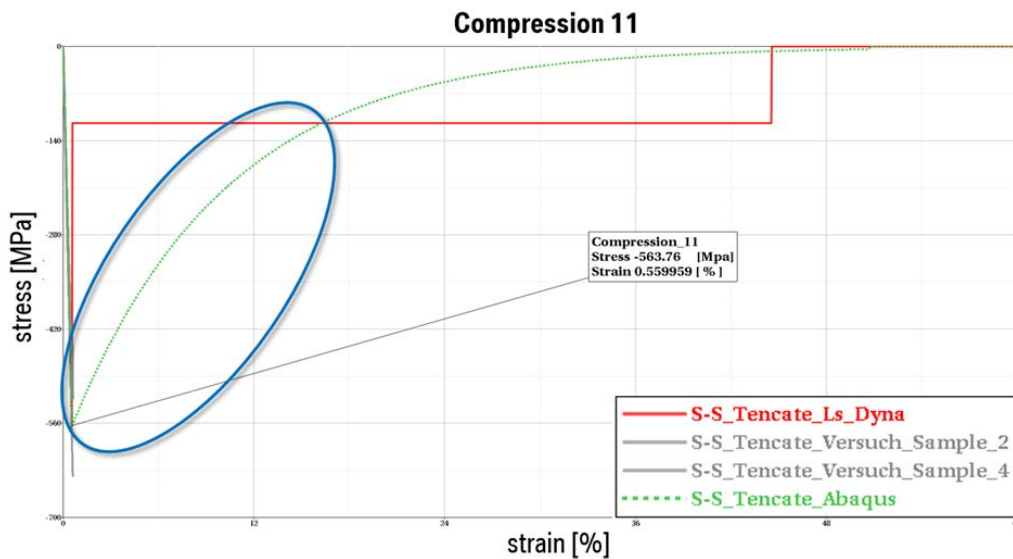


Figure 9-2. Stress-Strain Comparison Between LS-DYNA MAT54 and Initial ABAQUS Material Model

The ABAQUS model features an exponential decrease in stress after initial failure. This decrease is characterized by the area under the curve, which has to be given as a material parameter for this model. To achieve an initial drop off in stress similar to the LS-DYNA model this value had to be very small, which then led to a stress drop off to zero and a lack of energy absorption. For the green curve shown in Figure 9-2 the area under the LS-DYNA output curve was set as fracture energy, which led to high stresses after initial failure (circled region) and thus to high forces being transferred through the element.

Both behaviors, the instant drop off to zero and the rather smooth decrease with equal energy absorption, as shown in Figure 9-2 were not suitable to model the used thermoplastic materials.

To address this issue, a user material routine was implemented for ABAQUS/Explicit as shown in Figure 9-3. The new ABAQUS user material allowed for definition of a residual stress level and in addition the user can specify the slope of the curve after initial failure by defining the fracture energy that is consumed until the residual stress is reached. With this user routine,

it is possible to almost exactly calibrate the model to the LS-DYNA response on a single element level.

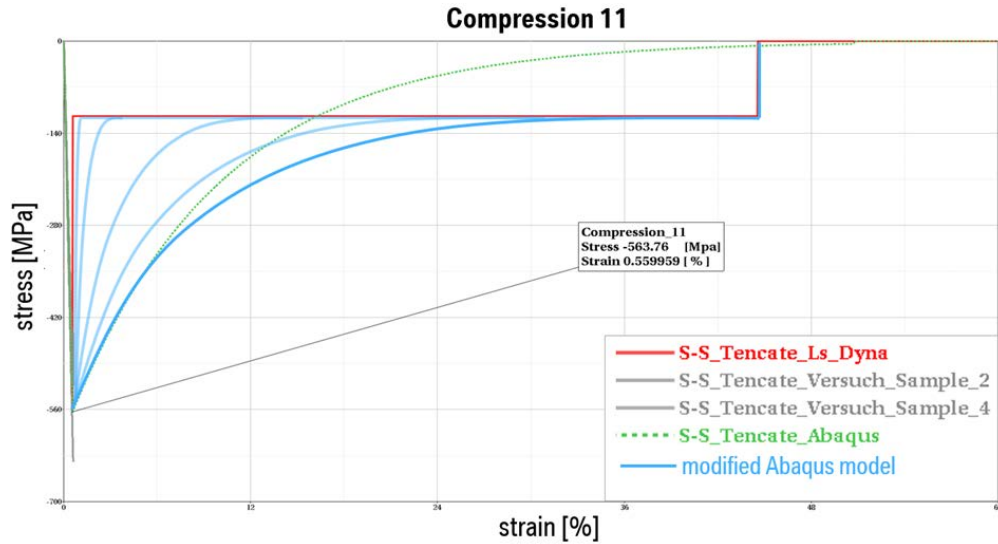


Figure 9-3. Stress-Strain Enhanced ABAQUS Material Model

One focus of this project was the demonstration of predictive computational methods, the other to demonstrate the feasibility of a CFRP B-pillar to meet the legal side-impact requirement. The structural requirements defined in Section 3.2.2 were to be fulfilled on component level in the Stage 4 reduced component environment and confirmed in the hardware tests. However, to obtain feedback from the vehicle environment, the design model was integrated into the Stage 2 vehicle model.

Figure 9-4 shows a comparison of the baseline steel B-pillar in blue and the composite B-pillar in red, both in the Stage 2 vehicle model at the time of maximum intrusion of the composite B-pillar.

The measured intrusions over time can be obtained from Figure 9-5. Each of the diagrams represents one of the defined measurement locations from Section 3.2.2. Both, metal and composite model, show a similar history of intrusion at all measured locations until 20 ms. At this point in time a major deviation between the two models was noticed. Especially the location of  $z = 397$ ,  $z = 693$  and  $z = 935$  show significantly higher intrusions in the composite model.

The relatively high intrusion in the composite model was caused by a local effect that is shown in Figure 9-4. The upper hinge of the rear door was pushed into the B-pillar's hat section and caused a local collapse. This led to a global kinking of the B-pillar rather than a progressive crushing and energy absorbing mode that can be observed in the component model and test results. However, undergoing a different deformation mode, the composite model does not predict a failure of the inner surface of the B-pillar or debonding in the flange regions.

Even though the load introduced by the doors can have a significant impact on the design of a B-pillar, this localized effect was not taken into account when the component model was developed for this project. In an actual vehicle development, this issue – amongst other load cases like roof crush, oblique pole, and other MDB load cases – would have to be addressed in subsequent design phases. However, these topics were discarded for this project in order to obtain a manageable effort for the resources in hand.



The final conclusions are outlined in Section 10.

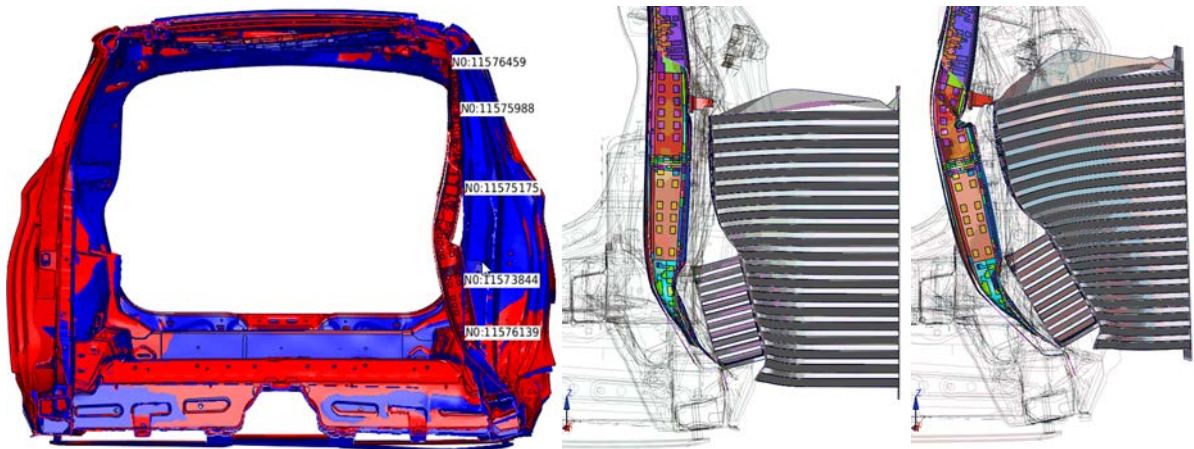


Figure 9-4. Comparison of Metal Baseline and Composite B-Pillar at Stage 2 Vehicle Model, Door Hinge Causing Local Collapse of Hat Section

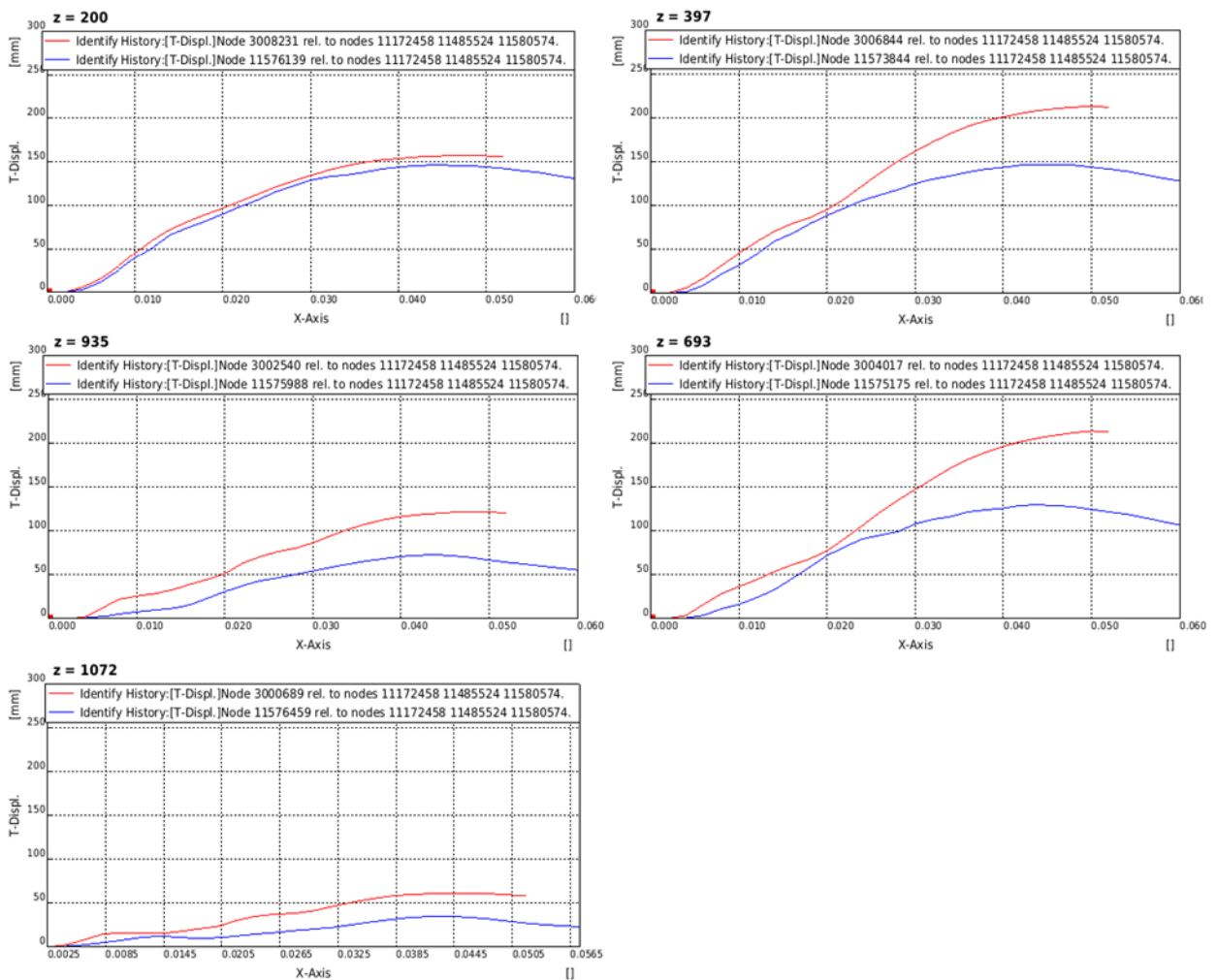


Figure 9-5. Comparison of Metal Baseline and Composite B-Pillar Intrusion Over Time



## 10. Conclusions

---

UD-CMM in partnership with NCMS, NHTSA, and BMW investigated thermoplastic carbon fiber reinforced materials for vehicle side frame structures. The proposed B-pillar was designed to meet structural and crash safety requirements (e.g., FMVSS No. 214 barrier) using thermoplastic composites that offers significant advantages (e.g., recycling, joining) compared to thermoset with the potential for improved crash performance. Novel side-impact crash concepts maximizing crash performance have been developed and commercially available thermoplastic materials were characterized to define appropriate material models and to evaluate energy absorption mechanisms. Predictive engineering at all levels, from coupon to sub-element to full-scale, guided the material down-selection. The same CAE tools simulate full vehicle to component and test setup behavior and were used to optimize manufacturability and structural/crash performance. Sub-components and B-pillars have been fabricated using the stamp forming and infusion processes allowing scalability with the potential to meet automotive production rates in the future. UD-CCM large drop tower was used to validate the predictive engineering tools and crash performance of the proposed B-pillars under realistic side-impact crash conditions.

The B-pillar design was spatially optimized for energy absorption (ductility), stiffness, and strength while maintaining part producibility and vehicle integration. BMW established B-pillar performance metrics derived from full-vehicle crash simulations and other design and integration requirements. UD-CCM provided full range of capabilities in materials selection and evaluation, composite design, analysis and crash simulations, process development and manufacturing (tooling, part production, trimming), full-scale pillar assembly and high-energy impact testing. This project has demonstrated design, materials, manufacturing and joining methods with continuous carbon fiber thermoplastics, at TRL 4-7 to meet automotive industry and government safety specifications. Key achievements from this project are summarized as follows.

- Successful fabrication and manufacture of an all thermoplastic composite B-pillar that is 60 percent lighter than the existing metallic design while meeting project requirements for NHTSA FMVSS No. 214 MDB side-impact crash.
- State-of-the-art CAE tools were evaluated (with internally developed data translation) simulating full vehicle to component impact (Dassault Systemes CATIA, Altair HyperWorks & LSTC LS-DYNA).
- Innovative production methods were developed and demonstrated for this multi-material part that included infusion and thermoforming tailored blanks with the potential to meet 2 minute cycle times.
- Adhesive bonding methods were developed and automated for dissimilar thermoplastics and steel interfaces.
- Automated trimming of the thermoplastic components was developed and demonstrated without damage to the composite structure.
- A test fixture was designed and integrated into UD-CCM high-energy impact tower simulating the crash behavior during side-impact crash without using a full vehicle structure.
- Multiple full-scale B-pillar assemblies (incorporating steel roof and frame rail) were successfully impact tested under 100 percent equivalent energy of FMVSS No. 214 MDB.

- The composite B-pillar response in the vehicle sub-component configuration satisfies all of the intrusion safety requirements considered for this project
- All composite B-pillars exhibited rebound and post-impact structural integrity in terms of fully supporting the impactor dead weight of 568.80 kg.
- The impact test was simulated and compared to the experimental data (deflection, load, and others) validating the predictive engineering approach.

The goals of the project, validating the predictive engineering tools and demonstrating equal or better occupant safety performance at reduced weight as equivalent steel vehicle components, have been successfully accomplished.

DOT HS 812 404  
April 2017



U.S. Department  
of Transportation  
**National Highway  
Traffic Safety  
Administration**



12885-042117-v2